PASSIVE MILLIMETER WAVE SIMULATION IN BLENDER

by

Maciej Murakowski

A thesis submitted to the Faculty of the University of Delaware in partial fulfillment of the requirements for the degree of Master of Science in Electrical and Computer Engineering

Fall 2014

PASSIVE MILLIMETER WAVE SIMULATION IN BLENDER

by

Maciej Murakowski

Approved: ____
Dennis W. Prather, Ph.D.
Professor in charge of thesis on behalf of the Advisory Committee

Approved: ____
Kenneth E. Barner, Ph.D.
Chair of the Department of Electrical and Computer Engineering

Approved: ____
Babatunde Ogunnaike, Ph.D.
Dean of the College of Engineering

Approved: ____
James G. Richards, Ph.D.
Vice Provost for Graduate and Professional Education

ACKNOWLEDGMENTS

I would first of all like to thank my family for their love and support, both during this writing of this thesis and throughout my life. I am also grateful to my friends for keeping me sane while taking crazy hours and cancelled plans in stride.

Professionally, I owe a debt of gratitude to John Wilson for his invaluable aid in testing and his limitless patience for the lie that is "It should work now;" to Lee Stein, Dan Mackrides, John Wilson (again), and Chris Schuetz for collecting the experimental data used in validating this work; to Garrett Schneider and Janusz Murakowski, for their experience, insight, and invaluable aid in helping me understand the math; to the members of the Prather research group, who have often been a source of ideas and inspiration; and to my advisor, Dennis Prather, for allowing me the opportunity to work on this project. Thank you all.

Finally, I wish to thank Ton Roosendaal, the Blender Foundation, the Blender developers, and the countless people in the Blender community, for producing such a wonderful piece of free software. Without them, this would not have been possible.

for Kep

TABLE OF CONTENTS

LIST OF TABLES

LIST OF FIGURES

ABSTRACT

Imaging in the millimeter wave (mmW) frequency range is being explored for applications where visible or infrared (IR) imaging fails, such as through atmospheric obscurants. However, mmW imaging is still in its infancy and imager systems are still bulky, expensive, and fragile, so experiments on imaging in real-world scenarios are difficult or impossible to perform. Therefore, a simulation system capable of predicting mmW phenomenology would be valuable in determining the requirements (e.g. resolution or noise floor) of an imaging system for a particular scenario and aid in the design of such an imager.

Producing simulation software for this purpose is the objective of the work described in this thesis. The 3D software package Blender was modified to simulate the images produced by a passive mmW imager, based on a Geometrical Optics approach. Simulated imagery was validated against experimental data and the software was applied to novel imaging scenarios. Additionally, a database of material properties for use in the simulation was collected.

Chapter 1

INTRODUCTION

In this chapter we introduce millimeter waves (mmWs), discuss some of the motivation behind imaging in the mmW regime, and introduce the passive mmW (pmmW) simulation software that is the subject of this thesis.

1.1 Millimeter Waves

Millimeter waves comprise the portion of the electromagnetic spectrum between approximately 30 to 300 GHz, with wavelengths between 10 and 1 mm. Millimeter waves are emitted by every object with a non-zero temperature; the power a perfectly emissive black body with surface area dA radiates into a solid angle $d\Omega$, across a bandwidth $d\nu$, is given by Planck's Law,

$$P = \frac{2h\nu^3}{c^2}\frac{1}{e^{h\nu/kT}-1}dA\,d\nu\,d\Omega \approx \frac{2k\nu^2}{c^2}T\,dA\,d\nu\,d\Omega \tag{1.1}$$

where $h = 6.626 \times 10^{-34}\,\mathrm{J\,s}$ is Planck's constant, $c = 2.998 \times 10^{8}\,\mathrm{m\,s^{-1}}$ is the speed of light, $k = 1.318 \times 10^{-23}\,\mathrm{J\,K^{-1}}$ is Boltzmann's constant, and T is the absolute temperature of the emitter in Kelvin. The approximation is due to taking the first two terms of a Taylor series expansion for $e^{h\nu/kT}$, and is accurate for objects at terrestrial temperatures even to several hundred gigahertz. From this, a black body at room temperature radiates approximately 800 nW of power, per square meter of surface area, per steradian, per gigahertz bandwidth at 95 GHz; by way of comparison, the peak emission is $5\,\mathrm{mW\,m^{-2}\,sr^{-1}\,GHz^{-1}}$ at a wavelength of 17 μm, nearly four orders of magnitude higher than the pmmW emission.

Both the low power and the low energy of the individual photons (400 μeV at 95 GHz) makes passive imaging in the mmW regime difficult; however, both detection

Figure 1.1: Atmospheric absorption under several atmospheric conditions. STD is a standard atmosphere with $7.5\,\mathrm{g\,m^{-3}}$ water vapor; humid is a standard atmosphere with $15\,\mathrm{g\,m^{-3}}$ water vapor; rain corresponds with a rain rate of $4\,\mathrm{mm\,h^{-1}}$; fog corresponds with a dense fog with 100 m visibility in the visible wavelengths [4].

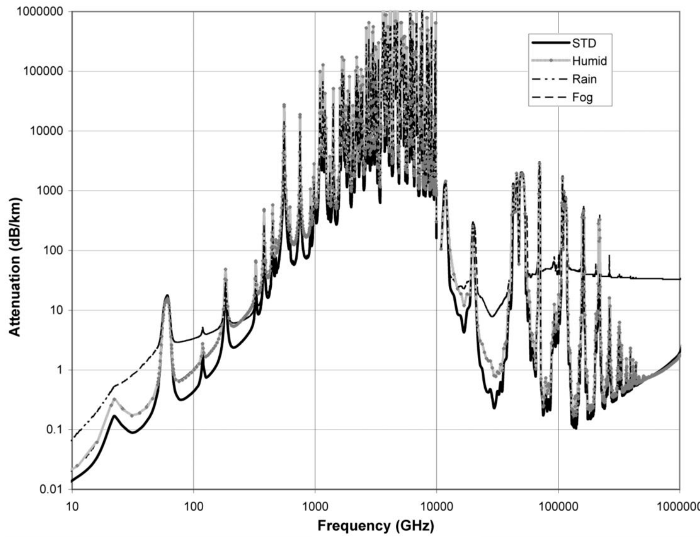

and imaging has been demonstrated using microbolometers [1] or a heterodyne process, through either up or downconversion [2, 3].

1.2 Motivation

Regardless of the challenges associated with the detection of mmW radiation, millimeter waves have several properties that make them attractive for imaging. Millimeter waves have relatively good propagation characteristics in atmosphere, as shown in Figure 1.1 [4]; though there are several peaks due to water and oxygen absorption, there are multiple frequency ranges where the waves propagate with essentially no attenuation, particularly around 35, 77, 95, 140, and 220 GHz; this allows both passive and active systems to be used at distances of several kilometers with attenuation comparable to visible-wavelength systems. More importantly, however, mmWs retain good propagation characteristics even in foggy or rainy weather, where the visibility in other wavelength regimes degrades significantly.

Additionally, in passive outdoor imaging scenarios, the sky is a constant source of illumination: the 3 K cosmic microwave background signal is largely unattenuated by the intervening atmosphere, leaving the sky a low-temperature target, regardless of weather or time of day. Terrestrial objects, meanwhile, are relatively warm, leading to high contrast within the scene.

Finally, mmW wavelengths are small enough to achieve reasonable resolution without requiring an excessively large imager; while a man-portable imager might not be feasible, a system with adequate performance could easily be mounted on a vehicle platform.

Three applications of pmmW imaging come immediately to mind. First, objects small enough to remain suspended in the atmosphere are also small enough that mmW scattering is in the Rayleigh regime, where the factor of $(d/\lambda)^4$ means that scattering is effectively negligible, allowing imaging through fog, dust, or other atmospheric obscurants. This phenomenology is demonstrated for fog and rain (as in Figure 1.1) and similar results for suspended dust have been reported [5]. This has potential applications, for example, in allowing aircraft to land safely in adverse weather conditions in the absence of active ground-based systems, enabling search-and-rescue operations in low visibility, or imaging in maritime fog. Second, due to their thickness and material properties, most clothing items are effectively transparent to mmW radiation. This has already been applied, with many airports deploying active mmW imaging systems to scan travelers for concealed contraband, and similar systems employing passive imagers are also being considered. Because most plastics are also transparent, such systems can be used to scan optically opaque containers as well. Third, as compared to IR imaging or radar, mmW imaging is a relatively new technology. While there are mature techniques for camouflage in the visible, IR, or radar spectra, countermeasure techniques in millimeter waves are still underdeveloped, and mmWs could be used to counteract countermeasures optimized for other parts of the EM spectrum.

However, before resources are devoted to deploying mmW systems for these applications, it would be advantageous to determine whether a mmW imager could perform the required task at all, which motivates the creation of simulation software.

1.3 mmW Blender

Our simulation software is based on a modified version of the 3D modeling and rendering software Blender [6]. Our motivation for using Blender as a base was threefold. Though we could have written our own rendering engine from scratch, it would not have been well-integrated with any scene creation tools; using Blender allows us to provide a unified system where one can design, model, and simulate an mmW image, all as part of the same workflow. This ties in with usability: there is a lower bound on the ease-of-use of any sufficiently powerful software package, but the wide availability of tutorials and community support for Blender eases the learning curve considerably. Finally, there was programming time: modifying existing software enabled us to quickly produce a functional mmW simulator, and the first version of mmW Blender was put into use in 2010 after only a few months of development.

In the remainder of this section, we give an overview of Blender and define some of the terminology we use later in this thesis.

Blender is an open-source 3D modeling, animation, and rendering software package, written primarily in C, C++, and Python. It was originally developed as a commercial product, but when the company producing it shut down in 2002, the community surrounding it bought the source code and released it under the GNU GPL. The nonprofit Blender Foundation and a team of volunteers from around the world have been developing it since. Blender now supports rigid body simulation, fluid simulation, smoke, fire, and hair rendering, GPU-accelerated rendering, and many modeling and animation features that make it useful not only for rendering mmW scenes, but also creating them in the first place.

Blender considers geometry as being constructed from triangular or quadrilateral polygons, called faces; the faces have associated with them vertices and edges. Alternate bases for geometries, such as those constructed from primitive shapes (e.g. spheres, cylinders, or prisms) or NURBS surfaces—which Blender supports, though it converts them to triangles for rendering—are possible, and used by other software. A collection of these faces makes up a mesh (e.g. a cube, person, Möbius strip, or collection of disconnected triangles), and each mesh is associated with an object; a collection of objects is a scene, and this scene is what is finally simulated. It is important to note that Blender has no intrinsic concept of solid or volumetric objects; volumetric rendering techniques (e.g. loss while propagating through a material) can only be simulated by assuming the underlying mesh geometry is well-behaved.

Each face is assigned a material; the material has associated with it a number of properties; some (such as index of refraction) are taken from the real world and others (such as RGB color) have no real-world analogue but are used in various approximations of real-world behavior. The scene simulation, called rendering, is performed based on the location, orientation, dimensions, and material properties of each face in the scene, and the position of a virtual detector called a camera; the details of how this is performed for mmW simulation is discussed in the following chapters.

Chapter 2

PASSIVE MILLIMETER WAVE SIMULATION

In this chapter we present the techniques used in our simulation of passive mmW scenarios. We describe and justify the approximations we make, and validate the simulation with experimentally collected data.

2.1 Geometrical Optics

In this section, we discuss our approach to geometrical optics, our chosen approximation for pmmW simulation. Beginning from Maxwell's Equations, we introduce the concept, develop the equations for propagation of mmW energy within a scene, and formulate an expression for the power detected by an imager in a scene.

2.1.1 Introduction

The geometrical optics approach considers an infinitely thin "pencil ray" originating from somewhere, either within or outside the scene. The ray enters the scene, interacts with scene geometry (potentially being split by reflection, refraction, or scattering into multiple rays), and eventually either makes its way to the detector where it is transformed into an image pixel, or is lost by escaping the scene or being completely absorbed. The ray experiences no diffraction effects, and is affected only by geometry it directly intersects.

Unfortunately, though this is the correct formulation of geometrical optics, in that the properties of all emitted rays are known fully and no approximations save for geometrical optics applying are made, it is highly inefficient computationally. Because the detector small in comparison to the scene, the probability of any particular ray interacting with it is small, so the overwhelming majority of rays do not contribute anything to the final image. This wastes computation time and increases the simulation run time beyond what is acceptable. The usual approach, which the Blender ray tracing engine implements, is to take advantage of reciprocity and run the process in reverse: rays originate at the camera and are launched to the scene; they interact with scene geometry, being split into multiple child rays, until a set number of interactions is reached or the ray escapes the scene. Those rays are then back-propagated to the detector.

The geometrical optics approximation is justified when surfaces are smooth, flat, and large in comparison to the wavelength of the radiation under consideration. Where geometrical optics fails, an extension called the geometrical theory of diffraction, which accounts for diffraction effects by considering additional rays originating at edges and corners [7], or various more complicated methods are used. However, at 95 GHz, the free-space wavelength is approximately 3 mm; many objects of interest, including most architecture, vehicles, and human bodies, are smooth on the scale of 1 mm; they are each also considerably larger than 3 mm. Therefore, we expect geometrical optics to be a good approximation of the behavior of passive millimeter waves, for many objects we would be interested in imaging. This is justified by several experiments found in the literature, two of which are described below.

We first consider a study on the monostatic reflection of a road surface at 35 GHz [8]; the authors attempt to fit monostatic (wherein the detector is at the same location as the illumination source) reflection at mmW frequencies to a Phong-like model. The Phong model is based on a lighting model from 3D graphics, and is characterized by a weak diffuse lighting term that radiates approximately isotropically, and a sharp specular reflection centered around some reflection direction [9]; on a curved surface this manifests as a bright specular highlight. The authors find that the monostatic reflection exhibits a sharp specular highlight when the surface is being viewed head-on, and a much weaker return off-normal. The results of this fit are shown in Figure 2.1, which shows the monostatic scattering return for a road surface, as a function of angle from normal.

Figure 2.1: Monostatic reflectance from a road surface fit with two reflectivity models [8].

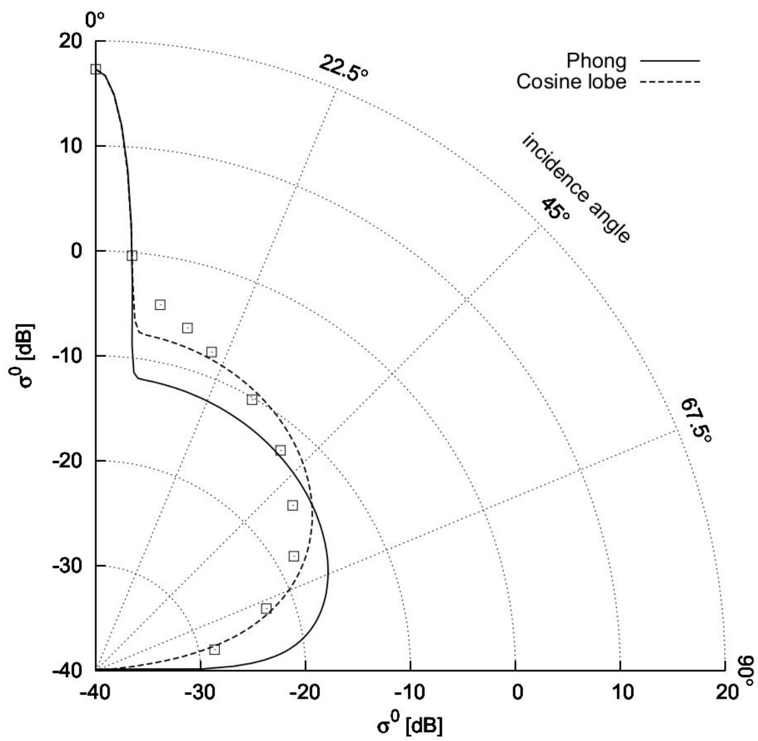

The quality of the fit is not important to us; rather, the important thing to note is that at only 5° away from the normal, the returned signal has dropped 18 dB from the signal at normal. This indicates that the specular cone is less than 10° wide at normal incidence, i.e. that most of the energy is reflected in the specular direction. There is no significant backscatter at any other angle.

Stronger demonstration of the mostly specular nature of the reflections is obtained from bistatic measurements [10]. A soil surface with r.m.s surface height 3.28 mm, corresponding to 0.52λ at the experimental frequency of 34.5 GHz, was illuminated from an angle of 20° from zenith, and the response was measured as a function of azimuthal and zenithal angle. The response in the vertical polarization from a vertically-polarized incident field is plotted in Figure 2.2.

The incident direction is denoted by $\mathrm{T_x}$. For this surface, the maximum response in an off-specular direction is −6 dB, corresponding to 25% of the specular reflection; notably, the strongest non-specular reflection is in the backscatter direction, which is expected due to micro-corner reflectors in the dirt; the reflection in all other directions is significantly weaker. By reciprocity, this means that most of the energy being reflected in the $\mathrm{T_x}$ direction originates either from specular reflection, or from $\mathrm{T_x}$. Thus, geometrical optics is a good first approximation to the reflection from even a rough surface.

2.1.2 Plane Waves

We now describe the pencil rays of Section 2.1.1 in terms of a plane wave solution to Maxwell's equations. In the absence of free charges, Maxwell's Equations are

$$\nabla \cdot \mathbf{D} = 0 \tag{2.1a}$$

$$\nabla \cdot \mathbf{B} = 0 \tag{2.1b}$$

$$\nabla \times \mathbf{E} = -\frac{\partial \mathbf{B}}{\partial t} \tag{2.1c}$$

$$\nabla \times \mathbf{H} = \frac{\partial \mathbf{D}}{\partial t} \tag{2.1d}$$

Figure 2.2: Bistatic reflection from a rough (0.52λ r.m.s. height) soil surface at 34.5 GHz [10].

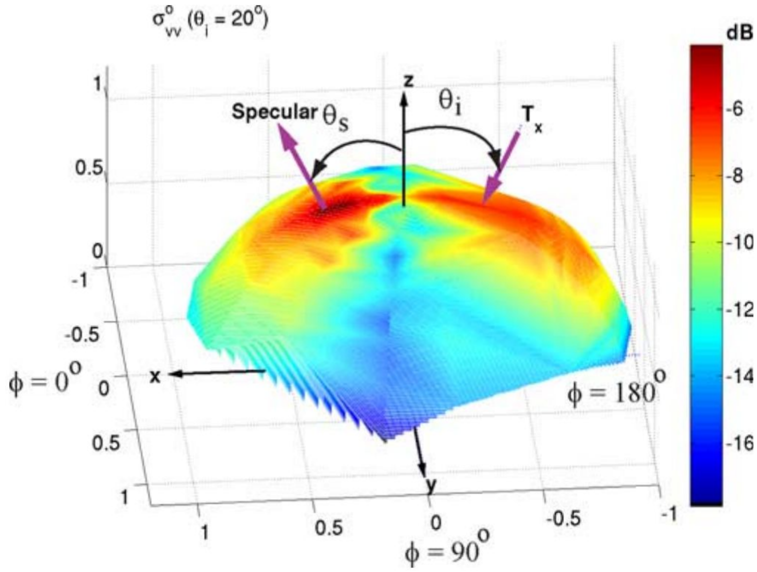

In an isotropic, linear medium with complex permeability μ and complex permittivity ε (i.e. $\mathbf{B} = \mu\mathbf{H}$ and $\mathbf{D} = \varepsilon\mathbf{E}$ for scalar μ and ε that are not functions of $\mathbf{H}$ or $\mathbf{E}$), Maxwell's equations admit a plane wave solution of the form

$$\mathbf{E}(\mathbf{r}, t) = \mathbf{E}_0 e^{i(\mathbf{k}\cdot\mathbf{r}-\omega t)} \tag{2.2}$$

where ω is the temporal angular frequency, $\mathbf{r}$ and t are the position vector and time, respectively, $\mathbf{E}_0$ is a complex vector, and $\mathbf{k}$ is the complex vector wavenumber, which obeys the dispersion relation

$$\mathbf{k}\cdot\mathbf{k} = k^2 = \omega^2\mu\varepsilon \tag{2.3}$$

Substituting this solution into Maxwell's equations, we can replace the differential operators $\nabla \Rightarrow i\mathbf{k}$ and $\frac{\partial}{\partial t} \Rightarrow -i\omega$; canceling the phase factors $e^{i(\mathbf{k}\cdot\mathbf{r}-\omega t+\phi)}$, Maxwell's

Equations become

$$\mathbf{k} \cdot \mathbf{E}_0 = 0 \tag{2.4a}$$

$$\mathbf{k} \cdot \mathbf{H}_0 = 0 \tag{2.4b}$$

$$\mathbf{k} \times \mathbf{E}_0 = \omega\mu\mathbf{H}_0 \tag{2.4c}$$

$$\mathbf{k} \times \mathbf{H}_0 = -\omega\varepsilon\mathbf{E}_0 \tag{2.4d}$$

It is important to note that all above vector quantities ($\mathbf{k}$, $\mathbf{E}_0$, and $\mathbf{H}_0$) can be complex. The scalar quantities ε and μ can also be complex, but ω is taken to be real (i.e. the wave exists for all time). For the permittivity we write $\varepsilon = \varepsilon_0\varepsilon_r$, where ε_0 is the permittivity of free space, an exact quantity defined as $\varepsilon_0 = 1/c^2\mu_0 \approx 8.854 \times 10^{-12}\,\mathrm{F\,m^{-1}}$, and ε_r is the dielectric constant, which can be complex; in that case, we write $\varepsilon_r = \varepsilon_r' + i\varepsilon_r''$. ε_r is a function of frequency for most materials across the entire frequency range; in contrast, for most materials at high frequencies, the permeability approaches the vacuum permeability, i.e. $\mu = \mu_0 = 4\pi \times 10^{-7}\,\mathrm{H\,m^{-1}}$; we assume that our frequencies of interest are high enough that this is the case for the remainder of this thesis.

We write the vector $\mathbf{k}$ in terms of the scalar wavenumber k as $\mathbf{k} = k\hat{\mathbf{k}}$, with $\hat{\mathbf{k}} \cdot \hat{\mathbf{k}} = 1$; according to Equation 2.3, $k = \omega\sqrt{\mu\varepsilon} = \omega n\sqrt{\mu_0\varepsilon_0} = \omega n/c$ where $n = \sqrt{\varepsilon_r}$ is the refractive index of the medium. Finally, we note that the unit vector $\hat{\mathbf{k}}$ can be real or complex. If it is real, we say the wave is homogeneous, otherwise it is heterogeneous; some implications of a complex $\hat{\mathbf{k}}$ will be explored in a later section.

2.1.3 Jones Formalism

We have described the propagation within a material with Equation 2.2; now we wish to determine the ray that results after interacting with a surface.

We consider a plane wave, denoted by $\mathbf{E}_0(\mathbf{r}, t)$, at frequency ω in a material with refractive index n_0 propagating in the direction of $\hat{\mathbf{k}}_0$. Note that we need only the electric field, as the magnetic field $\mathbf{H}_0(\mathbf{r}, t)$ can be trivially obtained from Equation

2.4c. We cast Equation 2.2 in terms that are more amenable to computation by defining two unit vectors $\hat{\mathbf{s}}_0$ and $\hat{\mathbf{p}}_0$ such that $\hat{\mathbf{s}}_0$, $\hat{\mathbf{p}}_0$, and $\hat{\mathbf{k}}_0$ form an orthonormal triple. Then

$$\mathbf{E}_0(\mathbf{r},t) = \left[A\hat{\mathbf{s}}_0 + Be^{i\phi}\hat{\mathbf{p}}_0\right] e^{i\left(\frac{\omega}{c}n_0\hat{\mathbf{k}}_0\cdot\mathbf{r}-\omega t\right)} \tag{2.5}$$

where the $e^{i\left(\frac{\omega}{c}n_0\hat{\mathbf{k}}_0\cdot\mathbf{r}-\omega t\right)}$ term as usual denotes the time-harmonic phase propagation in the $\hat{\mathbf{k}}_0$ direction; the term in square brackets describes the polarization state, with real scalars A, B, and ϕ; this representation is unique up to an arbitrary phase. In the case of a coherent field, ϕ has a set value that determines the polarization of the wave: for real $\hat{\mathbf{s}}_0$ and $\hat{\mathbf{p}}_0$, $\phi = 0$ or $\phi = \pi$ gives linear polarization, $\phi = \pi/2$ gives circular, and so on. If the radiation is incoherent, however, ϕ is ill-defined and can take on any value between 0 and 2π; additionally, any time-averaged quantity we extract from the incoherent field must *also* be averaged over all possible values of ϕ.

We now compute the results of the interaction of the plane wave of Equation 2.5 with matter. To do this, we consider two basic interactions: the propagation through a material, and the interaction with an interface between two materials. We write the plane wave after $j-1$ interactions; that is, the field has been reflected or transmitted through a material interface, and propagated between interactions $j-1$ times. The plane wave now has the form

$$\mathbf{E}_{j-1}(\mathbf{r}) = \left[f_{j-1}(\phi)\,\hat{\mathbf{s}}_{j-1} + g_{j-1}(\phi)\,\hat{\mathbf{p}}_{j-1}\right] e^{i\left(\frac{\omega}{c}n_{j-1}\hat{\mathbf{k}}_{j-1}\cdot\mathbf{r}-\omega t\right)} \tag{2.6}$$

where f_{j-1} and g_{j-1} are unknown functions of ϕ and $\hat{\mathbf{s}}_{j-1}$ and $\hat{\mathbf{p}}_{j-1}$ are complex polarization basis vectors orthogonal to $\hat{\mathbf{k}}_{j-1}$. We now consider this field incident on the j^{th} interface. We call the local incident-field coordinates $\hat{\mathbf{s}}_j^i$ and $\hat{\mathbf{p}}_j^i$, and we write the incident field in terms of the local coordinates (dropping the propagation terms and explicit ϕ dependence for the sake of clarity)

$$\mathbf{E}_{j-1}^i = \left(f_{j-1}\hat{\mathbf{s}}_{j-1}\cdot\hat{\mathbf{s}}_j^i + g_{j-1}\hat{\mathbf{p}}_{j-1}\cdot\hat{\mathbf{s}}_j^i\right)\hat{\mathbf{s}}_j^i + \left(f_{j-1}\hat{\mathbf{s}}_{j-1}\cdot\hat{\mathbf{p}}_j^i + g_{j-1}\hat{\mathbf{p}}_{j-1}\cdot\hat{\mathbf{p}}_j^i\right)\hat{\mathbf{p}}_j^i \tag{2.7}$$

We compute the vector $\hat{\mathbf{k}}_j$, i.e. the propagation direction after interacting with the surface, using some relation to be determined later, then compute the outgoing local coordinates $\hat{\mathbf{s}}_j$ and $\hat{\mathbf{p}}_j$, and write the field as a result of the interaction as

$$\begin{aligned}\mathbf{E}_j = &\left[\chi_{ss,j}\left(f_{j-1}\hat{\mathbf{s}}_{j-1}\cdot\hat{\mathbf{s}}_j^i + g_{j-1}\hat{\mathbf{p}}_{j-1}\cdot\hat{\mathbf{s}}_j^i\right) + \chi_{sp,j}\left(f_{j-1}\hat{\mathbf{s}}_{j-1}\cdot\hat{\mathbf{p}}_j^i + g_{j-1}\hat{\mathbf{p}}_{j-1}\cdot\hat{\mathbf{p}}_j^i\right)\right]\hat{\mathbf{s}}_j \\ &+ \left[\chi_{pp,j}\left(f_{j-1}\hat{\mathbf{s}}_{j-1}\cdot\hat{\mathbf{p}}_j^i + g_{j-1}\hat{\mathbf{p}}_{j-1}\cdot\hat{\mathbf{p}}_j^i\right) + \chi_{ps,j}\left(f_{j-1}\hat{\mathbf{s}}_{j-1}\cdot\hat{\mathbf{s}}_j^i + g_{j-1}\hat{\mathbf{p}}_{j-1}\cdot\hat{\mathbf{s}}_j^i\right)\right]\hat{\mathbf{p}}_j\end{aligned} \tag{2.8}$$

The χ terms depend on the nature of the interaction with the surface and can be based on either theory or experiment (e.g. bistatic reflection measurements [10]); the explicit form we use is given in Sections 2.2.4 and 2.2.5. Finally, this new field will propagate along some vector $\mathbf{d}_j$ before it interacts with another surface. Therefore, it will acquire a phase factor of $e^{i\frac{\omega}{c}n_j\hat{\mathbf{k}}_j\cdot\mathbf{d}_j}$. We can write the final expression for the field $\mathbf{E}_j$ compactly in matrix notation,

$$\mathbf{E}_j = f_j\hat{\mathbf{s}}_j + g_j\hat{\mathbf{p}}_j \tag{2.9a}$$

$$\begin{pmatrix} f_j \\ g_j \end{pmatrix} = \begin{pmatrix} e^{i\frac{\omega}{c}n_j\hat{\mathbf{k}}_j\cdot\mathbf{d}_j} & 0 \\ 0 & e^{i\frac{\omega}{c}n_j\hat{\mathbf{k}}_j\cdot\mathbf{d}_j} \end{pmatrix} \begin{pmatrix} \chi_{ss,j} & \chi_{sp,j} \\ \chi_{ps,j} & \chi_{pp,j} \end{pmatrix} \begin{pmatrix} \hat{\mathbf{s}}_{j-1}\cdot\hat{\mathbf{s}}_j^i & \hat{\mathbf{p}}_{j-1}\cdot\hat{\mathbf{s}}_j^i \\ \hat{\mathbf{s}}_{j-1}\cdot\hat{\mathbf{p}}_j^i & \hat{\mathbf{p}}_{j-1}\cdot\hat{\mathbf{p}}_j^i \end{pmatrix} \begin{pmatrix} f_{j-1} \\ g_{j-1} \end{pmatrix} \tag{2.9b}$$

This allows us immediately to find the form of the original field of Equation 2.5 after N bounces, namely,

$$\mathbf{E}_N = f_N\hat{\mathbf{s}}_N + g_N\hat{\mathbf{p}}_N \tag{2.10a}$$

$$\begin{pmatrix} f_N \\ g_N \end{pmatrix} = \mathbf{T}\begin{pmatrix} A \\ Be^{i\phi} \end{pmatrix} \tag{2.10b}$$

$$\begin{aligned}\mathbf{T} &= \prod_{j=N}^{1} \begin{pmatrix} e^{i\frac{\omega}{c}n_j\hat{\mathbf{k}}_j\cdot\mathbf{d}_j} & 0 \\ 0 & e^{i\frac{\omega}{c}n_j\hat{\mathbf{k}}_j\cdot\mathbf{d}_j} \end{pmatrix} \begin{pmatrix} \chi_{ss,j} & \chi_{sp,j} \\ \chi_{ps,j} & \chi_{pp,j} \end{pmatrix} \begin{pmatrix} \hat{\mathbf{s}}_{j-1}\cdot\hat{\mathbf{s}}_j^i & \hat{\mathbf{p}}_{j-1}\cdot\hat{\mathbf{s}}_j^i \\ \hat{\mathbf{s}}_{j-1}\cdot\hat{\mathbf{p}}_j^i & \hat{\mathbf{p}}_{j-1}\cdot\hat{\mathbf{p}}_j^i \end{pmatrix} \\ &= \prod_{j=N}^{1} \mathbf{P}_j\boldsymbol{\chi}_j\mathbf{R}_j\end{aligned} \tag{2.10c}$$

where $\mathbf{P}_j$ is the propagation matrix in the j^{th} material, $\boldsymbol{\chi}_j$ is the scattering matrix of the j^{th} interface, and $\mathbf{R}_j$ is the rotation matrix into the local coordinates defined for the j^{th} interface.

We now take the field $\mathbf{E}_N$ incident upon a detector. The detector has local coordinates $\hat{\mathbf{x}}$ and $\hat{\mathbf{y}}$, so we must write the field in these coordinates. We do this in the usual way:

$$\mathbf{E}_{detector} = E_x\hat{\mathbf{x}} + E_y\hat{\mathbf{x}} \tag{2.11a}$$

$$\begin{aligned}\begin{pmatrix} E_x \\ E_y \end{pmatrix} &= \begin{pmatrix} \hat{\mathbf{s}}_N \cdot \hat{\mathbf{x}} & \hat{\mathbf{p}}_N \cdot \hat{\mathbf{x}} \\ \hat{\mathbf{s}}_N \cdot \hat{\mathbf{y}} & \hat{\mathbf{p}}_N \cdot \hat{\mathbf{y}} \end{pmatrix} \mathbf{T} \begin{pmatrix} \mathrm{A} \\ \mathrm{B}e^{i\phi} \end{pmatrix} \\ &= \begin{pmatrix} M_{00} & M_{01} \\ M_{10} & M_{11} \end{pmatrix} \begin{pmatrix} A \\ Be^{i\phi} \end{pmatrix}\end{aligned} \tag{2.11b}$$

Equation 2.11 allows us to begin with an arbitrary wave originating anywhere in the scene, and, knowing the path it takes to reach the detector and the parameters of the materials it interacted with, to compute its form at the detector. Thus, Equation 2.11 is the general solution for wave propagation in the geometrical optics approximation.

There are several non-obvious assumptions, limitations, and errors in this formulation. First, we implicitly assumed that the imager coordinate basis vectors $\hat{\mathbf{x}}$ and $\hat{\mathbf{y}}$ are real; in that case, we cannot necessarily project the field into them as in Equation 2.11b, so any derived quantities will also be incorrect. Second, we assume that a ray is self-coherent along its entire propagation distance within the scene; if the initial field is itself coherent, this causes no problems; however, if the initial field is incoherent, it is possible that the phase difference between the s and p polarizations will become large enough that the two can no longer be considered as interacting coherently when projected to a new surface coordinate system, i.e. that we can no longer use the $\mathbf{R}_j$ matrix to transform into local coordinates; there is no obvious solution to this problem but, absent birefringent materials, it should be rare. Relatedly, there is no way to extend this formulation to birefringent or anisotropic materials, as this exacerbates the problem as well as adding issues of spatial coherence. And finally, we have as yet presented no way of determining the path the ray takes to the detector; this important detail is deferred until Sections 2.2.4 and 2.2.5.

2.1.4 Stokes Parameters

A mmW detector does not measure instantaneous field strength directly; rather, it measures a time-averaged power, which we compute here. The four Stokes parameters I, Q, U, and V are a convenient measure not only of time-averaged power but also polarization information for an incoherent field. They are defined as

$$I = |E_x|^2 + |E_y|^2 \tag{2.12a}$$

$$Q = |E_x|^2 - |E_y|^2 \tag{2.12b}$$

$$U = 2\mathfrak{Re}\left\{E_x E_y^*\right\} \tag{2.12c}$$

$$V = 2\mathfrak{Im}\left\{E_x E_y^*\right\} \tag{2.12d}$$

The parameter I is the total intensity of the incident field; Q is the degree of horizontal-vertical linear polarization: $Q > 0$ if the polarization state is more horizontal than vertical, and $Q < 0$ if it is more vertical than horizontal; U is the degree of linear polarization in a basis rotated at a 45° angle from the horizontal, analogously to Q; and V is the degree of circular polarization: $V > 0$ if the field is left-circular, $V < 0$ if the field is right-circular from the point of view of the detector.

From Equation 2.11b, the field incident upon the detector, with the $e^{i\left(\frac{\omega}{c}n_n\hat{\mathbf{k}}_n\cdot\mathbf{r}-\omega t\right)}$ propagator implied, is

$$E_x = M_{00}A + M_{01}Be^{i\phi} \tag{2.13a}$$

$$E_y = M_{10}A + M_{11}Be^{i\phi} \tag{2.13b}$$

Recall that all time-averaged quantities for incoherent radiation must also be averaged over all values of ϕ. Therefore, we evaluate the auxiliary quantities and average over all ϕ

$$|E_x|^2 = \int_0^{2\pi} \left[M_{00}A + M_{01}Be^{i\phi}\right]\left[M_{00}^*A + M_{01}^*Be^{-i\phi}\right] d\phi$$
$$= |M_{00}|^2 A^2 + |M_{01}|^2 B^2 \tag{2.14a}$$
$$|E_y|^2 = \int_0^{2\pi} \left[M_{10}A + M_{11}Be^{i\phi}\right]\left[M_{10}^*A + M_{11}^*Be^{-i\phi}\right] d\phi$$
$$= |M_{10}|^2 A^2 + |M_{11}|^2 B^2 \tag{2.14b}$$
$$E_xE_y^* = \int_0^{2\pi} \left[M_{00}A + M_{01}Be^{i\phi}\right]\left[M_{10}^*A + M_{11}^*Be^{-i\phi}\right] d\phi$$
$$= M_{00}M_{10}^*A^2 + M_{01}M_{11}^*B^2 \tag{2.14c}$$

This gives the Stokes parameters,

$$I = \left(|M_{00}|^2 + |M_{10}|^2\right) A^2 + \left(|M_{01}|^2 + |M_{11}|^2\right) B^2 \tag{2.15a}$$
$$Q = \left(|M_{00}|^2 - |M_{10}|^2\right) A^2 + \left(|M_{01}|^2 - |M_{11}|^2\right) B^2 \tag{2.15b}$$
$$U = 2\mathfrak{Re}\left\{M_{00}M_{10}^*\right\} A^2 + 2\mathfrak{Re}\left\{M_{01}M_{11}^*\right\} B^2 \tag{2.15c}$$
$$V = 2\mathfrak{Im}\left\{M_{00}M_{10}^*\right\} A^2 + 2\mathfrak{Im}\left\{M_{01}M_{11}^*\right\} B^2 \tag{2.15d}$$

Note that all terms in Equation 2.15 have an A^2 or B^2 dependence only, i.e. that each term is dependent only on the powers (or, equivalently through Equation 1.1, radiometric temperature) of each initial polarization state; therefore, we can work entirely in terms of power (temperature). Also note that the terms $|E_x|^2$ and $|E_y|^2$, i.e. the power along the x and y axis of the imager, can be trivially obtained either from Equations 2.14 or 2.15 if they are needed.

2.1.5 Stokes Parameters from Many Rays

We have presented the Stokes parameters in the geometrical optics approximation due to some field that interacts with some set of surfaces on its way to the detector. Now we further extend this formulation in order to develop full passive mmW scene simulation.

We have already assumed that all rays are self-coherent (i.e. that we can obtain the Stokes parameters through Equations 2.11 and 2.15). Now we must assume that all rays are incoherent with each other; put another way, we assume that there is no spatial or temporal coherence between any emitters in the scene. This means that we can calculate the Stokes parameters due to any ray independent of any other ray, then add them at the detector.

Then, the Stokes parameter measured by the detector is a sum over all the rays in the scene, of the Stokes parameter of each ray. Then, for any Stokes parameter S

$$S_{detector} = \sum_{all\,rays} S_{ray} \tag{2.16}$$

2.2 Implementation

We have so far kept the derivation of the physics completely general. This allows us to use any functional form, whether based on first-principles calculations or an empirical model, for every parameter (e.g. χ_{ss}), for every object where the geometrical optics approximation applies. In our simulation, we use as the parameters the results from infinite flat interfaces with infinite-extent plane waves impinging upon them; in this section, we derive these results and present a simple model to extend them to irregular surfaces. We also present a model for the temperature seen by a ray exiting the scene.

The description in this section is still general, and could be applied to any simulation software; changes specific to mmW Blender are given in Section 2.2.9.

2.2.1 Snell's Law

A ray propagating in medium 1, which has refractive index n_1, impinges on an interface with material 2, which has refractive index n_2. Assuming the surface is smooth, the ray is split into two child rays: the reflected ray propagates away from the interface in medium 1, while the refracted ray is transmitted into medium 2 and propagates away from the interface in it; this is shown in Figure 2.3. We wish to know the direction of propagation of the reflected and transmitted rays.

Figure 2.3: Geometry for plane wave interaction with a plane.

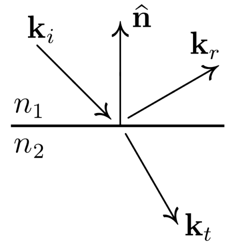

From standard ray optics [11], we know the reflected and transmitted rays are in the plane defined by the incident direction and the normal of the interface. The reflected ray makes the same angle with the surface normal as the incident ray. For the transmitted ray, if the incident ray makes an angle θ_i with the normal of the interface, the angle of refraction θ_t is given by Snell's Law as

$$n_1 \sin\theta_i = n_2 \sin\theta_t \tag{2.17}$$

Equation 2.17 applies generally. However, if either of the materials is lossy (i.e. has a complex refractive index), then the angles must also be complex, and thus lose their simple geometrical meaning. In this section, we derive a vectorial form of Snell's Law in terms of the notation we have previously introduced.

For the remainder of this section, we follow the derivation of Dupertuis *et al.* [12, **?**], changing the notation to align more closely with the one we have already established. We write the wave vectors of the incident, reflected, and transmitted waves as $\mathbf{k}_i$, $\mathbf{k}_r$, and $\mathbf{k}_t$, respectively; note that all three vectors are potentially complex, which is not well illustrated by Figure 2.3. We write the incident, reflected, and transmitted fields as $\mathbf{E}_i = \mathbf{E}_i^0 e^{i(\mathbf{k}_i\cdot\mathbf{r}-\omega t+\phi_i)}$, $\mathbf{E}_r = \mathbf{E}_r^0 e^{i(\mathbf{k}_r\cdot\mathbf{r}-\omega t+\phi_r)}$, and $\mathbf{E}_t = \mathbf{E}_t^0 e^{i(\mathbf{k}_t\cdot\mathbf{r}-\omega t+\phi_t)}$. Without loss of generality, shift our coordinate system such that the interface is given by the plane $\hat{\mathbf{n}}\cdot\mathbf{r} = 0$, where $\hat{\mathbf{n}}$ is the normal to the interface.

One of the boundary conditions for electric fields is the continuity of the tangential electric field. This reduces to the phase matching condition[1]

$$\mathbf{k}_i \times \hat{\mathbf{n}} = \mathbf{k}_r \times \hat{\mathbf{n}} = \mathbf{k}_t \times \hat{\mathbf{n}} \tag{2.18}$$

Equation 2.18 is a vectorial form of Equation 2.17 and reduces to the familiar form for real vectors $\mathbf{k}_i$, $\mathbf{k}_r$, and $\mathbf{k}_t$. We now wish to find an explicit form for $\mathbf{k}_t$. Using Equation 2.18 we write $\mathbf{k}_t$ in terms of the components perpendicular and parallel to the surface as

$$\mathbf{k}_t = k_d \hat{\mathbf{n}} + \hat{\mathbf{n}} \times (\mathbf{k}_i \times \hat{\mathbf{n}}) \tag{2.19}$$

where k_d is an unknown scalar. We apply the dispersion relation, $\mathbf{k}_t \cdot \mathbf{k}_t = k_0^2 n_2^2$, and simplify,

$$k_d = \pm k_0 \sqrt{n_2^2 - n_1^2 \left(\hat{\mathbf{k}}_i \times \hat{\mathbf{n}}\right) \cdot \left(\hat{\mathbf{k}}_i \times \hat{\mathbf{n}}\right)} \tag{2.20}$$

The plus or minus sign is chosen such that $\mathbf{k}_t$ is always pointing in the correct direction relative to the normal, i.e. in the same direction as $\mathbf{k}_i$; care must be taken computationally due to the branch cut in the square root.

For completeness, the reflected wave vector is

$$\mathbf{k}_r = \mathbf{k}_i - 2\left(\mathbf{k}_i \cdot \hat{\mathbf{n}}\right) \hat{\mathbf{n}} \tag{2.21}$$

which trivially satisfies the dispersion relation and Equation 2.18.

2.2.2 Amplitude Reflection and Transmission Coefficients

The reflection and transmission coefficients are computed assuming, as we have previously done, an infinite plane wave incident upon an infinite, smooth interface. We continue the derivation of Dupertuis *et al.* [12, **?**].

[1] For more details, see Appendix B.2.

The full boundary conditions for time-harmonic plane waves are

$$\hat{\mathbf{n}} \times \mathbf{E}_i + \hat{\mathbf{n}} \times \mathbf{E}_r - \hat{\mathbf{n}} \times \mathbf{E}_t = 0 \tag{2.22a}$$

$$\hat{\mathbf{n}} \times \mathbf{H}_i + \hat{\mathbf{n}} \times \mathbf{H}_r - \hat{\mathbf{n}} \times \mathbf{H}_t = 0 \tag{2.22b}$$

$$\varepsilon_1 \hat{\mathbf{n}} \cdot \mathbf{E}_i + \varepsilon_1 \hat{\mathbf{n}} \cdot \mathbf{E}_r - \varepsilon_2 \hat{\mathbf{n}} \cdot \mathbf{E}_t = \Sigma/2 \tag{2.22c}$$

$$\hat{\mathbf{n}} \cdot \mathbf{H}_i + \hat{\mathbf{n}} \cdot \mathbf{H}_r - \hat{\mathbf{n}} \cdot \mathbf{H}_t = 0 \tag{2.22d}$$

where the new term Σ is the surface charge density, which is not necessarily zero; however, if all terms are time-harmonic, on average it is zero. Again, $\hat{\mathbf{n}}$ is the surface normal, and incident, reflected, and transmitted fields are denoted by subscripted i, r, and t, respectively.

We now construct the local $\hat{\mathbf{s}}$-$\hat{\mathbf{p}}$ coordinate system first introduced in Section 2.1.3. Our conditions were that $\hat{\mathbf{s}}$, $\hat{\mathbf{p}}$, and $\hat{\mathbf{k}}$ form an orthogonal triplet. Therefore, it is natural to define

$$\hat{\mathbf{s}} = \frac{\hat{\mathbf{n}} \times \hat{\mathbf{k}}}{\sqrt{(\hat{\mathbf{n}} \times \hat{\mathbf{k}}) \cdot (\hat{\mathbf{n}} \times \hat{\mathbf{k}})}} \tag{2.23a}$$

$$\hat{\mathbf{p}} = \hat{\mathbf{k}} \times \hat{\mathbf{s}} \tag{2.23b}$$

If $\hat{\mathbf{n}}$ and $\hat{\mathbf{k}}$ are collinear (i.e. $\hat{\mathbf{n}} \times \hat{\mathbf{k}} = 0$) we pick $\hat{\mathbf{s}}$ as an arbitrary vector perpendicular to $\hat{\mathbf{n}}$.

Note that this definition allows us to keep the same $\hat{\mathbf{s}}$ for the incident, reflected, and transmitted rays. In general $\hat{\mathbf{k}}$ is complex, so both $\hat{\mathbf{s}}$ and $\hat{\mathbf{p}}$ will also be complex. We can decompose the fields as described in Section 2.1.3: $\mathbf{E} = E_s\hat{\mathbf{s}} + E_p\hat{\mathbf{p}}$, $\mathbf{H} = H_s\hat{\mathbf{p}} + H_p\hat{\mathbf{s}}$ (the s and p subscripts apply to the orientation of the *electric* field) and compute the amplitude reflection coefficients[2] for s and p polarizations as

$$r_s = \frac{E_{s,r}}{E_{s,i}} = \frac{\mathbf{k}_i \cdot \hat{\mathbf{n}} - \mathbf{k}_t \cdot \hat{\mathbf{n}}}{\mathbf{k}_i \cdot \hat{\mathbf{n}} + \mathbf{k}_t \cdot \hat{\mathbf{n}}} \tag{2.24a}$$

$$r_p = \frac{H_{p,r}}{H_{p,i}} = \frac{\varepsilon_2 \mathbf{k}_i \cdot \hat{\mathbf{n}} - \varepsilon_1 \mathbf{k}_t \cdot \hat{\mathbf{n}}}{\varepsilon_2 \mathbf{k}_i \cdot \hat{\mathbf{n}} + \varepsilon_1 \mathbf{k}_t \cdot \hat{\mathbf{n}}} \tag{2.24b}$$

[2] For a complete derivation, see Appendix B.3

and the amplitude transmission coefficients as

$$t_s = \frac{E_{s,t}}{E_{s,i}} = 1 + r_s = \frac{2\mathbf{k}_i \cdot \hat{\mathbf{n}}}{\mathbf{k}_i \cdot \hat{\mathbf{n}} + \mathbf{k}_t \cdot \hat{\mathbf{n}}} \tag{2.25a}$$

$$t_p = \frac{H_{p,t}}{H_{p,i}} = 1 + r_p = \frac{2\varepsilon_2 \hat{\mathbf{n}} \cdot \mathbf{k}_i}{\varepsilon_2 \mathbf{k}_i \cdot \hat{\mathbf{n}} + \varepsilon_1 \mathbf{k}_t \cdot \hat{\mathbf{n}}} \tag{2.25b}$$

Note that $r_p < r_s$ for most incidence angles.

We have already defined $k_d = \mathbf{k}_t \cdot \hat{\mathbf{n}}$ (Equation 2.19), and can use a similar form for $\mathbf{k}_i \cdot \hat{\mathbf{n}}$. However, this does not significantly simplify the above expressions.

2.2.3 Multilayer Stack

Having solved the case of wave interaction with a single interface, we now consider a set of $N-1$ parallel interfaces, with a wave incident upon them. The $N-1$ interfaces form the boundaries of a stack of $N-2$ layers between the first and last medium, which are assumed to continue to infinity. Such a problem arises when attempting to simulate thin objects, such as clothing or a pane of glass (where $N=3$ and the two surrounding media are both air), or layered objects, such as human skin (with a layer for the epidermis, the dermis, and subcutaneous tissue, each with its own set of material properties, thickness, and temperature). The media are enumerated 1 to N, and material m is said to have a refractive index n_m; additionally, if it is not the first or last medium, it has thickness d_m.

Unlike previous calculations, we consider the field to be propagating coherently between interfaces, such that interference between forward and backward-traveling waves is possible; this is reasonable if the total thickness of the stack is considerably smaller than the coherence length of the radiation.

To solve for this case, we again use a transfer matrix formalism. We note that there are two basic forms of interaction between the wave and the dielectric stack which change the magnitude and phase of the wave. The first, propagation across a layer, is shown in Figure 2.4a. The second, shown in Figure 2.4b, is interaction with some interface. Figure 2.4c summarizes the notation we will use for the remainder of this section: a superscript + indicates that the wave propagates in the direction of increasing

Figure 2.4: Schematic diagram of field propagation in a multi-layer stack of materials.

(a) Propagation through a single layer.

(b) Propagation across an interface.

(c) Propagation through a many-layered structure.

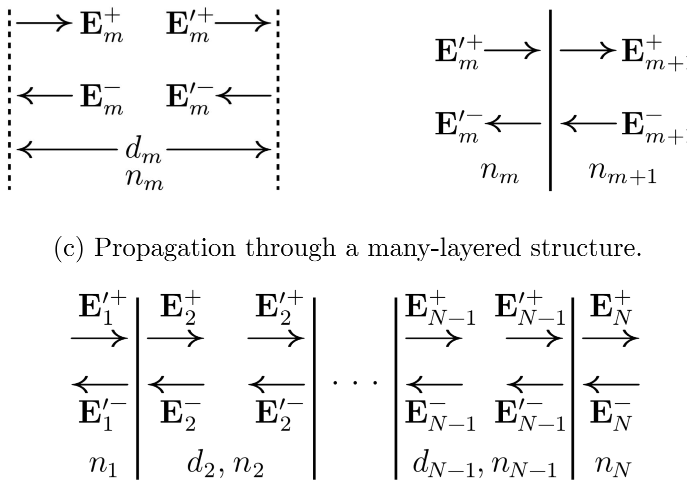

layer number (right, in the diagram), and a superscript $-$ indicates the inverse; a prime ($'$) indicates the field evaluated immediately on the left (lower layer number) side of an interface, while an unprimed field is evaluated on the right (higher layer number). Note that though we have drawn the direction of field propagation as normal to the interface, nothing in the derivation limits us to only this case, and the results presented here are general for all directions of field propagation.

Considering the case of propagation, we can write for the forward-going wave, using Equation 2.2,

$$\mathbf{E}_m^+ = \mathbf{E}_{m0}^+ e^{i(\mathbf{k}_m\cdot\mathbf{r}-\omega t)} \tag{2.26a}$$

$$\mathbf{E}_m'^+ = \mathbf{E}_{m0}^+ e^{i[\mathbf{k}_m\cdot(\mathbf{r}+\hat{\mathbf{n}}d_m)-\omega t]} \tag{2.26b}$$

where $\mathbf{r}$ has been restricted to the interface. Note that we have implicitly defined the normal vector $\hat{\mathbf{n}}$ as pointing to the right; we will continue with this convention; also note that the only difference between the terms is a factor of $e^{i\mathbf{k}\cdot\hat{\mathbf{n}}d_m}$; in Equation 2.19 we defined $k_d = \mathbf{k}\cdot\hat{\mathbf{n}}$; substituting this and following the same procedure for the back-propagating wave $\mathbf{E}_m^-$, we write the final transfer matrix for propagation as

$$\begin{pmatrix} \mathbf{E}_m'^+ \\ \mathbf{E}_m'^- \end{pmatrix} = \begin{pmatrix} e^{ik_{dm}d_m} & 0 \\ 0 & e^{-ik_{dm}d_m} \end{pmatrix} \begin{pmatrix} \mathbf{E}_m^+ \\ \mathbf{E}_m^- \end{pmatrix} = \mathbf{P}_m \begin{pmatrix} \mathbf{E}_m^+ \\ \mathbf{E}_m^- \end{pmatrix} \tag{2.27}$$

For the case of interactions at an interface (Figure 2.4b), we can write the waves propagating away from the interface in terms of waves propagating towards it

$$\mathbf{E}_{m+1}^+ = r_{m+1,m}\mathbf{E}_{m+1}^- + t_{m,m+1}\mathbf{E}_m'^+ \tag{2.28a}$$

$$\mathbf{E}_m'^- = r_{m,m+1}\mathbf{E}_m'^+ + t_{m+1,m}\mathbf{E}_{m+1}^- \tag{2.28b}$$

where $r_{m,m+1}$ is the reflection coefficient from medium m to medium $m+1$, $t_{m+1,m}$ is the transmission coefficient from medium $m+1$ to medium m, and so forth. After some algebra, this reduces to the transfer matrix for transmission,

$$\begin{pmatrix} \mathbf{E}_{m+1}^+ \\ \mathbf{E}_{m+1}^- \end{pmatrix} = \frac{1}{t_{m+1,m}} \begin{pmatrix} 1 & r_{m+1,m} \\ r_{m+1,m} & 1 \end{pmatrix} \begin{pmatrix} \mathbf{E}_m'^+ \\ \mathbf{E}_m'^- \end{pmatrix} = \mathbf{T}_{m,m+1} \begin{pmatrix} \mathbf{E}_m'^+ \\ \mathbf{E}_m'^- \end{pmatrix} \tag{2.29}$$

which holds true for both s and p polarizations, using the appropriate amplitude reflection and transmission coefficients. Finally, we combine these according to Figure 2.4c and obtain the transfer matrix for the entire stack

$$\begin{pmatrix} \mathbf{E}_N^+ \\ \mathbf{E}_N^- \end{pmatrix} = \left[\prod_{j=N}^{3} \mathbf{T}_{j-1,j}\mathbf{P}_{j-1} \right] \mathbf{T}_{1,2} \begin{pmatrix} \mathbf{E}_1'^+ \\ \mathbf{E}_1'^- \end{pmatrix} = \begin{pmatrix} L_{00} & L_{01} \\ L_{10} & L_{11} \end{pmatrix} \begin{pmatrix} \mathbf{E}_1'^+ \\ \mathbf{E}_1'^- \end{pmatrix} \tag{2.30}$$

From the transfer matrix $\mathbf{L}$ in Equation 2.30, we extract the reflection coefficients; we do this by considering the ray to be originating in medium N and setting $\mathbf{E}_N^- = 1$, $\mathbf{E}_N^+ = r$, $\mathbf{E}_1'^- = t$, and $\mathbf{E}_1'^+ = 0$ in Equation 2.30. This leads to the simple expression for reflection and transmission through a stack of thin materials

$$r = \frac{L_{01}}{L_{11}} \tag{2.31a}$$

$$t = \frac{1}{L_{11}} \tag{2.31b}$$

which, again, applies for both polarization states.

We note as an aside that this formalism is used in the free-space determination of mmW dielectric properties of material samples [13, 14, 15].

2.2.4 Power Propagation and Power Reflection and Transmission Coefficients

We have so far been manipulating field quantities and wave vector $\mathbf{k}$. However, as mentioned previously, a mmW imager measures time-averaged power. Therefore, we must evaluate the properties associated with power flow, rather than the wave vector or field quantities. Average power flow is given by the Poynting vector

$$\mathbf{S} = \frac{1}{2}\mathfrak{Re}\left\{\mathbf{E} \times \mathbf{H}^*\right\} \tag{2.32}$$

Taking $\mathbf{E}$ to have the form given in Equation 2.2 and evaluating $\mathbf{H}^*$ using Maxwell's equations, the power flux for a time-harmonic inhomogeneous plane wave is[3]

$$\mathbf{S} = \frac{1}{2\omega\mu_0} e^{2\mathfrak{Im}\{\mathbf{k}\}\cdot\mathbf{r}} \left[\left(\mathbf{E}_0 \cdot \mathbf{E}_0^*\right)\mathfrak{Re}\left\{\mathbf{k}\right\} - i\mathfrak{Im}\left\{\mathbf{k}\right\} \times \left(\mathbf{E}_0 \times \mathbf{E}_0^*\right)\right] \tag{2.33}$$

This form of the Poynting vector is problematic several reasons. First, the power flux in a ray decreases (or increases, though we do not consider this in the passive case) in the direction of $\mathfrak{Im}\left\{\mathbf{k}\right\}$; this is not necessarily the same as the direction of power propagation; in fact, Equation 2.33 explicitly shows that the direction of power flux has a component perpendicular to $\mathfrak{Im}\left\{\mathbf{k}\right\}$ (though this component will be zero if $\mathbf{E}_0 \times \mathbf{E}_0^* = 0$, as is the for a homogeneous wave or a wave in a lossless medium). This means that Beer's Law does not apply in general, which is problematic from a phenomenological standpoint. Moreover, we see that the direction of propagation depends not only on the homogeneity of the wave but also, for an inhomogeneous wave, its polarization state. This means it is possible to construct multiple waves propagating in the same direction, but that will refract in different directions when they interact with a material. We also note, incidentally, that once a wave becomes inhomogeneous through interactions with materials, it is difficult to make it homogeneous again.

Due to these facts, the ray tracing approach described in Section 2.1.1 is fundamentally incompatible with the behavior of inhomogeneous plane waves.

---

[3] See Appendix B.4 for a full derivation.

This is because for ray tracing to work, we must make an assumption about the properties of the ray at the detector, rather than the emitting in the scene. We only know that some wave with power flow along the launched ray vector makes its way to the detector; if we make the guess that this wave is homogeneous at the detector, then attempt to propagate back to the point where it entered the scene, we could very well find that the wave is no longer homogeneous (e.g. because it was transmitted through a lossy material between two surfaces that were not parallel), and that its k-vector does not match that of the wave we know enters the scene at that point; that is, the back-propagating approach does not match the boundary conditions.

To resolve this, we could attempt to find a inhomogeneous vector at the camera that, when propagated back to its origin, would match the boundary condition; however, any optimization algorithm to do this would fail because the problem space is pathologically not smooth. We must first guess at an inhomogeneous k-vector that gives the same direction of power flow—an infinite number of possibilities exist, but finding them is not trivial, given Equation 2.33—and then propagate it back. However, an inhomogeneous wave will have a different direction of power propagation (the quantity we care about) after interacting with a surface, so its path will diverge from the original homogeneous ray after some interactions; it will end up originating at a different point in the scene, having interacted with different surfaces, and still not satisfying the boundary condition. On top of this, a small perturbation in propagation direction will lead to vastly different end points, because the direction of power propagation after a surface interaction also depends on the surface normal and the surface normals vary discontinuously; even if they did not, the objects do: a ray might barely hit an object at a glancing angle, while a slightly offset neighbor would miss the object entirely.

Attempting to satisfy the boundary conditions for inhomogeneous waves using back-propagating waves from the camera, then, is hopeless. We instead resolve this problem by making one more assumption: all propagating waves are homogeneous. That is, in the expression $\mathbf{k} = k\hat{\mathbf{k}}$, $\hat{\mathbf{k}}$ is always real. We justify this with the observation that inhomogeneous waves are produced from homogeneous waves by transmission through a lossy material (the more lossy the material, the more inhomogeneous the wave), so we expect that most waves carrying any significant amount of energy will be mostly homogeneous.

Note that this immediately implies both that Beer's Law holds and that power propagates in the direction of $\hat{\mathbf{k}}$.

Then, analogously to the amplitude reflection coefficients of Section 2.2.2, we can write the reflection and transmission coefficients for power flux[4]

$$R_s = r_s^* r_s \tag{2.34a}$$

$$R_p = r_p^* r_p \tag{2.34b}$$

$$T_s = t_s^* t_s \mathfrak{Re}\left\{\frac{k_{d,t}^*}{k_{d,i}^*}\right\} \tag{2.34c}$$

$$T_p = t_p^* t_p \mathfrak{Re}\left\{\frac{k_{d,t}^*/\varepsilon_i}{k_{d,i}^*/\varepsilon_t}\right\} \tag{2.34d}$$

where r and t are the amplitude reflection and transmission coefficients from Equations 2.24 and 2.25 and ε_i and ε_t are the dielectric constants on the incident and transmition side of the interface. These equations apply to materials with a thin coating applied, if one uses r and t from Equation 2.31 instead.

Note that for a series of layered materials, if any layers are lossy it is possible that $R + T < 1$. It is also possible, if the layers in the stack are less lossy than the medium the field originates from, that at glancing angles $R + T > 1$. This is because the low-loss layer acts effectively as a waveguide, moving incident power "downstream" in a channel that is less lossy than the surrounding media. Therefore, the reflected field will be comprised of both the reflection from the incident field at that point, and energy from "upstream." This is not a desired result for simulation; therefore, if it occurs, we scale R and T such that $R + T = 1$.

Figure 2.5: Flowchart for the ray tracing algorithm.

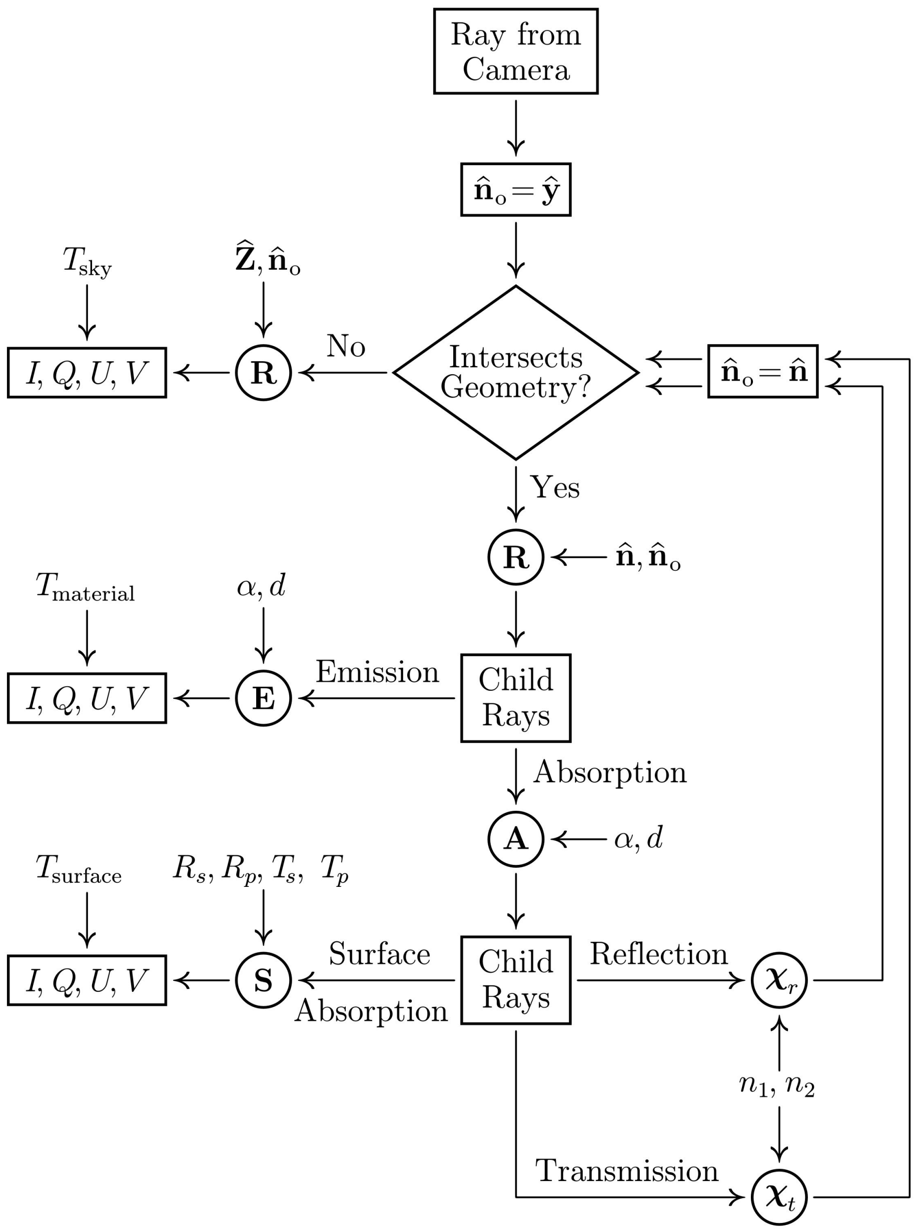

2.2.5 Ray Tracing

Having made the assumption that all propagating waves are homogeneous, we can now describe the ray tracing procedure in mmW Blender.

The ray tracing algorithm is described schematically in Figure 2.5; arrows track the $\mathbf{M}$ matrix from Equation 2.11b associated with a ray as it propagates through the scene. At the camera $\mathbf{M}$ is initialized to the identity matrix. Every circular block multiplies the $\mathbf{M}$ matrix by a corresponding matrix based on Equation 2.10c; these are explained in detail below. The algorithm iterates recursively until the ray exits the scene or is otherwise terminated.

The "Child Ray" blocks split off child rays and working copies of the matrix and pass them along instead of the original; the new $\mathbf{k}$ vectors are also calculated where necessary.

At every "I, Q, U, V" block, we compute the Stokes parameters for the current $\mathbf{M}$ matrix and ray temperatures according to Equation 2.15, then terminate the ray tracing and add the ray's contribution to the pixel's Stokes parameters. The ray temperature can be T_{material}, the bulk temperature of the object, T_{surface}, the temperature of any coating layer applied to the material (which is not necessarily the same as T_{material}), or T_{sky}, the temperature of a ray entering the scene. T_{sky} is usually a function of the direction the ray leaves the scene, and can be polarized as in Equation 2.5; more details are given in Section 2.2.7. For surface and material emission, we take $A = B = T$.

Additionally, in order to prevent infinite recursions, the ray tracing is set to terminate after a user-defined recursion level is reached; this is not illustrated in the flowchart. The terminating temperature in this case is that of the last object the ray interacted with.

The matrix $\mathbf{R}$ is the rotation matrix from one set of local coordinates to another.

[4] The derivation of these terms is found in Appendix B.5

It is written as

$$\mathbf{R} = \begin{pmatrix} \hat{\mathbf{s}}_\text{o} \cdot \hat{\mathbf{s}} & \hat{\mathbf{p}}_\text{o} \cdot \hat{\mathbf{s}} \\ \hat{\mathbf{s}}_\text{o} \cdot \hat{\mathbf{p}} & \hat{\mathbf{p}}_\text{o} \cdot \hat{\mathbf{p}} \end{pmatrix} \tag{2.35}$$

with $\hat{\mathbf{s}}$ and $\hat{\mathbf{p}}$ calculated from $\hat{\mathbf{n}}$ and $\hat{\mathbf{s}}_\text{o}$ and $\hat{\mathbf{p}}_\text{o}$ calculated from $\hat{\mathbf{n}}_\text{o}$ according to Equation 2.23, where $\hat{\mathbf{n}}$ and $\hat{\mathbf{n}}_\text{o}$ are vectors normal to the current and previously encountered surface, respectively. For rays escaping the scene, we introduce the vector $\hat{\mathbf{Z}}$, the z-axis in global (i.e. world) coordinates; recall that $\hat{\mathbf{x}}$ and $\hat{\mathbf{y}}$ were defined in terms of local imager coordinates, and can be oriented in any direction in world space. The use of a global $\hat{\mathbf{Z}}$ allows us to consistently describe the polarization of rays from outside the scene, independent of the imager orientation.

In the case of a coating comprised of lossy layers, the surface itself might be absorptive; this is accounted for in the "Surface" child ray, which considers the loss (and therefore emission) equal to the amount not reflected from or transmitted through the surface. That is, in terms of the power reflection coefficients of Equation 2.34

$$\mathbf{S} = \begin{pmatrix} \sqrt{1 - R_s - T_s} & 0 \\ 0 & \sqrt{1 - R_p - T_p} \end{pmatrix} \tag{2.36}$$

The square root is due to considering fields rather than powers (i.e. the terms are squared to obtain powers in Equation 2.15).

The absorption matrix $\mathbf{A}$ is based on the propagation matrix $\mathbf{P}$ from Equation 2.10c; knowing that we will be evaluating time-averaged powers allows us to simplify the the expression

$$\mathbf{A} = \begin{pmatrix} e^{-\alpha d/2} & 0 \\ 0 & e^{-\alpha d/2} \end{pmatrix} \tag{2.37}$$

where $\alpha = 2\mathfrak{Im}\left\{k\right\}$ is the absorption coefficient of the medium and d is the distance traveled. The factor of $1/2$ in the exponential is again to ensure the appropriate behavior of the power.

The emission matrix is closely related, in the sense that any absorbed energy is emitted at the temperature of the absorbing medium. Thus, we write

$$\mathbf{E} = \begin{pmatrix} \sqrt{1 - e^{-\alpha d}} & 0 \\ 0 & \sqrt{1 - e^{-\alpha d}} \end{pmatrix} \tag{2.38}$$

again making sure that the magnitude squared gives the appropriate value for emission.

The reflection and transmission matrices $\boldsymbol{\chi}_r$ and $\boldsymbol{\chi}_t$ are formulated such that taking the complex magnitude squared gives the appropriate reflection and transmission coefficients from Equation 2.34. Thus

$$\boldsymbol{\chi}_r = \begin{pmatrix} r_s & 0 \\ 0 & r_p \end{pmatrix} \tag{2.39}$$

$$\boldsymbol{\chi}_t = \begin{pmatrix} t_s \sqrt{\mathfrak{Re}\left\{\frac{k^*_{d,t}}{k^*_{d,i}}\right\}} & 0 \\ 0 & t_p \sqrt{\mathfrak{Re}\left\{\frac{k^*_{d,t}/\varepsilon_{r,i}}{k^*_{d,i}/\varepsilon_{r,t}}\right\}} \end{pmatrix} \tag{2.40}$$

We use r and t rather than $\sqrt{rr^*}$ or $\sqrt{tt^*}$ because r or t can be complex (indicating a relative phase shift) and it is important to preserve that.

Once ray tracing of all child rays terminates, the final value of the Stokes parameters are returned for that pixel. After all pixels have been evaluated, the simulation terminates. Finally, the image is normalized such that it can be displayed on a computer monitor.

2.2.6 Non-glossy Surfaces

All calculations so far have assumed a mirror-smooth surface between materials; while this is a good approximation for many man-made materials, it notably fails for dirt, grass, and other natural surfaces. Therefore, in order to simulate outdoor scenes, we need a model for reflection and transmission through rough surfaces. The purpose of the model presented here is not complete accuracy or fidelity, but rather it is to be a reasonable, usable approximation while we collect further data and develop a more accurate model.

We base the rough surface model from a non-glossy reflection model that Blender has built-in; it is based upon perturbing the normal of the surface the ray hits, then computing the ray propagation (reflection and transmission) based on this perturbed normal; multiple samples are computed and the results are averaged per-pixel, simulating sub-pixel roughness.

The specific procedure Blender uses is as follows: we assume without loss of generality that the surface normal $\hat{\mathbf{n}}$ points in the $\hat{\mathbf{z}}$ direction. The perturbed normal is given by $\hat{\mathbf{n}}' = (\hat{\mathbf{n}} + \mathbf{v}) \, / \, |\hat{\mathbf{n}} + \mathbf{v}|$; we choose the perturbing vector $\mathbf{v} = r \, (\hat{\mathbf{x}} \cos \phi + \hat{\mathbf{y}} \sin \phi)$, where ϕ uniformly sampled from the interval $[0, 2\pi)$ and $r = \sqrt{1 - b^{2L}}$, where b is uniformly sampled[5] on the interval $[0, 1)$ and $L = (1 - g)^3$, where g is the gloss parameter; if $g = 1$, the surface is completely glossy, if $g < 1$, the surface becomes increasingly rough-looking, with reflected and transmitted images becoming increasingly blurry; a check is performed to ensure the reflected or transmitted rays end up on the appropriate side of the surface.

As with many models in computer graphics, this particular form of the perturbed normal was chosen because it gave aesthetically pleasing results, rather than because it is physically accurate. Unfortunately, creating a more accurate model is beyond the scope of this thesis; such a model can be easily plugged in to the simulation code once it is developed, however.

2.2.7 Sky Model

We require a model for the temperature of a ray entering the scene, called T_{sky} above. We require this information as a function of ray direction. Here we present a model for estimating T_{sky} for an outdoor terrestrial scene [16].

First, we expect that, in the absence of atmosphere, the temperature would be a uniform 3 K due to the cosmic microwave background. The presence of atmosphere

---

[5] As is often the case, better results for less computation time are achieved by using a quasi-random point set, rather than random sampling. Blender uses the Hammersley point set for this purpose, but any method of generating uniform values on the interval $[0, 1)^2$ is acceptable.

would tend to increase the temperature toward that of the atmosphere, in proportion to the distance traveled; thus, we would expect that the sky is coldest at zenith and approaches ambient temperature near the horizon.

We simulate the atmosphere as a series of N layers, each with its own temperature and composition. For each layer, we calculate an absorption coefficient α based on the frequency and the gas composition. Then the temperature of a ray in the $j+1^{\text{th}}$ layer (counting from the top of the atmosphere down) is given by the recurrence relation

$$T_{j+1} = T_j e^{-\alpha_j d_j} + T_j^l \left(1 - e^{-\alpha_j d_j}\right)$$

where T_j^l, α_j, and d_j are the temperature, absorption coefficient, and distance traveled within the j^{th} layer, respectively. The initial condition is $T_0^l = 3\,\text{K}$, the cosmic background temperature. The viewing angle is adjusted for by increasing d_j, taking the curvature of the earth into account; the presence of clouds is modeled by adjusting the absorption coefficient due to liquid water in the layers with the clouds present; the temperature and composition of each layer is obtained from the lapse rates of each quantity, for which there are meteorological models [17] [18].

The results of applying this model are shown in Figure 2.6. In this range, the absorption peaks are due to water and oxygen. This manifests as both a higher absorption coefficient and higher temperature near the absorption peaks. The atmospheric windows at 35 GHz and 77 to 95 GHz are clearly visible.

2.2.8 Imager Model

The simulation we have described produces a perfect image, of the sort that one would see through an infinitely-sensitive camera that simultaneously avoids diffraction and depth of field effects. The simulated image has no limits on resolution or resolvable feature size, only on the number of pixels we are willing to wait to simulate. A real-world imager is not so ideal. The approach we take is to compute a point spread function (PSF) for the imager we wish to simulate, then convolve the simulated image with it; this is in general complicated because the PSF is dependent on not only the imager,

Figure 2.6: Atmospheric model under various weather conditions.

(a) Propagation loss at sea level.

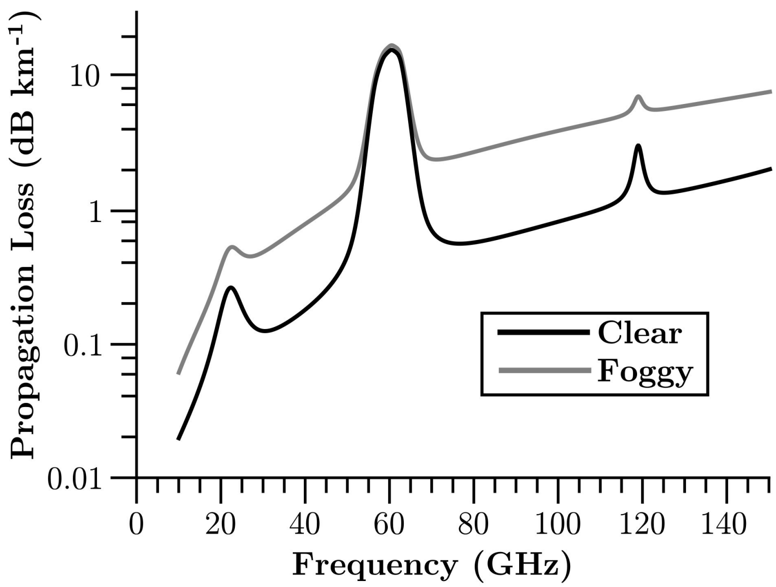

(b) Zenithal sky temperature.

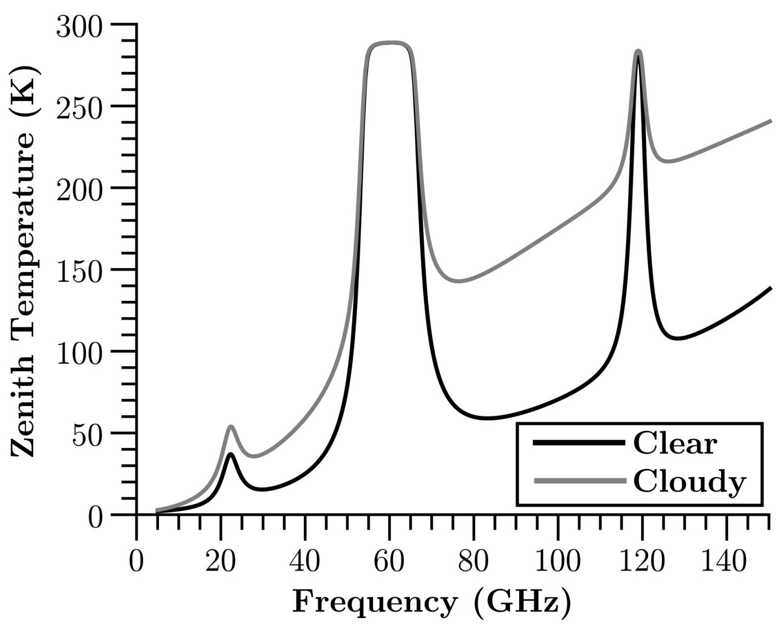

but also the frequency and position in the image that one considers. For the purpose of this work, we use the Airy disk PSF [11]

$$I(\theta) = \left[\frac{2J_1(ka\sin\theta)}{ka\sin\theta}\right]^2 \tag{2.41}$$

where θ is the angle between the center-line of the image and a blurring pixel, a is the radius of the aperture, k is the wavenumber, and J_1 is a Bessel function of the first kind, of order 1. We compute the convolution of this with the image assuming that it is the PSF applies for every pixel in the image and that the angle between every pixel is the same; these assumptions are reasonably accurate so long as the imager field of view is small.

Real imagers also have noise from various physical processes; we again choose the simplest possible model: we apply an additive Gaussian noise with the appropriate noise temperature (corresponding to the standard deviation of the Gaussian curve) to every pixel in the final image.

2.2.9 Implementation-Specific Features

Here we describe simulation features specific to the implementation of mmW Blender.

When a ray enters a material, it refracts and propagates according to the properties of that material; when it exits, it refracts and propagates based on the properties of the medium it was traveling in, and the new medium—which might be atmosphere. The interaction of a ray with a surface, then, requires two pieces of information: the properties of the medium it originated in, and the properties of the medium it is impinging upon. However, Blender is based upon polygons, with no concept of a solid object; therefore, we must determine the properties of the media on either side of the interface, knowing (at most) the properties of the surface and the properties of the surfaces the ray has previously interacted with. The process of determining these is based on assuming that every solid object has a surface that is a closed, orientable manifold, and is best illustrated with an example.

Consider a ray propagating in free space, encountering a surface with material A. The ray splits into a reflected and a transmitted ray, the reflected ray continuing in free space, the transmitted ray in medium A. The transmitted ray propagates some distance, then encounters another surface, where it splits again into a reflected and a transmitted ray; the reflected ray continues in medium A. If the material of the surface is also A, the transmitted ray is assumed to leave medium A and is now propagating in free space again. If the surface has material B, however, the transmitted ray is now assumed to be propagating in medium B; additionally, the next surface the transmitted ray encounters is assumed to have material A (because every object is closed and orientable, every ray that enters an object must eventually leave it), so it is ignored and the ray continues propagating without any interaction. This means that to have a ray propagate from medium A to medium B, two closed objects with material A and B must be brought in contact such that they are very slightly interpenetrating.

This creates a nonphysical situation where rays travel a different distance in each material depending on which side of the interface they originate from; additionally, there are errors around the corner of a penetrating object at certain angles; both of these can be minimized by making the penetration depth as small as possible. Even with these errors, this is the cleanest solution, as other possibilities would require either more work for the user, or considerably more program logic.

Thin coating layers can be added to a material as described in Section 2.2.3. The coating layers are evaluated as though the incident radiation was fully coherent; this accurate for layers that are much thinner than the coherence length $c/\Delta f$ where Δf is the bandwidth. As the imager bandwidth cannot be set for the simulation, it is left up to the user to ensure the total coating thickness does not become too large. The order the coating layers are evaluated depends on whether the ray is found to be entering or leaving the material.

We also allow four additional material properties to be selected by the user. Materials can be set to be: metal, in which case the material is perfectly reflective at all angles, with $r_s = -1$ and $r_p = 1$; blackbody, in which case the material is perfectly absorptive at all incidence angles, with $r_s = r_p = 0$, $t_s = t_p = 1$, and the absorption $\alpha = \infty$; opaque, in which case r_s and r_p are computed as normal, but $t_s = t_p = 0$ at all angles; and thin, in which case the material is considered to be only a series of thin sheets, and the transmitted ray keeps the properties of the incident medium. We take an opaque metal to behave as a metal, an opaque blackbody or metal blackbody to behave as a blackbody, and a thin metal and blackbody to still behave as a metal and blackbody, respectively. Each of these surface types can have a coating applied to it; in this case, the reflection and transmission coefficients are set in the leftmost matrix in Equation 2.30, and all other matrices are evaluated as normal.

We allow the user to change the parameters of the atmosphere. The user can set the loss (in $\mathrm{dB\,km^{-1}}$) as well as the temperature. The sky model of Section 2.2.7 is implemented by allowing the user to set the temperature in each polarization of a ray leaving the scene, as a function of direction. This allows the sky model to be computed off-line and applied as a texture map.

Finally, we we allow the user to set the maximum number of levels of recursion, limiting the number of times any particular ray can interact with the scene. Three or four bounces is typically enough to capture most of the phenomenology, though more might be necessary in a complicated scene with many non-lossy objects. The user also has the option for restricting the number of bounces using a threshold: if the total contribution to the image of a particular ray is less than the threshold, the rendering for that ray is terminated.

2.3 Validation

In this section we discuss the validation of the simulation techniques by comparison to experimentally measured images. We first describe the mmW imaging system used to obtain the experimental data, then describe several test scenes and compare the simulation of these scenes to experimental data. All material parameters used in the simulations are also provided.

2.3.1 Scanning Cart

We first briefly describe the imaging system used to collect the experimental data.

The imager, built at the University of Delaware, operates in the $\mathrm{K_a}$ band, though the spectral response is not well-characterized; we assume, for the purposes of simulation, that it is monochromatic at 35 GHz. It is a single pixel detector, consisting of a horn antenna mounted in a focusing dish. The dish is mounted on a set of computer-controlled gimbals, which provides freedom of movement in the azimuthal and zenithal directions. An image is produced by raster-scanning the detector across scene, collecting data at each pixel; the process takes several minutes. The imager has a dish diameter of 0.6 m, and has been found to be nearly diffraction-limited, so the Airy disk point spread function given in Equation 2.41 is expected to apply. It is capable of simultaneously capturing x and y polarizations, with a 2 K noise figure per polarization; it does not capture the Stokes parameters, however. The scanning antenna, associated hardware, and control electronics are mounted in a wheeled cart for ease of transport.

More details about the imager can be found in [5], and a detailed description of the principles behind its operation in [3].

Finally, we note that though the focal depth is adjustable, meaning that in theory every pixel of a collected image could be in focus, in practice the focal depth is set to one particular value for the entire image; the focal depth was set to 7 m for every image in the validation set. There are, unfortunately, no fast ways to accurately simulate depth-of-field effects (though several algorithms exist for producing visually-convincing approximations), so this was not done for the simulated images.

2.3.2 Cinderblocks

We begin with a relatively simple scene: a stack of cinderblocks in a desert environment. A visible image of the scene is shown in Figure 2.7a. The surroundings are open and flat, with no significant structures nearby. A list of the material properties of objects in the scene is given in Table 2.1.

Figure 2.7: Cinderblocks in the desert at visible wavelengths and 35 GHz.

(a) Visible image of cinderblocks.

(b) x-polarized image of cinderblocks.

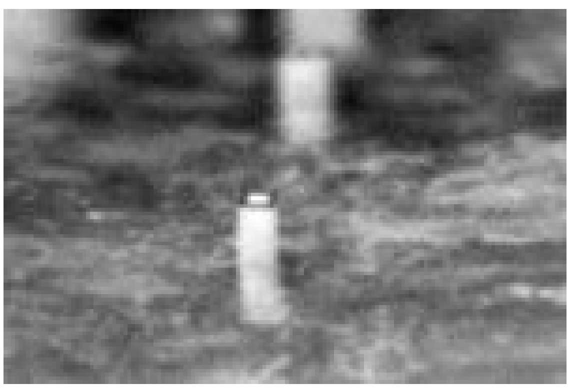

(c) x-polarized simulated image of cinderblocks.

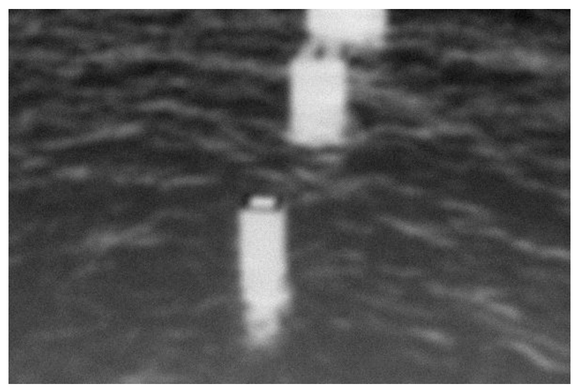

(d) y-polarized image of cinderblocks.

(e) y-polarized simulated image of cinderblocks.

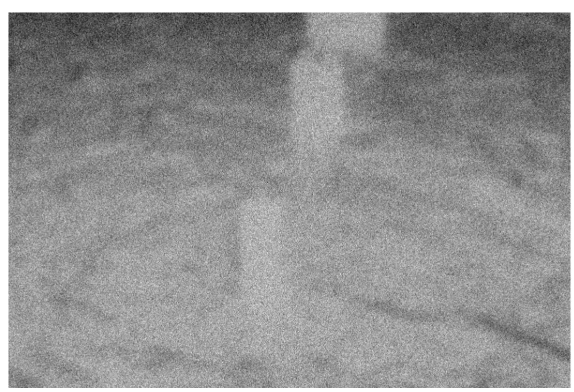

Table 2.1: Material properties used in the Cinderblocks scene

Object	ε_r'	ε_r''	Temperature (K)	Notes
Cinderblock	5.5	0.5	300	Concrete [19]
Ground	3.9	0.56	300	Sand [19]

The experimental data in the x polarization, shown in Figure 2.7b, has several interesting features. First, there is no clear boundary between the cinderblock and its reflection from the ground. Second, the top of the cinderblock is very cold; this is because it produces a nearly-specular reflection of the cold sky. Finally, the cavity inside the cinderblock is very warm. All of these are reproduced in the simulated image in Figure 2.7c, for both the near and far cinderblock. In the y polarization, shown in Figure 2.7d, the reflection coefficient is much lower, since the imager $\hat{\mathbf{y}}$ coordinate is along the $\hat{\mathbf{p}}$ direction of the local coordinate system; the lower reflection from the sky leads to a dramatically decreased contrast, and complete disappearance of the cinderblocks; the simulation, shown in Figure 2.7e, captures this behavior.

Turning our attention to the ground, rather than modeling it as a flat plane, a texture affecting the direction of the surface normal is applied to it; this changes the relative power of the reflections, and simulates the ground being bumpy. Though it is not perfect, this basic ground model already is a good match for the real ground. It could be improved by adding ground clutter, or having different areas of the ground be warmer or cooler, depending on, e.g., the color in visible wavelengths.

Using this relatively simple scene, we have demonstrated the basic capabilities of the simulation software. We have also demonstrated that it is possible to use experimental data for material properties to produce a highly accurate simulated pmmW image. We have also demonstrated it is possible to use a relatively simple model (a flat plane with a texture map) to accurately simulate the complex phenomenology of reflection from a rough surface.

Table 2.2: Material properties used in the Truck scene

Object	ε_r'	ε_r''	Temperature (K)	Notes
Truck Body	N/A	N/A	N/A	Metal
Tires	7.7	0.38	300	SA-9 tire [21]
Interior	2.2	0.06	300	Leather [13]
Ground	3.9	0.56	300	Sand [19]

2.3.3 Truck

The next scene we consider is a truck in a desert environment. A visible image of the scene is shown in Figure 2.8a. Again, the surroundings are open and flat. The truck in the simulated images is based on a publicly-available 3d model [20]. A list of the material properties of objects in the scene is given in Table 2.2.

The experimentally measured x-polarized image is shown in Figure 2.8b, with the corresponding simulation in 2.8c; there is some detail seen in the reflections from the side of the truck body, though it is too distorted to make out clearly. The reflection of the truck is clearly visible in the ground, appearing as a bright cavity where rays are trapped in the underside of the truck. We again see in the y polarized images (Figures 2.8d and 2.8e) that the reflections from the ground are washed out and all ground features are lost; it does not affect the contrast in this scene as much, however, because the metal remains reflective at both polarizations; these horizontal surfaces are the coldest portions of the scene at both polarizations. We also see that there are cavities in the wheel wells and the cab, which show up comparatively warm, in both simulation and experiment. In fact, where simulation and experiment differ, the differences are minor and attributable to the scene geometry (i.e. the 3D model of the truck and the positioning of the camera).

For the ground we used the simple model introduced in the Cinderblocks scenario in Section 2.3.2. Again, though it could be improved, it is a good first approximation for the behavior of dirt at 35 GHz.

We have again demonstrated the ability to populate a scene with objects, assign experimentally determined material properties to those objects, and run the simulation

Figure 2.8: A pickup truck in the desert at visible wavelengths and 35 GHz.

(a) Visible image of a pickup truck.

(b) x-polarized image of a pickup truck.

(c) x-polarized simulated image of a pickup truck.

(d) y-polarized image of a pickup truck.

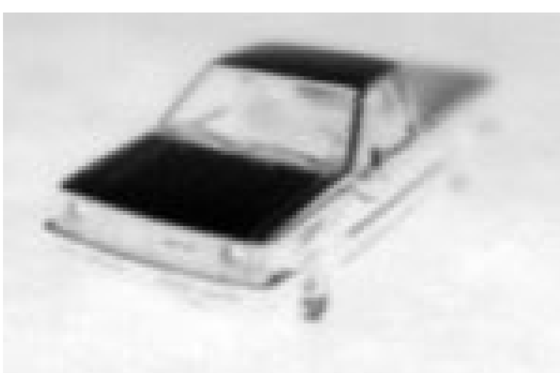

(e) y-polarized simulated image of a pickup truck.

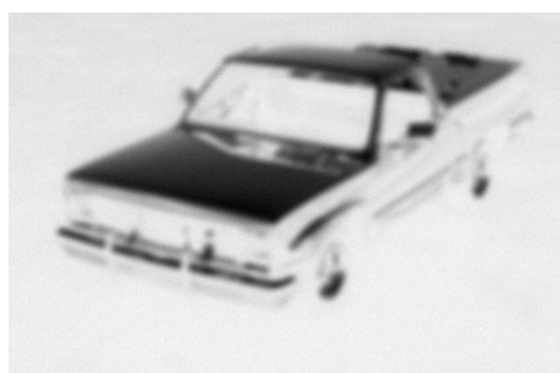

Table 2.3: Material properties used in the Bike Racks scene

Object	ε_r'	ε_r''	Temperature (K)	Notes
Posts	N/A	N/A	N/A	Metal
Chain	N/A	N/A	N/A	Metal
Bicycle Frame	N/A	N/A	N/A	Metal
Bricks	5.5	0.5	288	Concrete [19]
Windows	3.9	0	288	Fused silica [24]
Grass	4.9	2.1	288	Moist soil [21]
Tires	7.7	0.38	288	SA-9 tire [21]
Plastics	1.9	0.01	288	Polypropylene [25]

to produce an image that exhibits the same phenomenology as experimentally measured image, even for more complicated geometry.

2.3.4 Bike Racks

For the final scene, we consider a set of bike racks located behind Evans Hall at the University of Delaware. A visible image of the scene is shown in Figure 2.9a. Not visible in this photograph is a large tree directly behind the imager, nor the buildings surrounding this area. All are modeled, however, as they have significant impact on the simulated image. The bicycles in the simulated scene are based on publicly-available 3d models [22, 23]. A list of the material properties of objects in the scene is given in Table 2.3.

The experimental and simulated images for the x polarization are shown in Figures 2.9b and 2.9c respectively; the experimental and simulated images for the y polarization are shown in Figure 2.9d and 2.9e respectively.

All key features of the experimental data are reproduced in the simulation. The bicycle frame (or other metal parts) are the coldest objects in the scene, exactly as expected; the rear wheel of the near bicycle also features prominently, but the wheels of the far bicycle, being positioned to mostly reflect the horizon, are barely visible. The differences in relative power of the bicycle frame and front gear between the experimental and simulated image are due to slight differences in the model geometry and orientation. The bike lock, though faint in the experimental data, is also visible in both. The largest

Figure 2.9: Bicycles outside Evans Hall at visible wavelengths and 35 GHz.

(a) Visible image of bicycles.

(b) x-polarized image of bicycles.

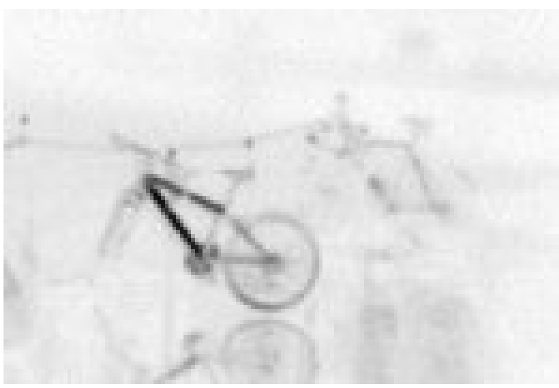

(c) x-polarized simulated image of bicycles.

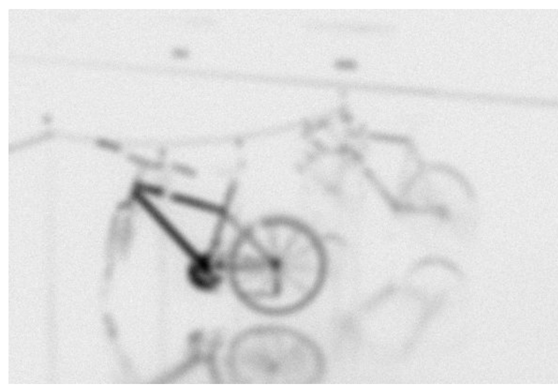

(d) y-polarized image of bicycles.

(e) y-polarized simulated image of bicycles.

difference between the x and y-polarized images is the presence of reflections from the bricks and this is faithfully reproduced in the simulation as well.

The conical cap on the fence posts and bike racks are major features, as are the chains between the fenceposts. The fenceposts themselves, reflecting the horizon, are significantly less visible. In the first iteration of the simulated image, while the fenceposts were invisible, their reflections in the bricks were very clear; this is because rays reflecting from the posts would be traveling at a low angle and leave the scene near the horizon, while rays reflected from the bricks to the fenceposts would leave the scene at an angle much closer to zenith, thus appearing cold; however, once the tree behind the imager was modeled, those rays could no longer exit the scene, and the reflected images of the posts disappeared.

Using the bicycle model, we have shown that the simulation software is capable of reproducing even complex scenes faithfully. We have also incidentally demonstrated the importance of modeling all objects in the scene, not just the ones that are in the imager field of view. Most importantly, we once again used experimentally derived values for the dielectric properties of the objects and reasonable values for the sky model, with no attempts at tweaking the values to more closely match the experiment; when combined with an accurate representation of the scene geometry, we demonstrated that the simulation software produces an image remarkably close to the experimental data, validating the simulation.

Chapter 3

NOVEL IMAGING SCENARIOS

In this chapter we apply our simulation software to novel mmW imaging scenarios. Three scenarios are chosen from military and civilian imaging applications for which millimeter waves are being considered. The goal of this chapter is not to exhaustively explore every scenario in detail, nor is it to design an imaging system for any scenario. The goal, rather, is primarily to showcase the value of the simulation software in determining whether a pmmW-based system is applicable to the given scenario.

Note that although we have not validated the simulated Stokes parameters, the x and y-polarized simulation values are derived from them; it is therefore reasonable to expect that the simulation of I, Q, U, and V will also be accurate, so in the following scenarios we report the Stokes parameters where they are useful.

3.1 Airplane Landing In Adverse Conditions

We first apply the ability of mmWs to penetrate fog to evaluate an airplane landing guidance system based on passive mmW imaging.

3.1.1 Scene Description

A small airplane makes its final landing approach at a 4° glide angle to a 20 m wide, 600 m long runway. The imager is placed on the nose of the aircraft. The imager targets are a series of passive mmW beacons, placed every 50 m alongside the runway, and every 5 m at the beginning and end. The beacons are 1 m square metal plates at a 45° angle, aligned such that they reflect the coldest part of the sky, at zenith, toward the airplane. Two possible beacon configurations are shown in Figure 3.1: the beacons can be, as previously described, a single 1 m square metal plate, shown in

Figure 3.1: Two styles of passive mmW landing guidance beacons.

(a) A single large metal plate. (b) Many small metal plates

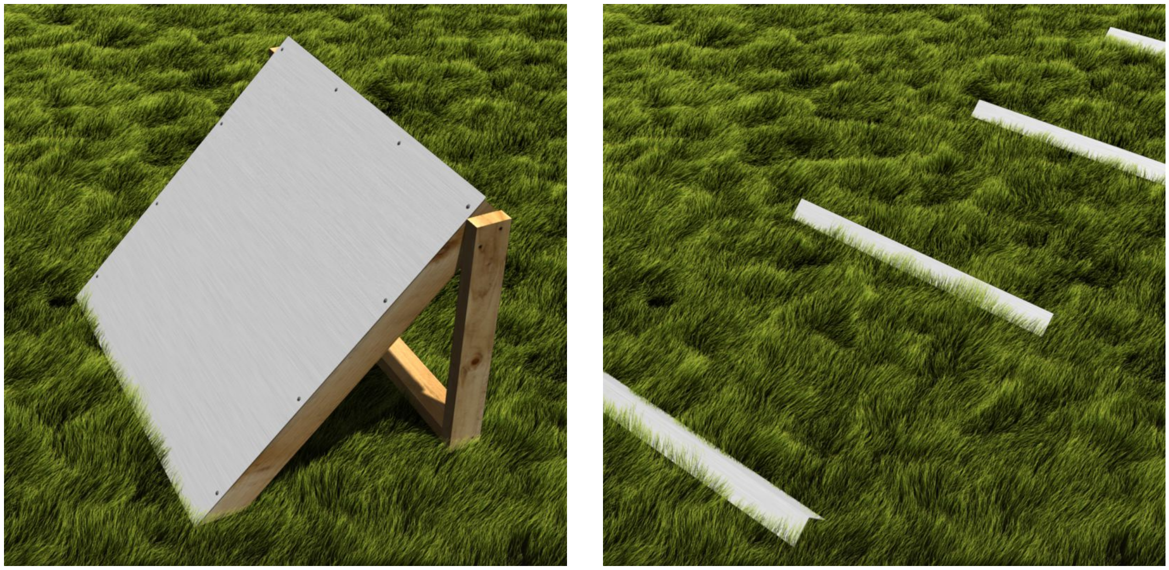

Figure 3.1a; alternatively, the metal plate could be broken up into a series of low-profile angle brackets, with each edge still angled at 45°, of a size and dimension such that the projected area is the same as the single plate, as shown in Figure 3.1b; a set of 10 brackets with a 10 cm side length placed with a 1 m gap between them would accomplish this. Either beacon is cheap and easy to deploy, completely non-reliant on an external power source, can be made flimsy enough to not damage an aircraft in the event of an emergency, and is trivial to camouflage such that it is invisible from the air except along the landing path.

The scene is simulated at both 35 and 95 GHz. The imager is a circular aperture with a diameter of 0.6 m for both frequencies, which produces a 500×500 pixel image, with a per-pixel noise of 4 K. The imager field of view is 10°. The material properties of all objects in the scene are given in Table 3.1. Three different weather conditions are simulated: cloudy, heavy fog, and extreme fog. Fog was generated using the model presented in Section 2.2.7, setting the cloud base height to 0 m (i.e. ground level), the cloud top to 600 m, and the columnar density of water in the clouds to $0.02\,\mathrm{g\,cm^{-2}}$ (corresponding to a volumetric density of $0.3\,\mathrm{g\,m^{-3}}$) for heavy fog or $0.06\,\mathrm{g\,cm^{-2}}$ ($1\,\mathrm{g\,m^{-3}}$)

Table 3.1: Material properties used in the Airplane Landing scenario.

	Dielectric Constant					
	35 GHz		95 GHz			
Object	ε_r'	ε_r''	ε_r'	ε_r''	Temperature (K)	Notes
Reflector	N/A	N/A	N/A	N/A	N/A	Metal
Runway	2.5	0.6	2.25	0.18	288	Asphalt [19]
Ground	4.9	2.1	3.7	1.2	288	Moist soil [21]

Table 3.2: Fog attenuation properties for the Airplane Landing scenario.

			Attenuation ($\mathrm{dB\,km^{-1}}$)	
Weather	Water Content ($\mathrm{g\,m^{-3}}$)	Visibility (m) [27]	35 GHz	95 GHz
Cloudy	0	N/A	0.17	0.92
Heavy Fog	0.3	50 - 150	0.40	2.29
Extreme Fog	1.0	25 - 70	0.88	5.05

for extreme fog. The attenuation characteristics of the model fog, along with the visible-wavelength visibility of such a fog, are given in Table 3.2. The calculated fog attenuation corresponds well with the attenuation of 0.6 to 1.5 $\mathrm{dB\,km^{-1}\,g^{-1}\,m^{3}}$ at 35 GHz and 3 to 5 $\mathrm{dB\,km^{-1}\,g^{-1}\,m^{3}}$ at 95 GHz [26].

Two distances to the runway are considered: 1000 m and 400 m. Both are considerably longer than visual range for the foggy weather conditions. All images are of the parameter $|E_y|^2$ because it was found to provide the highest contrast.

3.1.2 Landing In Cloudy Weather

In this scenario, there is no obscuring fog. This scenario serves as a basis of comparison for the remaining two conditions. The pmmW images in these conditions are shown in Figure 3.2.

There are several things to note regarding this imaging scenario. First, both frequencies allow recognition of the beacons at both ranges. This is important because it shows that, fundamentally, it is not impossible to land an aircraft based on data from a passive mmW imager. Second, the 35 GHz image is much lower quality. This is because at a 0.6 m aperture diameter, at a distance of 400 m, at 35 GHz, the spot size is approximately 14 m in diameter; given that the separation between beacons is only

Figure 3.2: Simulated mmW image of passive beacons in the absence of fog.

(a) 35 GHz image, 1000 m distance

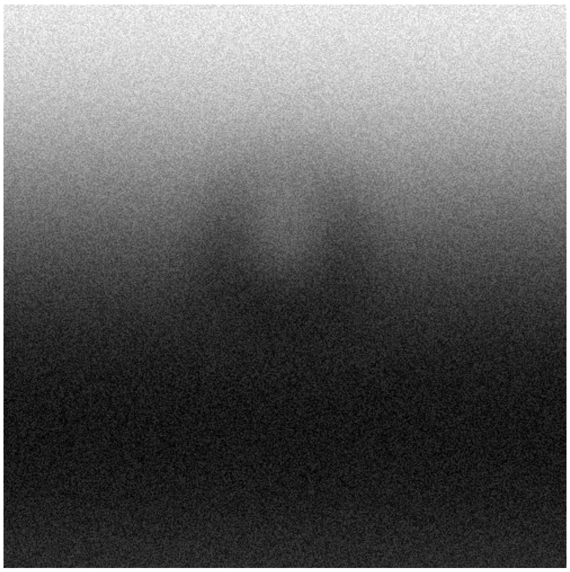

(b) 35 GHz image, 400 m distance

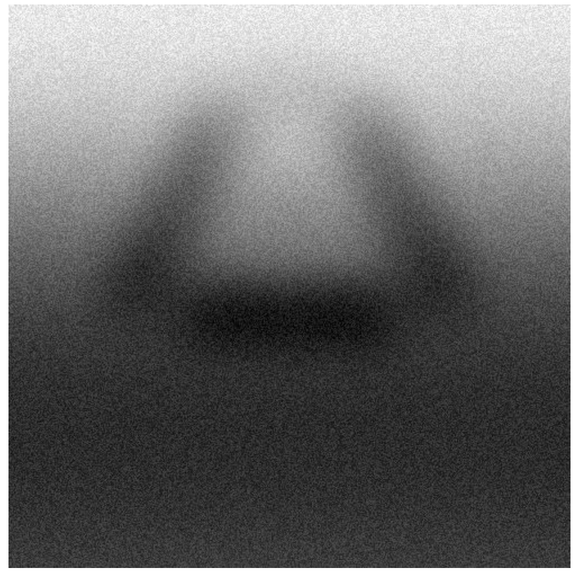

(c) 95 GHz image, 1000 m distance

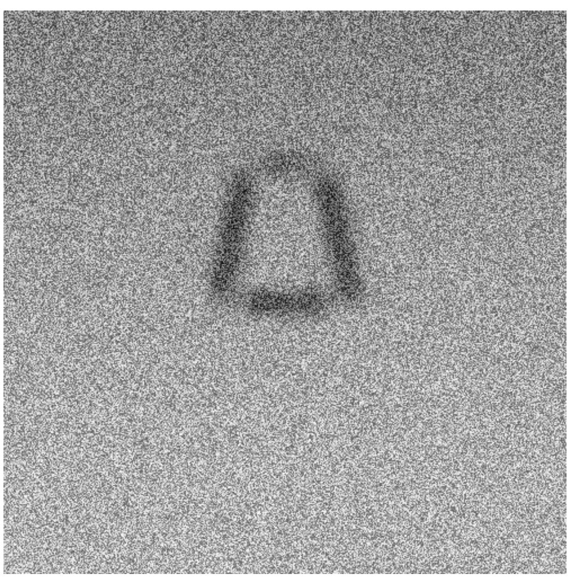

(d) 95 GHz image, 400 m distance

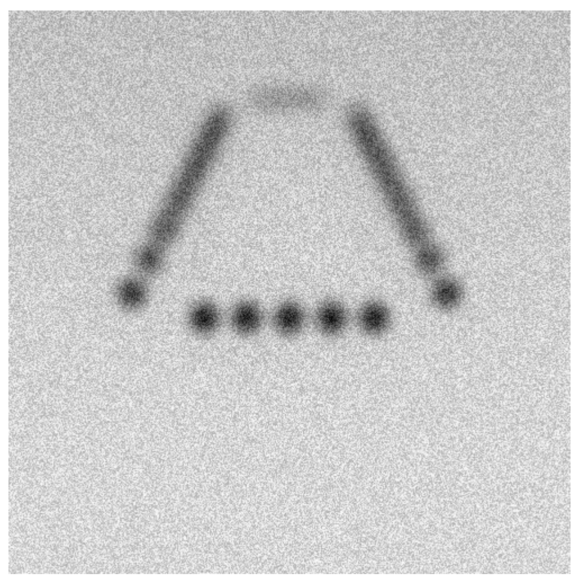

5 m, it is impossible to distinguish between individual beacons. All image pixels smear together to such an extent that it is only due to the extremely low temperature of the sky that we are able to see the beacons at all; the image is lighter at the top and darker at the bottom due to the slight difference in sky temperature between horizon and 9° above horizontal (the direction of specular reflection at the bottom of the image), illustrating the extreme loss of contrast. A larger aperture, such as could be mounted on a larger aircraft, would perform significantly better at 35 GHz. Similarly, at 95 GHz, the spot size at 1000 m is 13 m in diameter and the beacons blur together. Third, the runway itself is indistinguishable from the surrounding ground; this is because at such a shallow angle, both surfaces have nearly 100% reflectivity.

3.1.3 Landing In Heavy Fog

We now consider landing in a heavy fog. In this scenario, the runway is invisible from both distances; due to the nose of the aircraft, it possible that the pilot cannot see the ground at 1000 m from the runway, though it becomes visible before before the aircraft reaches the 400 m point. Any lights on the ground are most likely visible throughout the approach. The pmmW images under these conditions are shown in Figure 3.3.

Again, at both frequencies the landing beacons are visible, and, again, the 35 GHz image is too low-contrast to be usable at 1000 m. It is interesting to note that the images at are not significantly different from those taken in cloudy weather; this is because the fog does not significantly affect the zenith temperature. At 95 GHz, the total additional path loss from the sky to the detector via the beacon due to fog is only 2.2 dB (0.8 dB traveling vertically through the 600 m of fog, the remainder traveling the 1000 m to the detector). The fog has even less effect at 35 GHz, but the image is too poor due to the aperture size for this to matter.

Figure 3.3: Simulated mmW image of passive beacons through $0.3\,\mathrm{g\,m^{-3}}$ water content fog.

(a) 35 GHz image, 1000 m distance

(b) 35 GHz image, 400 m distance

(c) 95 GHz image, 1000 m distance

(d) 95 GHz image, 400 m distance

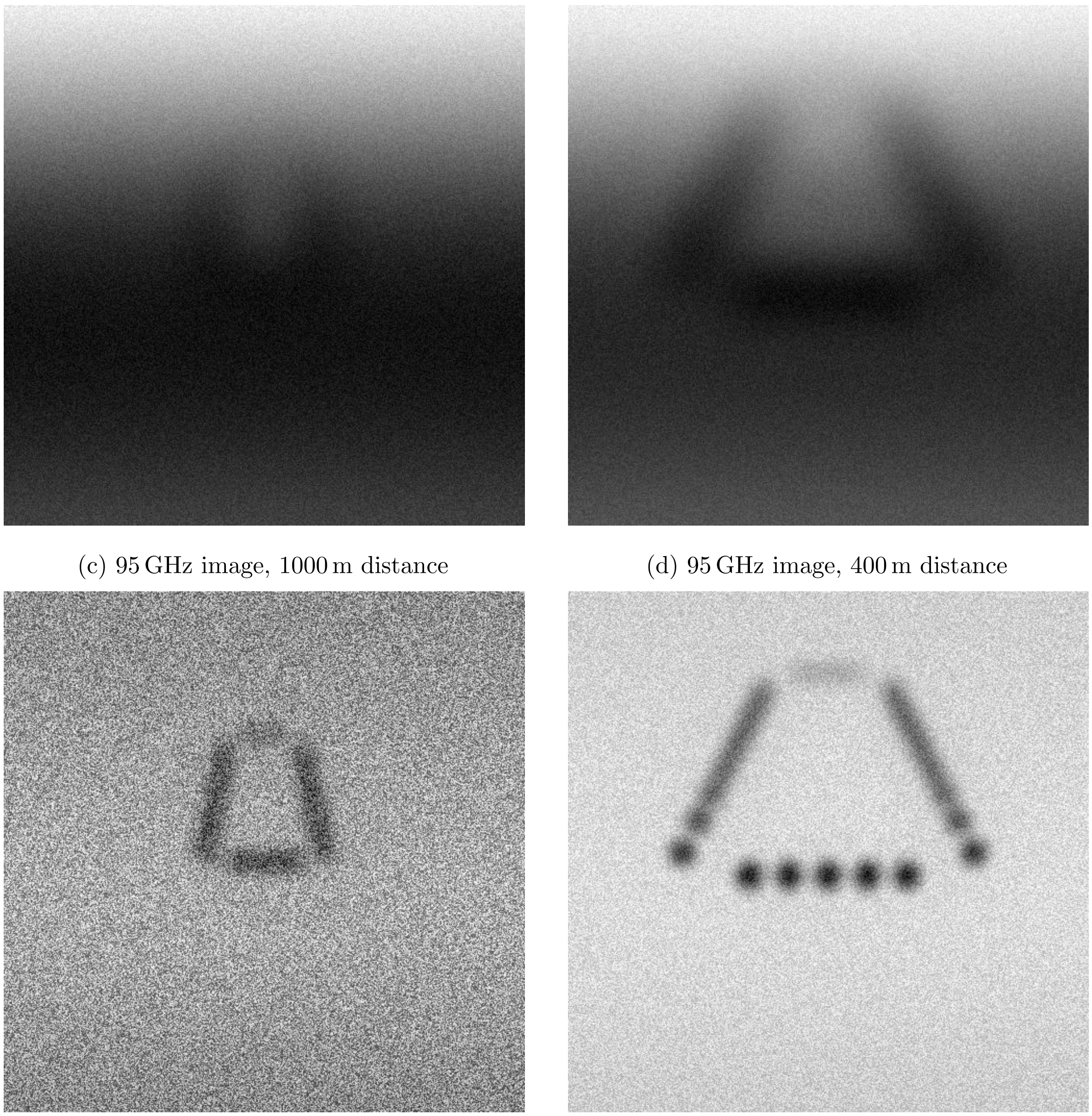

3.1.4 Landing In Extreme Fog

We now consider landing in extremely heavy fog. In this scenario, the runway is invisible from both distances, and remains invisible until immediately before touchdown; it is possible, for some larger aircraft, for the pilot to never see the ground at all until the front landing gear contacts the runway. Landing under such conditions is currently possible only using ground-based radio transmitters to guide the aircraft. The pmmW images under these conditions are shown in Figure 3.4.

The value of mmW imaging is illustrated most strongly in this scenario. The 35 GHz image is again not degraded significantly compared to the cloudy weather version but, again, the image was very low quality to begin with. The image at 95 GHz is degraded by the fog, but the runway markers are still visible even at a 1000 m range. This is notable because in this heavy a fog, absolutely nothing is visible from the cockpit in any other imaging regime; light from the ground would be attenuated and scattered by the intervening fog, and no structure tall enough to be seen through it would be built this close to a runway. The pilot would have radar altimetry and GPS guidance, but no way to absolutely orient himself in the absence of active transmissions from the ground. The pmmW beacons in conjunction with a passive imaging system can be used for this purpose, even in zero-visibility conditions.

3.1.5 Conclusion

A set of mmW beacons placed alongside a runway can aid in landing in extreme weather conditions where it would otherwise be impossible. The beacons themselves are cheap, safe, low-power, covert, and frequency-agnostic. The most stringent requirement on the imaging system is the aperture size: the system must be able to resolve individual beacons, otherwise (as in the 35 GHz images) the contrast is degraded too far to be reliably useful. Lower frequencies provide improved propagation characteristics, but require a larger aperture. More study, including specific details about the proposed imager performance, is required to make a final determination of the feasibility of such a system, though we have proven that the concept is sound.

Figure 3.4: Simulated mmW image of passive beacons through $1.0\,\mathrm{g\,m^{-3}}$ water content fog.

(a) 35 GHz image, 1000 m distance

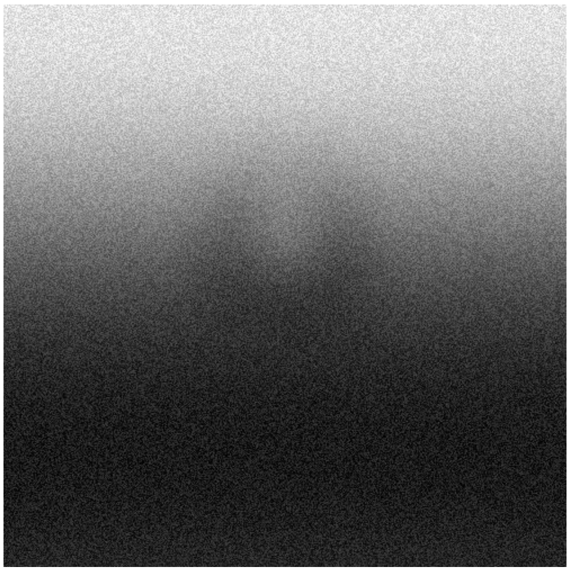

(b) 35 GHz image, 400 m distance

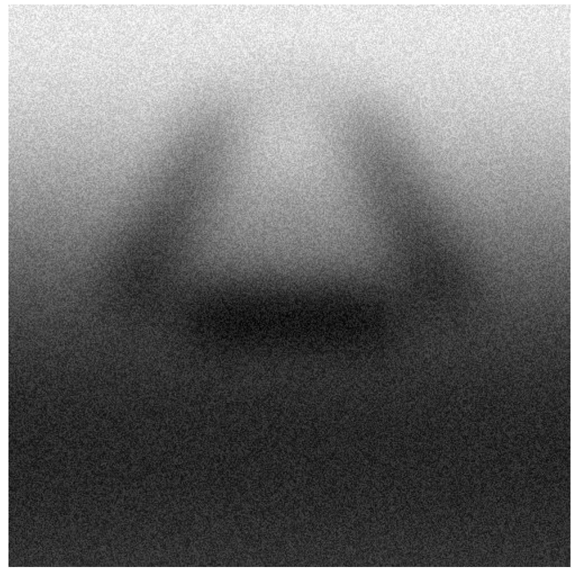

(c) 95 GHz image, 1000 m distance

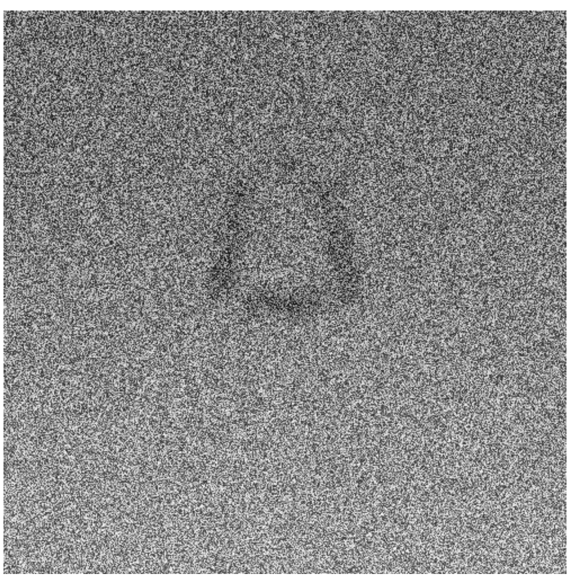

(d) 95 GHz image, 400 m distance

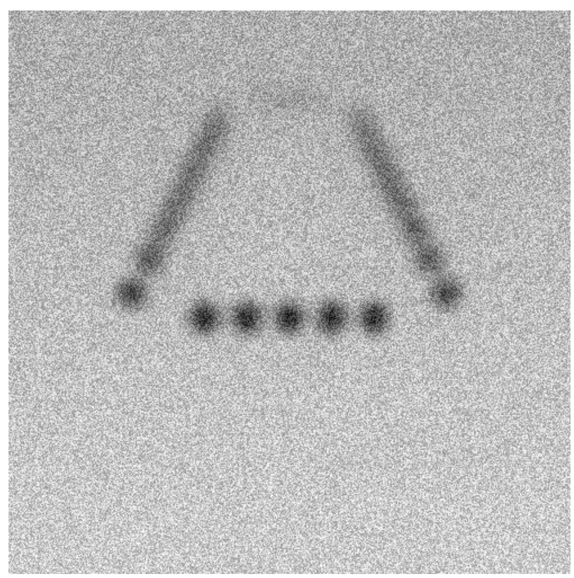

Figure 3.5: Visible image of the underarm holster used in the mmW simulation.

3.2 Concealed Weapon Detection

We apply the ability of mmWs to penetrate clothing to evaluate the capabilities of a concealed weapon detection system based on passive mmW imaging.

3.2.1 Scene Description

A man dressed in street clothing carries a handgun in an underarm holster of the kind shown in Figure 3.5; this holster is easily concealed under street clothing; the torso and human model are based on a publicly-available 3d model [28]. We have not developed a hair model, so the man is taken to be bald.

Weight, and thus aperture size, is less of an issue for a ground-based system, so we take the imager as having a circular aperture with a diameter of 1.0 m. The imager is placed at a height of 1.5 m above the ground. Two distances to the target are considered: 4 and 20 m, corresponding to checkpoint and standoff imaging scenarios; at 4 m the field of view is 30° and at 20 m the FOV is 6°. Two locations for the target are

Table 3.3: Material properties used in the Concealed Weapon Detection scenario.

	Dielectric Constant					
	35 GHz		95 GHz			
Object	ε'_r	ε''_r	ε''	ε''_r	Temperature (K)	Notes
Shoes	2.2	0.06	2.2[1]	0.16[1]	300	Leather [13]
Holster	2.2	0.06	2.2[1]	0.16[1]	310	Leather [13]
Gun	N/A	N/A	N/A	N/A	N/A	Metal
Clothing	1.6	0.06	1.6[1]	0.12[1]	300	Denim [13]
Person	14	16	5.9	9.4	310	Dry skin [29, 30]
Ground	2.5	0.6	2.25	0.18	296	Asphalt [19]

considered: outdoors and indoors; outdoors, reflections from the cold sky at various angles are expected to provide the largest contrast and aid in detection, while indoors the contrast is expected to result from temperature differences between the person and his surroundings.

The scene is simulated at both 35 and 95 GHz. We consider all polarization states: the Stokes parameters I, Q, U, and V, as well as $|E_x|^2$ and $|E_y|^2$. The imager produces a 740×440 pixel image with a per-pixel noise of 4 K for each polarization state. The material properties of all objects in the scene are given in Table 3.3.

We have chosen denim for the clothing as it is the thickest and most lossy material that is commonly worn. The denim is assumed to be 0.8 mm thick and the leather holster is 2 mm.

It should be noted that we can only present still images here; seeing the subject in motion (e.g. turning around slowly) would significantly improve detection probability.

3.2.2 Outdoors

The simulated outdoor images, 35 GHz from a distance of 4 m, 95 GHz from 4 m, and 95 GHz from 20 m are shown in Figures 3.6, 3.7, and 3.8, respectively. The 35 GHz image from 20 m is almost too blurry to resolve the person, much less detect any concealed weapons, so it is not included.

[1] Dielectric constant values were not found in literature at 95 GHz; the values were extrapolated based on low-frequency data.

Figure 3.6: Concealed weapons detection at 35 GHz, outdoors at 4 m.

(a) Stokes I

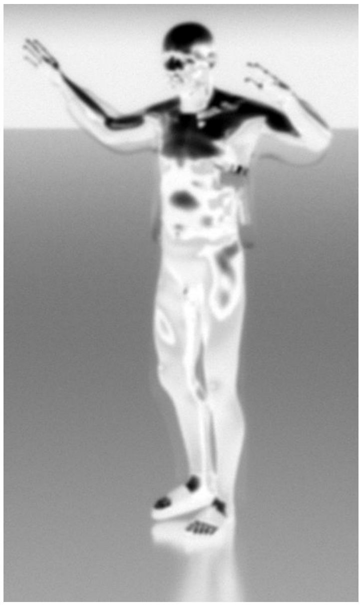

(b) Stokes Q

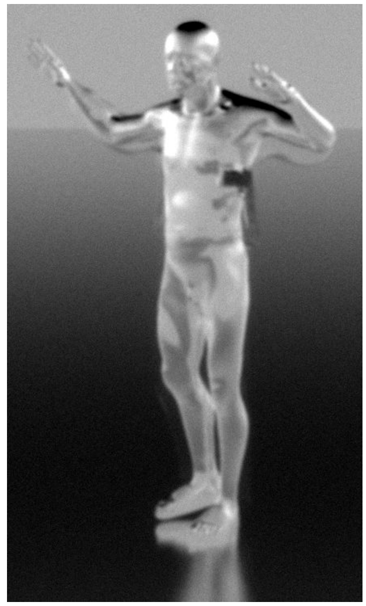

(c) Stokes U

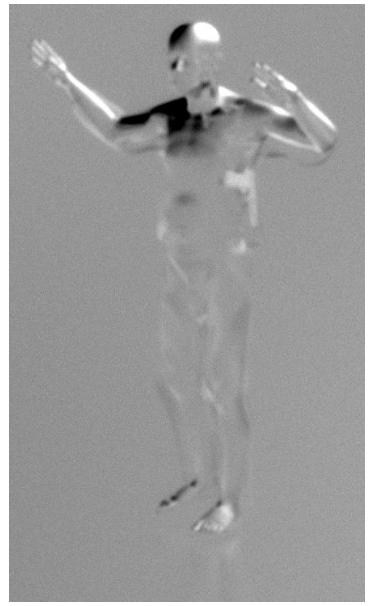

(d) Stokes V

(e) $|E_x|^2$

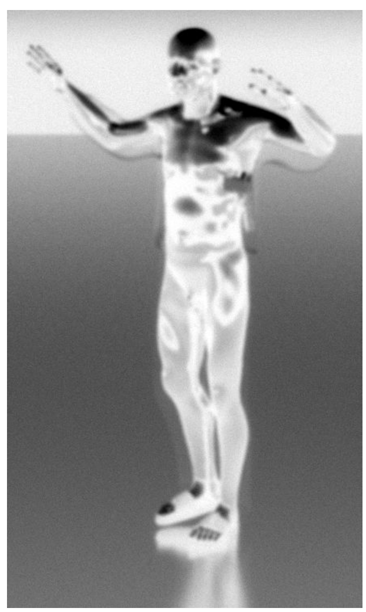

(f) $|E_y|^2$

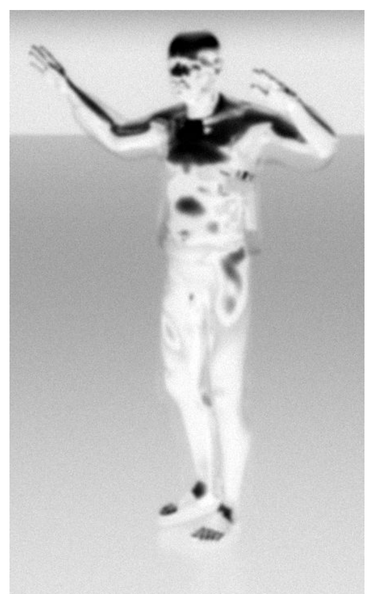

Figure 3.7: Concealed weapons detection at 95 GHz, outdoors at 4 m.

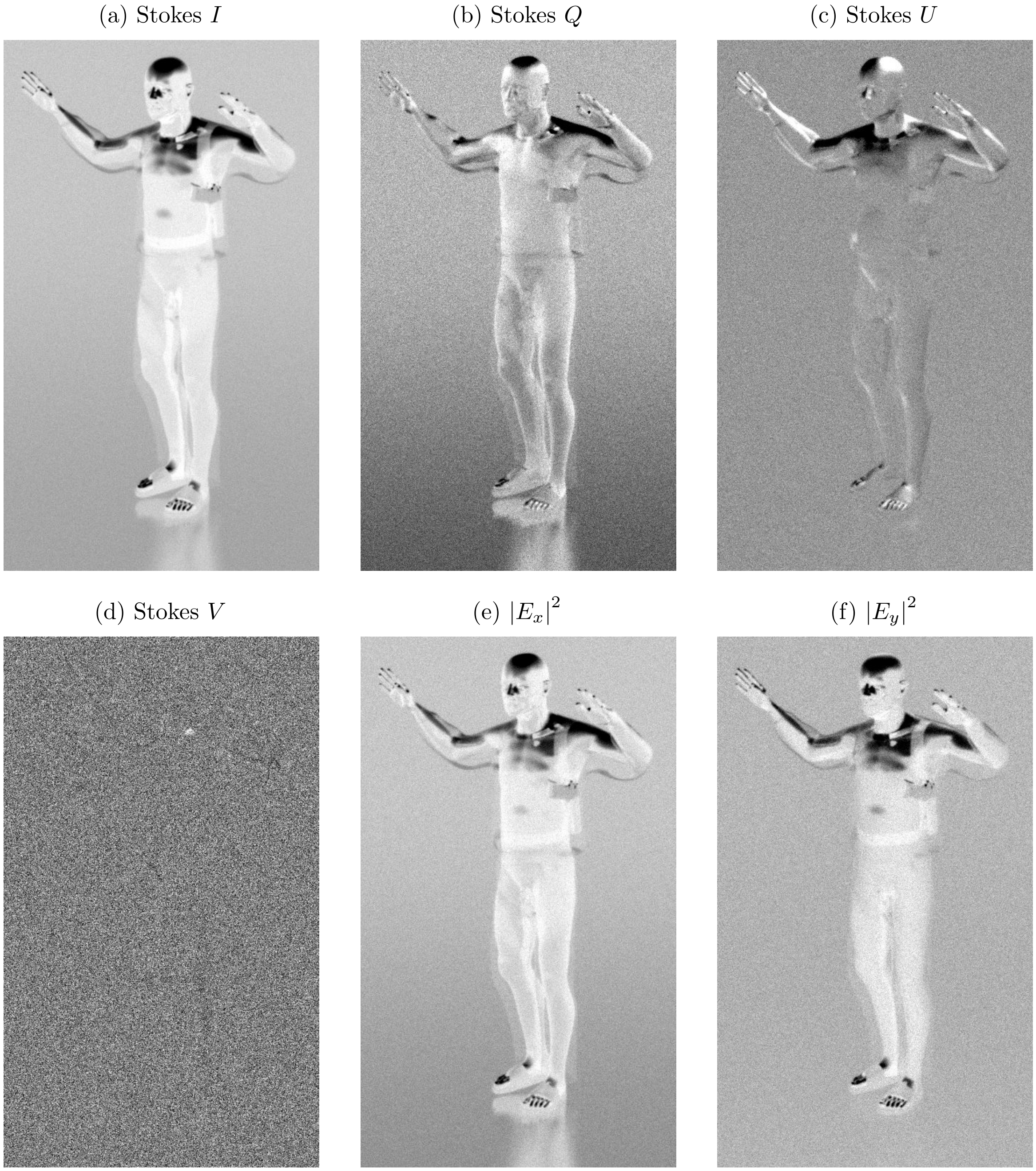

(a) Stokes I (b) Stokes Q (c) Stokes U

(d) Stokes V (e) $|E_x|^2$ (f) $|E_y|^2$

Figure 3.8: Concealed weapons detection at 95 GHz, outdoors at 20 m.

(a) Stokes I

(b) Stokes Q

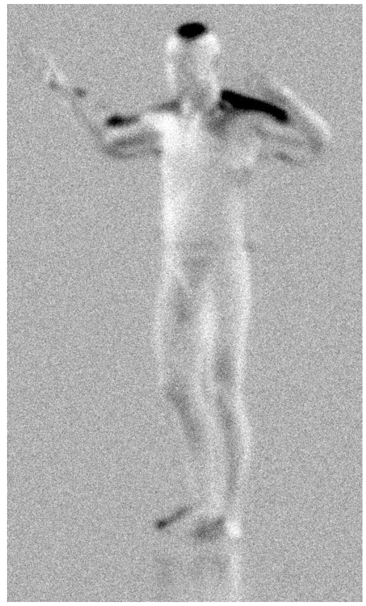

(c) Stokes U

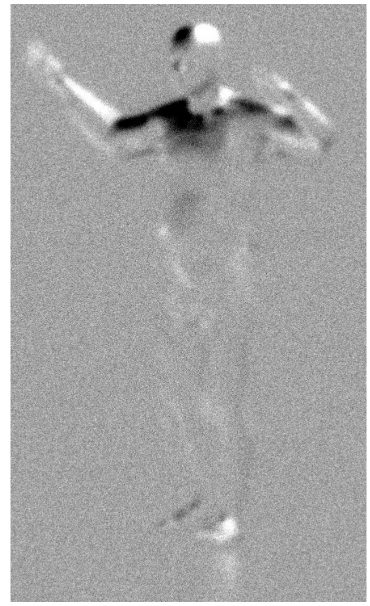

(d) Stokes V

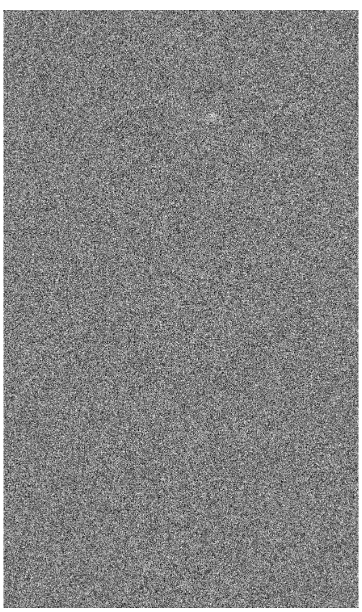

(e) $|E_x|^2$

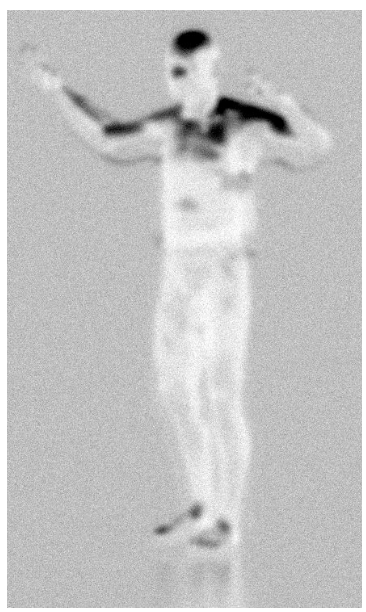

(f) $|E_y|^2$

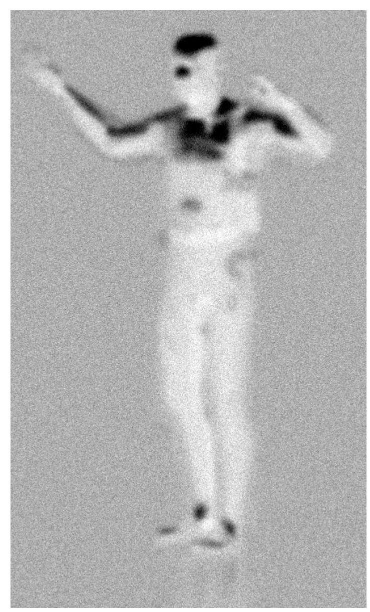

We notice several things about these images. First, the V Stokes parameter (degree of left/right circular polarization, Figures 3.6d, 3.7d, and 3.8d) images conveys no useful information; there is simply not enough circular polarized radiation in this scenario to be worth detecting. Second, the darkest pixels are consistently the top of the head, the shoulders, and parts of the upper chest; this is unsurprising, as these parts are angled to reflect the coldest part of the sky at zenith. Since the images are displayed by setting the coldest pixel to black, the hottest to white, and linearly interpolating the other values[2], these cold patches lead to the rest of the scene being washed out. Finally, the handgun is visible in every frequency and distance; it is not always obvious as a threat, but it is always visible as a foreign object in at least one of the polarizations.

We now analyze each frequency-distance pairing individually.

Figure 3.6 shows the images produced at 35 GHz from a distance of 4 m. One immediately notices that the handgun has an exceptionally strong signature in the Q and U (Figures 3.6b and 3.6c, respectively) images, with even the trigger guard being visible. This is unfortunately a happy coincidence of a particular arrangement of sky temperature, viewing angle, and contraband position, and is not the case in general, as illustrated by the higher-frequency images. We also see this in Figure 3.9, which shows the Q image from a series of different angles, with the visibility of the handgun varying depending on viewing angle, demonstrating that multiple viewing angles will be needed to reliably detect hidden contraband. One observation that does apply in general, however, is that the lumpiness of the body combines with the high variation in the sky temperature profile to produce several artifacts near folds of skin, especially around the abs, thighs, and knees in the I, $|E_x|^2$, and $|E_y|^2$ images; however, these

---

[2] As part of the display process, the real-valued image data is converted to an 8-bit integer between 0 (black) and $2^8 - 1 = 255$ (white); it was found that setting the coldest pixel to black would result in the lowest 40 or 50 integers each being assigned to a single digit number of pixels, with similar behavior for white pixels. This caused the 8-bit image to effectively use only 7 bits, significantly decreasing the contrast. The black (white) level is actually set such that the coldest (hottest) $1/256^{\text{th}}$ of the pixels are black (white), and the rest of the values are linearly interpolated.

contributions affect all polarizations almost equally, so they nearly cancel out in the Q and U states. Finally, the clothing is invisible except where it bags under the arms, and the holster is entirely invisible.

Switching to the same view at 95 GHz, shown in Figure 3.7, reveals several finer details (such as toes; note that the person is wearing sandals) due to shorter wavelength. The clothing is visible as shadows around the legs and torso, though it does not significantly affect the image; the holster is now visible as well, and it obscures the barrel of the handgun; the hand-grip is still clearly visible, however. There is less variation in sky temperature, so the aforementioned artifacts in Figure 3.6 are much weaker. Also, the handgun no longer shows up particularly strongly in the Q and U images (Figures 3.7b and 3.7c, respectively), though it does remain visible.

Finally, consider the 95 GHz image from a distance of 20 m shown in Figure 3.8. The handgun is no longer recognizable as a handgun, though it and the holster are visible as foreign objects. It has, however, disappeared from the Q and U images; in fact, in the Q image it is more noticeable from the way it disrupts the bright line running up the edge of the torso. This disruption of the generally smooth shape of the human body suggests a characteristic of concealed objects that the operator could be trained to look for.

3.2.3 Indoors

The simulated indoor images, 35 GHz from 4 m, 95 GHz from 4 m, and 95 GHz from 20 m are shown in Figures 3.10, 3.11, and 3.12, respectively. Again, the 35 GHz image at 20 m is too blurry to be usable.

Save for the level of blur and some minor differences in the visibility of clothing items, the images are effectively identical, so we discuss them together.

The images have a considerably higher apparent noise than the outdoor images; this is due to the much lower contrast in the scene: the surroundings are uniformly 296 K, and the person is 310 K, leading to a maximum temperature difference of 14 K; the 4 K noise figure is a significant fraction of that range. In most mmW imaging

Figure 3.9: Series of outdoor images at 35 GHz taken from a distance of 4 m. All images are of the Q parameter.

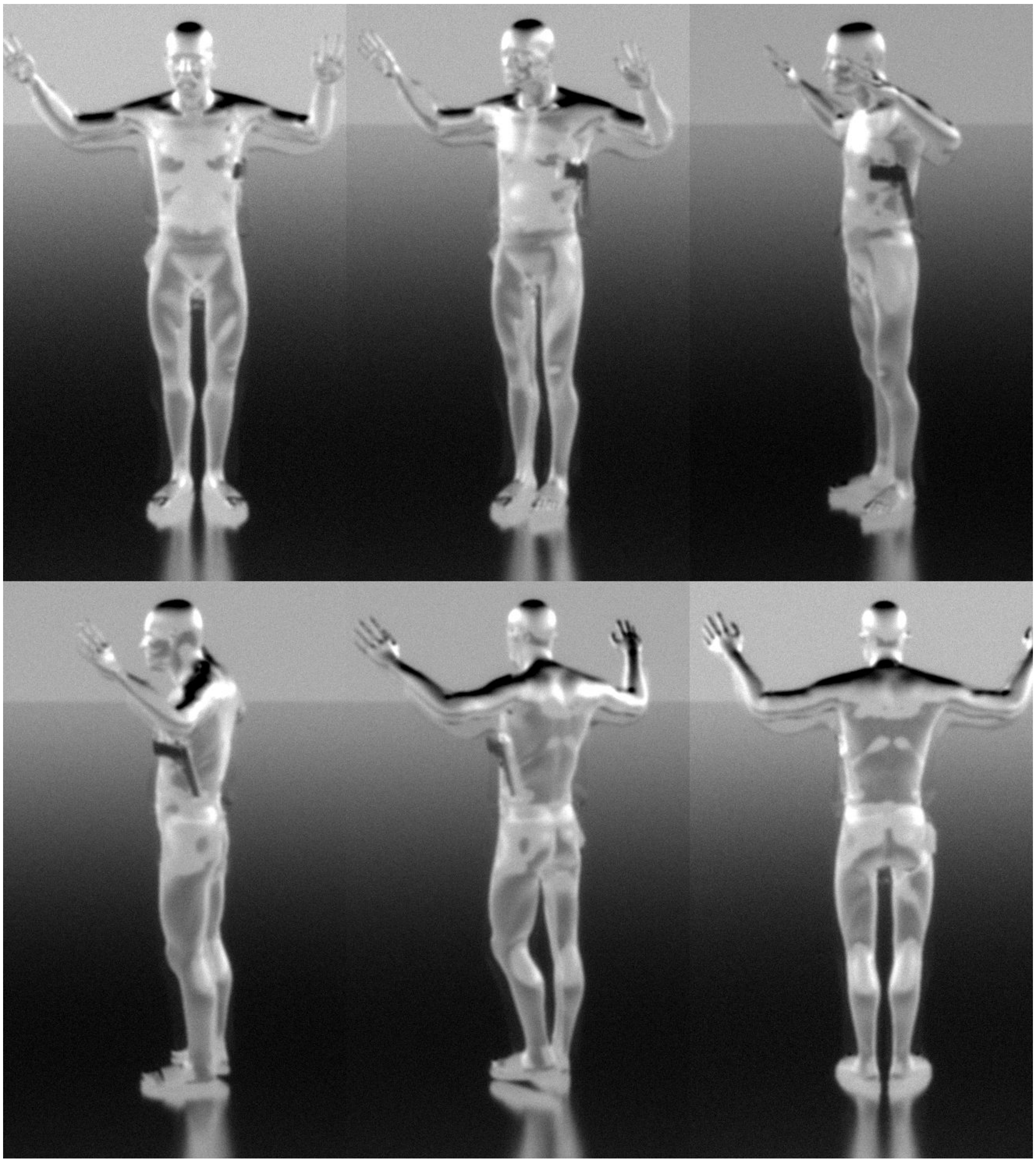

Figure 3.10: Concealed weapons detection at 35 GHz, indoors at 4 m.

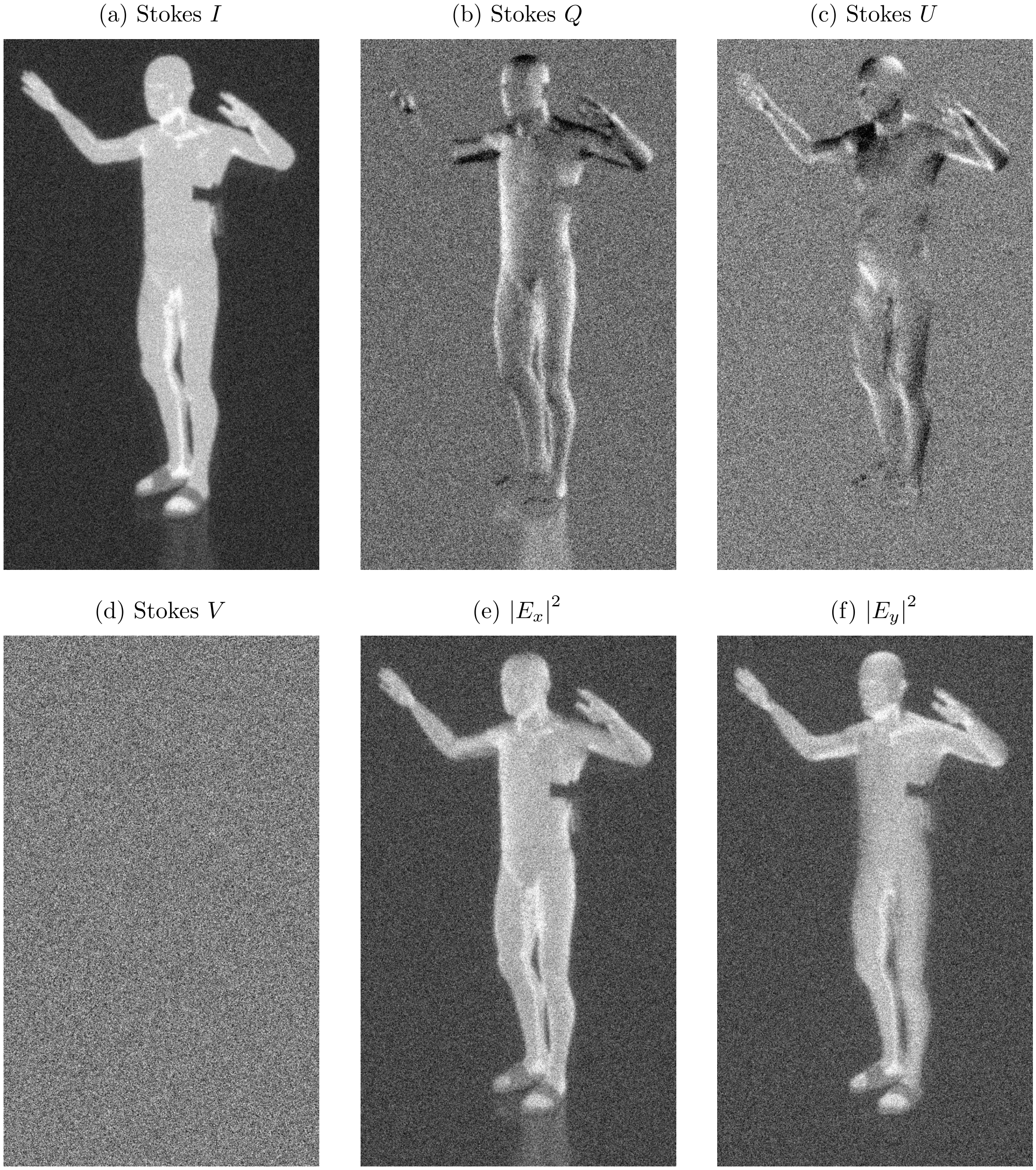

Figure 3.11: Concealed weapons detection at 95 GHz, indoors at 4 m.

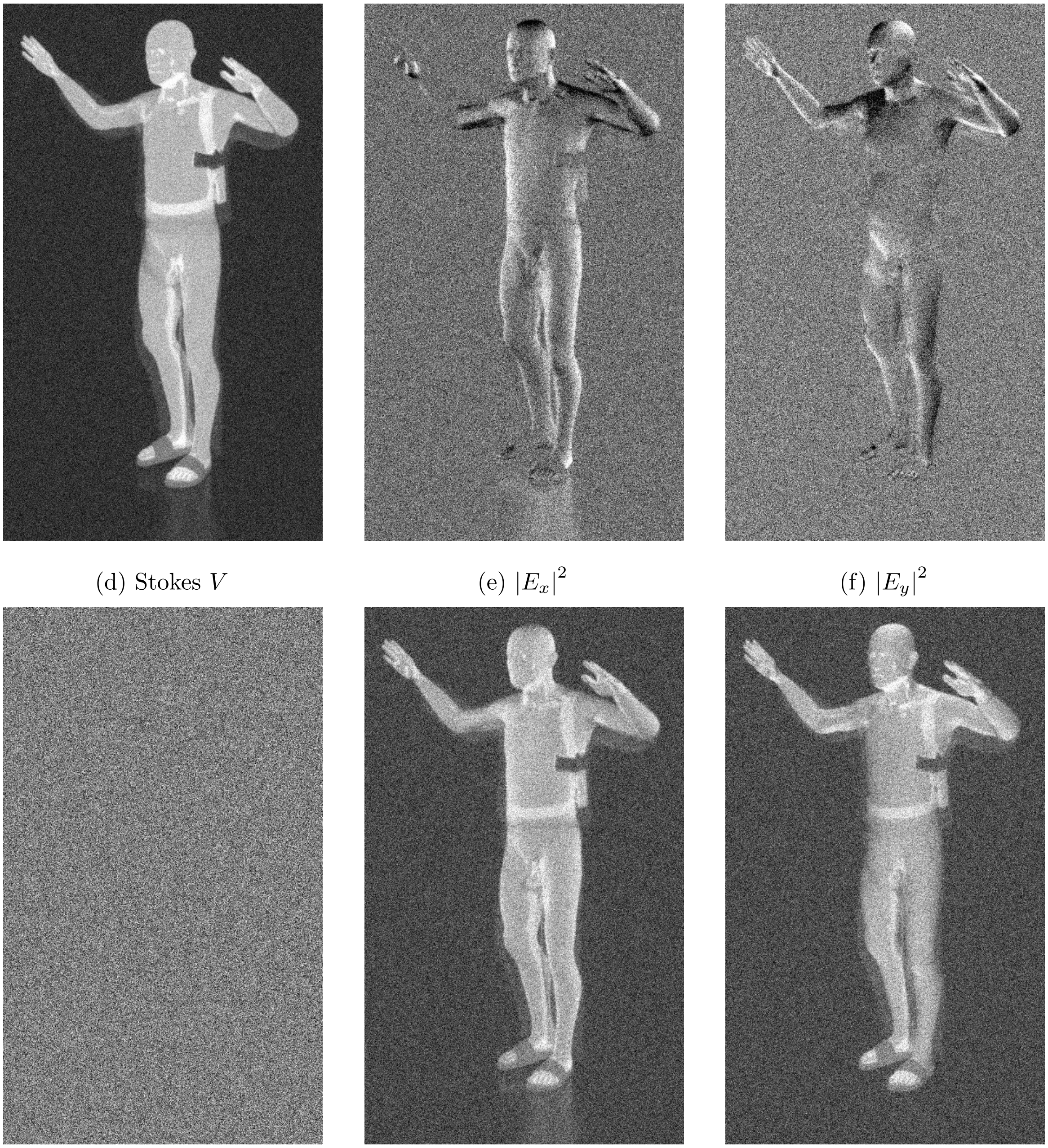

(a) Stokes I (b) Stokes Q (c) Stokes U

(d) Stokes V (e) $|E_x|^2$ (f) $|E_y|^2$

Figure 3.12: Concealed weapons detection at 95 GHz, indoors at 20 m.

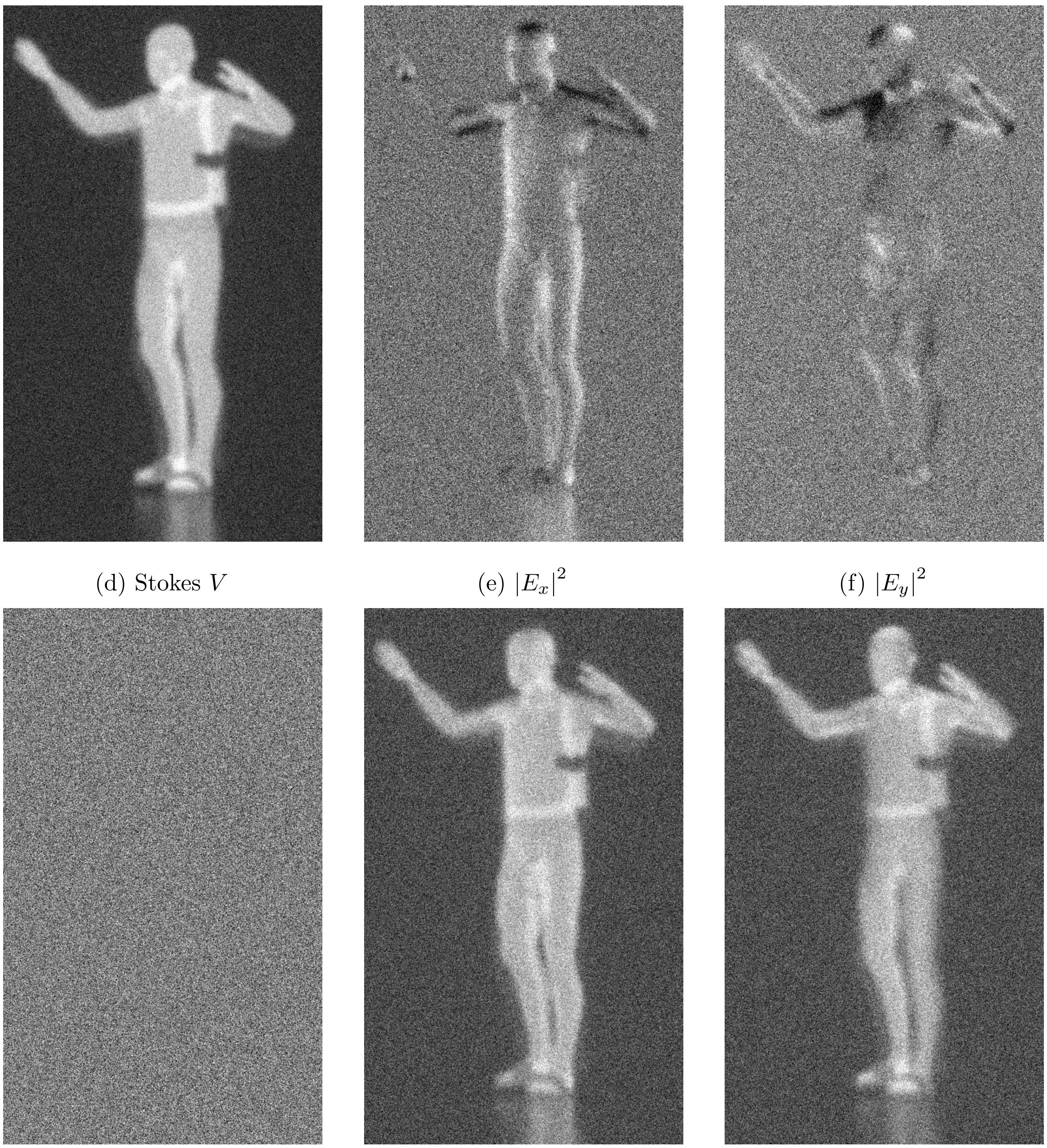

(a) Stokes I

(b) Stokes Q

(c) Stokes U

(d) Stokes V

(e) $|E_x|^2$

(f) $|E_y|^2$

scenarios, contrast is due to differences in reflected temperature between objects; here, however, the reflected temperature is uniform, so the imager has effectively become a low-quality clothing-penetrating thermal camera.

Again we see a bright line up the edge of horizontal surfaces in the Q images (Figures 3.10b, 3.11b, and 3.12b), with the handgun disrupting it; the value of this observation is dubious in this case, as the handgun is plainly visible in the I, $|E_x|^2$, and $|E_y|^2$ images. We also again see the value of considering multiple polarization images: visual artifacts, such as increased brightness in cavity areas (e.g. under the chin and around the groin), either disappear or are diminished in some images, while anomalous objects (the handgun in this scenario) remain visible in some form in every image.

3.2.4 Conclusion

A passive mmW imaging system can be used to see through clothing and aid in the detection of concealed weapons from a distance. Whether such a system is effective depends on the location, the viewing angle, and the sort of contraband that one hopes to detect.

Humans are essentially bags of salt water, and water has a relatively high dielectric constant in the microwave and mmW regime, which leads to a relatively high reflectivity for human skin. Dielectric materials concealed under clothing would have lower reflectivity, but be at the same temperature as the body, and so show up warm; highly reflective materials, such as metals, would reflect the colder surroundings, and show up as cold. This occurs both indoors and outdoors, though outdoors the reflections from the head, shoulders, and chest provide a much colder return than from a vertically-oriented reflector strapped to the torso, and a strategy must be devised to deal with this. Besides the aperture size/resolution design, there is the non-obvious tradeoff between 35 and 95 GHz that, while mmWs at 95 GHz have improved detection capabilities (evidenced by the holster becoming visible), they also have a decreased ability to penetrate clothing.

We note that we performed imaging in the atmospheric windows of 35 and 95 GHz; this led to degraded performance outdoors due to the cold sky. However, if we were to perform the imaging in one of the mmW absorption bands, such as near 60 GHz, the sky temperature would be considerably higher, while at reasonable detection ranges the propagation loss to the imager would still be relatively low. This would lead effectively to indoor-like imaging in all weather conditions; whether this is preferable depends on the capabilities of the imager.

Most importantly, though, the simulation software has enabled us to reach these conclusions without needing to perform expensive and time-consuming experiments.

3.3 Search and Rescue

We apply the ability of millimeter waves to image through clouds to evaluate using passive mmW imaging to aid in the search portion of search-and-rescue operations.

3.3.1 Scene Description

A Cessna 172 (a small metal-skinned airplane) has crashed in a desert scrub land environment; a visible image of the crash is shown in Figure 3.13a; the airplane model in this and the simulated mmW images is based on a publicly-available 3d model [31]. A passive mmW search system is mounted on the underside of a search aircraft flying at 3000 m, pointed down; the imager has a field of view of 10°, corresponding to a 500 m wide search area, per flyover. The imager has a diameter of 2 m, which would be difficult to achieve with a full aperture, but a 2 m equivalent synthetic aperture system could be produced with antennas distributed over all horizontal surfaces of the search craft.

The scene is simulated at 35 and 95 GHz, which corresponds to a spot size on the ground of 13 and 5 m, respectively. The imager produces a 300×300 pixel image, with a 4 K per-pixel noise at each frequency. The material properties of all objects in the scene are given in Table 3.4.

Figure 3.13: Visible images of the targets in the Search and Rescue scenario.

(a) A crashed Cessna 172

(b) A pmmW beacon made from a metalized Mylar emergency blanket

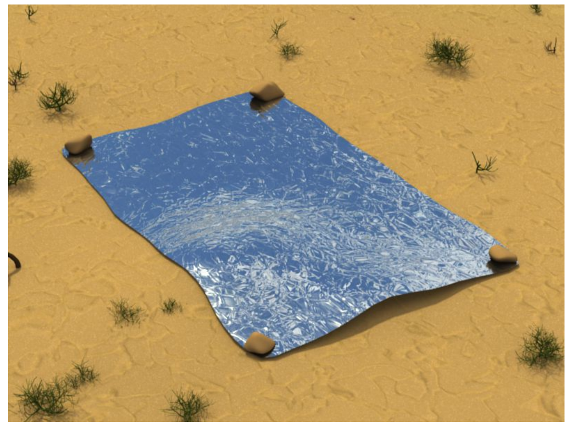

Table 3.4: Material properties used in the Search and Rescue scenario.

	Dielectric Constant					
	35 GHz		95 GHz			
Object	ε_r'	ε_r''	ε_r'	ε_r''	Temperature (K)	Notes
Dry Ground	3.1	0.2	2.9	0.2	300	Dry soil [21]
Wet Ground	4.9	2.1	3.1	1.2	300	Moist soil [21]
Rocks	6.7	0.31	6.7	0.43	300	Basalt [32]
Aircraft	N/A	N/A	N/A	N/A	N/A	Metal
Blanket	N/A	N/A	N/A	N/A	N/A	Metal

We consider three variants of this scenario. In the first, basic scenario, we attempt to find the plane. In the second scenario, the pilot attempts to signal the search plane, using a Mylar emergency blanket (shown in Figure 3.13b); the blanket is metal-coated, so it would be 100% reflective; it is 1.5 m wide and 2 m long. In the last scenario, the pilot has a pack of 12 emergency blankets and uses them to make a large beacon measuring 6 m by 6 m. We also consider three weather conditions: clear, cloudy, and moderate rain. The latter two weather conditions would disrupt search-and-rescue efforts by high-altitude aircraft operating at visible or IR wavelengths. Note that this scenario could also take place at any time, as time of day is not a significant factor in the mmW temperature of the atmosphere, which is another significant advantage over a visible or IR system in this scenario.

We model small-scale ground clutter such as rocks, boulders, shrubs, and trees; we do not model large-scale clutter objects such as streams or other major terrain features which would break up the uniform terrain and make detection more difficult; however, there are very few large, flat, horizontal, metallic objects in nature, so the airplane and beacons will still always be the coldest objects in the scene. Many small aircraft are partially or entirely fabric-skinned, however, with a metal (or composite material, for newer craft) skeleton, which would be far less visible; we attempt to address this problem by removing the airplane from the scene when beacons are present; we do not attempt to simulate a fabric-skinned composite material-framed aircraft without beacons. Finally, we do not model phase noise or scattering in the atmosphere, which can be significant over long distances [33]; our only sources of image degradation are aperture size effects, propagation loss due to attenuation, and a per-pixel imager noise.

3.3.2 Clear Weather

In this scenario, the weather is clear; as the best-case imaging scenario, this serves as a baseline for comparison for the other weather conditions. The pmmW image is shown in Figure 3.14. The path loss from the aircraft to the ground is 0.1 dB at 35 GHz and 0.3 dB at 95 GHz.

Figure 3.14: Simulated mmW search and rescue from an altitude of 3000 m in clear weather.

(a) Airplane at 35 GHz

(b) Small beacon at 35 GHz

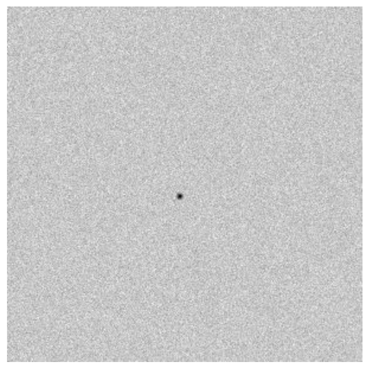

(c) Large beacon at 35 GHz

(d) Airplane at 95 GHz

(e) Small beacon at 95 GHz

(f) Large beacon at 95 GHz

We notice several things in these images. First, the airplane and beacons are clearly visible at both frequencies; not only are they visible, they are each easily the brightest object in the scene. Second, all ground clutter features have disappeared, having been blurred out and lost in the imager noise; additionally, the slight bumpiness and variation in terrain height has also been washed out. This is useful because it renders the background essentially free of small clutter. Third, the signal is not obviously a downed aircraft at 35 GHz, nor is it distinguishable from the beacons; at 95 GHz., however, the shape of the airplane is clear. Fourth, the small beacon is a much weaker signal than the aircraft, but still visible under these conditions; this means that pilots of fabric-skinned aircraft could reasonably use an emergency blanket as a pmmW signal. Finally, the lower resolution of the 35 GHz system is most obvious when considering the small beacon, which is far smaller than the smallest resolvable feature at this distance; it is cold enough to remain visible, but the noise level is much higher.

3.3.3 Cloudy Weather

In this scenario, the weather is cloudy. The clouds are considered as having an altitude between 1000 and 2000 m (recall the aircraft is at 3000 m); this degrades the imaging in two ways: first, the search craft must see through the clouds, and second, the signal from the ground is weaker due to the increased sky temperature caused by the clouds. The pmmW image is shown in Figure 3.15. The path loss from the aircraft to the ground is 1.2 dB at 35 GHz and 5.6 dB at 95 GHz.

The first thing to notice is that, when compared to the image in clear weather, the 35 GHz image is barely degraded. The images are somewhat noisier (indicated by the background becoming grayer), but the airplane, small beacon, and large beacon each remain easily visible through the clouds. Again, though, it is only possible to detect the crashed airplane, and not to determine its shape. Regarding the 95 GHz images, the airplane and large beacon remain visible. The small beacon is reduced to a few pixels and is very nearly lost in the noise; however, it would show up clearly as the

Figure 3.15: Simulated mmW search and rescue from an altitude of 3000 m through a 1000 m thick cloud layer.

(a) Airplane at 35 GHz

(b) Small beacon at 35 GHz

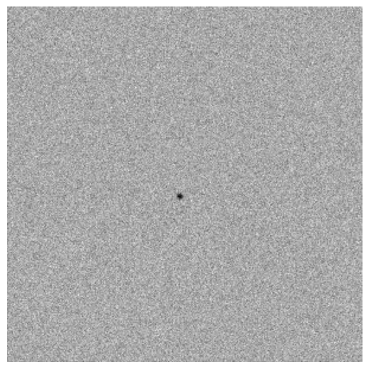

(c) Large beacon at 35 GHz

(d) Airplane at 95 GHz

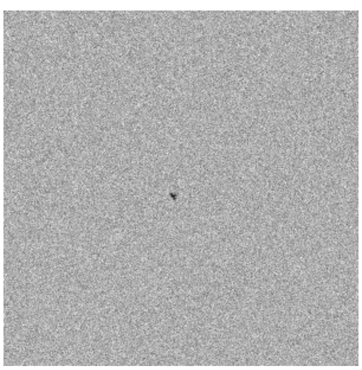

(e) Small beacon at 95 GHz

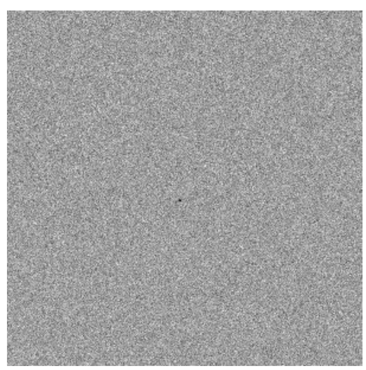

(f) Large beacon at 95 GHz

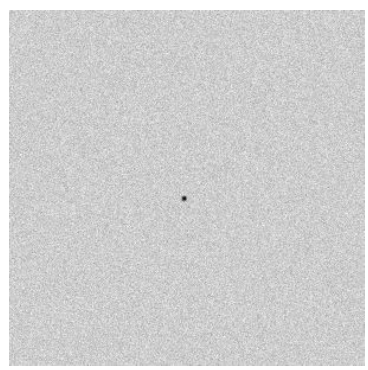

Table 3.5: Rain attenuation parameters for the Search and Rescue scenario, at a rainfall of $10\,\mathrm{mm\,h^{-1}}$ [34].

Frequency (GHz)	a	b	Attenuation ($\mathrm{dB\,km^{-1}}$)
35	0.235	1.009	2.4
95	1.06	0.745	5.9

search plane moved over the terrain, so we can still consider it as being visible from the air.

3.3.4 Rainy Weather

In this scenario, the weather is moderate rainfall, at a rate of $10\,\mathrm{mm\,h^{-1}}$. Attenuation at mmW frequencies for a rain rate R (given in $\mathrm{mm\,h^{-1}}$) is given by the empirical relation,

$$A = aR^b$$

where the parameters a and b are dependent on frequency and temperature. We use the values of a and b calculated by Olsen *et al.* in [34] for a rain temperature of $20\,°\mathrm{C}$. Values of a, b, and the associated loss are given in Table 3.5. For comparison, the attenuation at visible wavelengths is on the order of $4.5\,\mathrm{dB\,km^{-1}}$ at this rain rate [35]; however, in visible-wavelength imaging, the unattenuated signature would be much weaker, decreasing the effective range significantly.

We take the rainclouds as having a height between 1000 and 2000 m, and the rain a height up to 1500 m. The path loss from the aircraft to the ground is 4.8 dB at 35 GHz and 11.7 dB at 95 GHz. The image from this altitude is shown in Figure 3.16.

Notably, both the airplane and large beacon are still visible at 35 GHz; unfortunately, the small beacon has disappeared. The image is approximately on par with the image at 95 GHz through clouds (the second row of Figure 3.15). The 95 GHz image gives no useful information. Even unblurred (i.e. using an infinite-diameter aperture) the maximum temperature difference in the 95 GHz image is on the order of 2 K, which would be completely lost below the noise floor; there is simply nothing to see at this frequency.

Figure 3.16: Simulated mmW search and rescue from an altitude of 3000 m through $10\,\mathrm{mm\,h^{-1}}$ rain.

(a) Airplane at 35 GHz

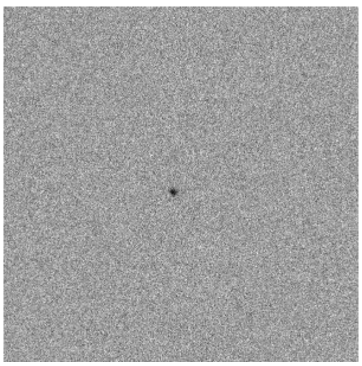

(b) Small beacon at 35 GHz

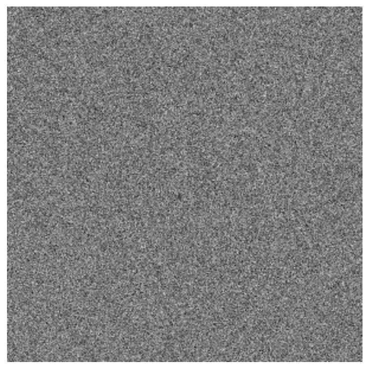

(c) Large beacon at 35 GHz

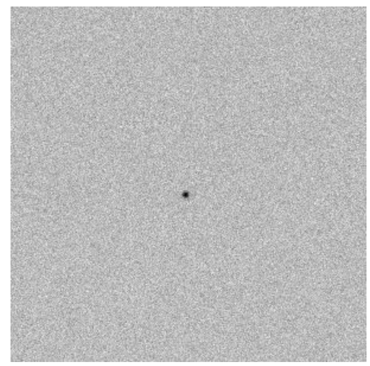

(d) Airplane at 95 GHz

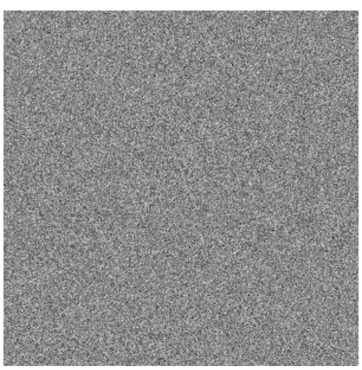

(e) Small beacon at 95 GHz

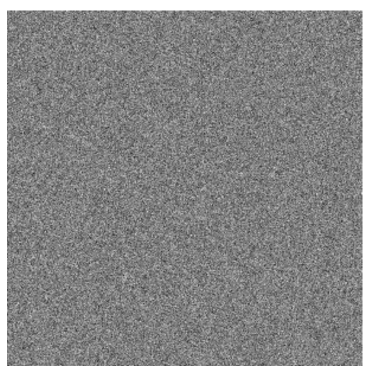

(f) Large beacon at 95 GHz

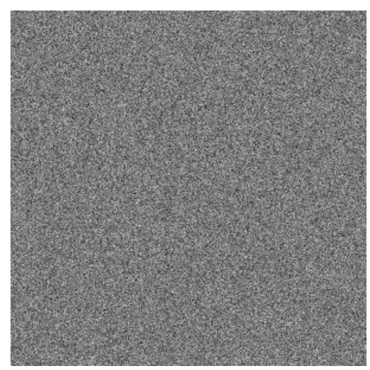

3.3.5 Conclusion

Millimeter waves capable of penetrating rain and clouds can assist in search-and-rescue operations under adverse weather conditions, particularly when combined with passive beacons placed by the target. Though the target cannot be resolved at 35 GHz, it can still be easily detected even through moderate rain. Thicker clouds and heavier rain (or higher-altitude clouds, so the rain accounts for more of the path) would increase the path loss, potentially making the mmW image unusable, though there is still some headroom at 35 GHz; however, poor weather also negatively affects other imaging techniques, so this is not in itself a mark against the pmmW system. An advantage of the pmmW system is that small scrub and clutter does not adversely effect the imager performance, as the contrast is too low for it to be visible. Also, most of the loss is in the lower atmosphere, through the rain and the clouds; if the imager aperture could be increased (and the resolution, such that the search target is larger than a single pixel), there is no real limit to how high the search plane could fly, or how large an area it could cover in a single pass, making it superior to conventional techniques; the challenge, of course, would be increasing the aperture size.

Chapter 4

CONCLUSIONS AND FUTURE WORK

We have described a methodology for simulating the images taken by a pmmW imaging system; moreover, we have implemented pmmW simulation capabilities in Blender, demonstrated the software's validity, and simulated three novel scenarios of interest to the pmmW imaging community.

Not covered in this thesis is the possibility of simulating scenes with active mmW sources. We already have the capability of performing active coherent simulation using physical optics implemented in Blender. However, it is prohibitively slow and memory-intensive, making it unusable for any reasonably-sized scenes we would be interested in simulating; current efforts include attempting to increase the speed and decrease the memory footprint.

Work on the simulation software was begun when the most recent version of Blender was 2.49b; in the time since, Blender has undergone major improvements in functionality and usability that are not reflected in the current program; future work includes porting the simulation capabilities to the most recent code version.

The software presented in this thesis, however, is still useful for simulation of passive phenomenology and has already been used in conjunction with an imager model to aid in the design of a real imaging system.

BIBLIOGRAPHY

[1] J. Nemarich. Microbolometer detectors for passive millimeter-wave imaging. Technical report, Army Research Laboratory, 2005.

[2] D. Notel, J. Huck, S. Neubert, S. Wirtz, and A. Tessmann. A compact mmw imaging radiometer for concealed weapon detection. In *Infrared and Millimeter Waves, 2007 and the 2007 15th International Conference on Terahertz Electronics. IRMMW-THz. Joint 32nd International Conference on*, pages 269 –270, sept. 2007.

[3] C.A. Schuetz, J. Murakowski, G.J. Schneider, and D.W. Prather. Radiometric millimeter-wave detection via optical upconversion and carrier suppression. *Microwave Theory and Techniques, IEEE Transactions on*, 53(5):1732 – 1738, may 2005.

[4] R. Appleby and H.B. Wallace. Standoff detection of weapons and contraband in the 100 ghz to 1 thz region. *Antennas and Propagation, IEEE Transactions on*, 55(11):2944 –2956, nov. 2007.

[5] Christopher A. Schuetz, E.L. Stein, Jr., J. Samluk, D. Mackrides, J.P. Wilson, R.D. Martin, T.E. Dillon, and D.W. Prather. Studies of millimeter-wave phenomenology for helicopter brownout mitigation. volume 7485, page 74850F. SPIE, 2009.

[6] The Blender Foundation, April 2012. `http://www.blender.org`.

[7] J.B. Keller. Geometrical theory of diffraction. *J. Opt. Soc. Am.*, 52(2):116–130, Feb 1962.

[8] N. Peinecke, H.U. Doehler, and B.R. Korn. Phong-like lighting for mmw radar simulation. volume 7117, page 71170M. SPIE, 2008.

[9] B.T. Phong. Illumination for computer generated pictures. *Communications of the ACM*, 18(6):311–317, June 1975.

[10] A.Y. Nashashibi and F.T. Ulaby. Mmw polarimetric radar bistatic scattering from a random surface. *Geoscience and Remote Sensing, IEEE Transactions on*, 45(6):1743 –1755, june 2007.

[11] E. Hecht and A. Zajac. *Optics*. Addison-Wesley Pub. Co., Reading, Mass. :, 2nd ed. edition, 1987.

[12] M.A. Dupertuis, M. Proctor, and B. Acklin. Generalization of complex snell-descartes and fresnel laws. *Journal of the Optical Society of America A*, 11(3):1159–1166, Mar 1994.

[13] S.W. Harmer, N. Rezgui, N. Bowring, Z. Luklinska, and G. Ren. Determination of the complex permittivity of textiles and leather in the 14-40 ghz millimetre-wave band using a free-wave transmittance only method. *Microwaves, Antennas Propagation, IET*, 2(6):606 –614, sept. 2008.

[14] Lijun Li, Yingzhou Wang, and Ke Gong. Measurements of building construction materials at ka-band. *International Journal of Infrared and Millimeter Waves*, 19:1293–1298, 1998. 10.1023/A:1022689229776.

[15] K. Sato, H. Kozima, H. Masuzawa, T. Manabe, T. Ihara, Y. Kasashima, and K. Yamaki. Measurements of reflection characteristics and refractive indices of interior construction materials in millimeter-wave bands. In *Vehicular Technology Conference, 1995 IEEE 45th*, volume 1, pages 449 –453 vol.1, jul 1995.

[16] H.J. Liebe. Mpm–an atmospheric millimeter-wave propagation model. *International Journal of Infrared and Millimeter Waves*, 10:631–650, 1989. 10.1007/BF01009565.

[17] P. H. Stone and J. H. Carlson. Atmospheric Lapse Rate Regimes and Their Parameterization. *Journal of Atmospheric Sciences*, 36:415–423, March 1979.

[18] J. P. Hollinger and R. C. Lo. Ssm/i project summary report. Technical report, Naval Research Laboratory, 1983.

[19] G.P. Kulemin. *Millimeter-Wave Radar Targets and Clutter*. Artech House Radar Library. Artech House, 2003.

[20] Olgagrie. Pickup truck 3d model, 2007.

[21] A.J. Gatesman, T.M. Goyette, J.C. Dickinson, J. Waldman, J. Neilson, and W.E. Nixon. Physical scale modeling the millimeter-wave backscattering behavior of ground clutter. Technical report, University of Massachusetts Lowell Submillimeter-Wave Technology Laboratory, 2001.

[22] silviuq12. Racing bicycle 3d model, 2011.

[23] Jaipur. Bicycle 3d model, 2007.

[24] T. Zwick, A. Chandrasekhar, C.W. Baks, U.R. Pfeiffer, S. Brebels, and B.P. Gaucher. Determination of the complex permittivity of packaging materials at millimeter-wave frequencies. *Microwave Theory and Techniques, IEEE Transactions on*, 54(3):1001 – 1010, march 2006.

[25] M.N. Afsar, K.A. Korolev, L. Subramanian, and I.I. Tkachov. Complex permittivity measurements of dielectrics and semiconductors at millimeter waves with high power sources. In *Microwave Symposium Digest, 2005 IEEE MTT-S International*, page 4 pp., june 2005.

[26] E. Altshuler. A simple expression for estimating attenuation by fog at millimeter wavelengths. *Antennas and Propagation, IEEE Transactions on*, 32(7):757 – 758, jul 1984.

[27] R.G. Eldridge. The Relationship Between Visibility and Liquid Water Content in Fog. *Journal of Atmospheric Sciences*, 28:1183–1186, October 1971.

[28] Manuel Bastioni. Makehuman, 2004.

[29] S.I. Alekseev and M.C. Ziskin. Human skin permittivity determined by millimeter wave reflection measurements. *Bioelectromagnetics*, 28(5):331–339, 2007.

[30] C. Gabriel. Compilation of the dielectric properties of body tissues at rf and microwave frequencies. Technical report, Armstrong Laboratory Air Force Material Command, 1995.

[31] 3dregenerator. Cessna 172 3d model, 2011.

[32] L.L. Frasch, S.J. McLean, and R.G. Olsen. Electromagnetic properties of dry and water saturated basalt rock, 1-110 ghz. *Geoscience and Remote Sensing, IEEE Transactions on*, 36(3):754 –766, may 1998.

[33] M.C.H. Wright. Atmospheric Phase Noise and Aperture Synthesis Imaging at Millimeter Wavelengths. *Publications of the Astronomical Society of the Pacific*, 108:520, June 1996.

[34] R. Olsen, D. Rogers, and D. Hodge. The arb relation in the calculation of rain attenuation. *Antennas and Propagation, IEEE Transactions on*, 26(2):318 – 329, mar 1978.

[35] D.E. Setzer. Computed transmission through rain at microwave and visible frequencies. *The Bell System Technical Journal*, 49(8):1873–1892, October 1970.

[36] M. Nurul Afsar. Precision millimeter-wave measurements of complex refractive index, complex dielectric permittivity, and loss tangent of common polymers. *IEEE Transactions on Instrumentation Measurement*, 36:530–536, June 1987.

[37] Etsuo Kawate and Kenichi Ishii. Determination of dielectric constant of a thin and low-dielectric film in the millimeter wave region. *Applied Physics Letters*, 84(24):4878 –4880, jun 2004.

[38] M.N. Afsar and K.J. Button. Precise millimeter-wave measurements of complex refractive index, complex dielectric permittivity and loss tangent of gaas, si, sio/sub 2/, a1/sub 2/o/sub 3/, beo, macor, and glass. *Microwave Theory and Techniques, IEEE Transactions on*, 31(2):217 –223, feb. 1983.

[39] G. Zhang, S. Nakaoka, and Y. Kobayashi. Millimeter wave measurements of temperature dependence of complex permittivity of dielectric plates by the cavity resonance method. In *Microwave Conference Proceedings, 1997. APMC '97, 1997 Asia-Pacific*, volume 3, pages 913 –916 vol.3, dec 1997.

[40] J. R. Izatt and F. Kremer. Millimeter wave measurement of both parts of the complex index of refraction using an untuned cavity resonator. *20:2555–2559*, July 1981.

[41] W.V. Sorin and D.F. Gray. Simultaneous thickness and group index measurement using optical low-coherence reflectometry. *Photonics Technology Letters, IEEE*, 4(1):105 –107, jan. 1992.

[42] Y.F. Gui, W.B. Dou, K. Yin, and P.G. Su. Automated and precise dielectric measurement systems at millimeter wavelengths using open resonator technique. In *Millimeter Waves, 2008. GSMM 2008. Global Symposium on*, pages 66 –69, april 2008.

[43] S. Chen, K.A. Korolev, K.N. Nguyen, and M.N. Afsar. Broad-band millimetre wave spectroscopy of common materials. In *Microwave Conference, 2007. European*, pages 692 –695, oct. 2007.

[44] Jonathan H Jiang and Dong L Wu. Ice and water permittivities for millimeter and sub-millimeter remote sensing applications. *Atmospheric Science Letters*, 5(7):146–151, 2004.

[45] M. J. Campbell and J. Ulrichs. Electrical properties of rocks and their significance for lunar radar observations. *74:5867–5881*, 1969.

[46] C. Matzler and A. Sume. Microwave radiometry of leaves. In P. Pampaloni, editor, *Microwave Radiometry and Remote Sensing Applications: Proceedings of the Specialist Meeting Held in Florence, Italy, 9-11 March, 1988*, pages 133–148, 1989.

[47] M.N. Afsar. Dielectric measurements of common polymers at millimeter wavelength. In *Microwave Symposium Digest, 1985 IEEE MTT-S International*, pages 439 –442, june 1985.

[48] G.L. Friedsam and E.M. Biebl. Precision free-space measurements of complex permittivity of polymers in the w-band. In *Microwave Symposium Digest, 1997., IEEE MTT-S International*, volume 3, pages 1351 –1354 vol.3, jun 1997.

[49] R J Cook and C B Rosenberg. Measurement of the complex refractive index of isotropic and anisotropic materials at 35 ghz using a free space microwave bridge. *Journal of Physics D: Applied Physics*, 12(10):1643, 1979.

[50] A. J. Gatesman, A. Danylov, T. M. Goyette, J. C. Dickinson, R. H. Giles, W. Goodhue, J. Waldman, W. E. Nixon, and W. Hoen. Terahertz behavior of optical components and common materials. In *Society of Photo-Optical Instrumentation Engineers (SPIE) Conference Series*, volume 6212 of *Society of Photo-Optical Instrumentation Engineers (SPIE) Conference Series*, June 2006.

[51] C. M. Alabaster. *The microwave properties of tissue and other lossy dielectrics*. PhD thesis, Cranfield University, 2004.

[52] T. Meissner and F.J. Wentz. The complex dielectric constant of pure and sea water from microwave satellite observations. *Geoscience and Remote Sensing, IEEE Transactions on*, 42(9):1836 – 1849, sept. 2004.

[53] Julius Adams Stratton. *Electromagnetic theory*. McGraw-Hill, New York :, 1st ed. edition, 1941.

Appendix A

DIELECTRIC CONSTANTS OF SELECTED MATERIALS

Most materials are not well-characterized at mmW frequencies. There are a number of reasons for this, including the difficulty in collecting dielectric constant data, variability in materials making it impossible to obtain a single overall value for any parameter, and, until recently, lack of utility of such measurements. It is also usually the case that, when a new measurement technique is presented, the authors validate it against some well-characterized material (e.g. Teflon or polypropylene) but do not perform measurements of novel materials; when new materials are explored, it is typically with the aim of characterizing materials for mmW integrated circuits or similar non-imaging applications [36, 37, 38, 39, 40, 41, 42, 15], so many measurements exist of e.g. semiconductor materials or other mmW components that are rarely found in nature. This section contains a compilation of material properties we have found useful for scene simulation.

Note that differences in measurement techniques and material samples will lead to differences in reported dielectric properties; moreover, there is typically a range of materials known as e.g. concrete or fiberglass with different material properties. Therefore, when possible, measurements should be performed on the material one is hoping to simulate. However, as demonstrated in Section 2.3, even approximately correct material parameters give good results if the geometry is modeled correctly.

Table A.1: mmW dielectric properties of common materials.

	Dielectric Constant				
	35 GHz		95 GHz		
Material	ε_r'	ε_r''	ε_r'	ε_r''	Reference
Concrete	5.5	0.5	2.49	6.8×10^{-2}	[19, 15]
Asphalt	2.5	0.6	–	–	[19]
Brick	1.3	7.4×10^{-2}	–	–	[14]
Sand	3.0	0.56	4.6	7×10^{-3}	[19, 43]
Ice	3.1	2×10^{-3}	3.1	9×10^{-3}	[44]
Dry soil	3.1	0.2	2.9	0.2	[21]
Moist soil	4.9	2.1	3.1	1.2	[21]
Basalt	6.7	0.28	6.8	0.45	[32]
Granite	5.3	2.3×10^{-2}	–	–	[45]
Denim	1.6	6×10^{-2}	–	–	[13]
Beige leather	2.2	6×10^{-2}	–	–	[13]
Human skin	14	16	5.9	9.4	[29, 30]
Oak leaves	7.3	5.6	4.1	3.3	[46]
Polypropylene	2.3	1.8×10^{-4}	2.26	1.3×10^{-3}	[47, 48]
Plexiglass	2.3	2×10^{-2}	2.59	1.9×10^{-2}	[25, 48]
Nylon	2.99	2.1×10^{-2}	2.99	2.5×10^{-2}	[49, 48]
Fiberglass	4.3	0.11	3.78	9.3×10^{-2}	[50, 51]
Water	12.5	22.5	6.65	9.4	[52]
Salt water	12.3	23.2	5.82	10.1	[52]

Appendix B

DERIVATIONS

There are several derivations that were glossed over in the body of this thesis. For the sake of completeness, we include them here.

B.1 Mathematical Background

Unless noted otherwise, all vector quantities used in this thesis occupy the space $\mathbb{C}^3$. That is, a vector $\mathbf{A}$ can be written

$$\mathbf{A} = a_x\hat{\mathbf{x}} + a_y\hat{\mathbf{y}} + a_z\hat{\mathbf{z}}$$

where a_j is a complex number and the real vectors $\hat{\mathbf{x}}$, $\hat{\mathbf{y}}$, and $\hat{\mathbf{z}}$ form an orthonormal basis spanning $\mathbb{C}^3$; $\hat{\mathbf{x}}$, $\hat{\mathbf{y}}$, and $\hat{\mathbf{z}}$ need not be real.

The dot product is defined as

$$\mathbf{A} \cdot \mathbf{B} = \sum_j a_j b_j$$

The standard definition for the dot product for complex vectors is $\mathbf{A} \cdot \mathbf{B} = \sum_j a_j b_j^*$ because that allows the dot product to be used as an inner product on $\mathbb{C}^3$ as it is on $\mathbb{R}^3$. Therefore caution is required when implementing the simulation using existing software libraries.

Using this dot product we define the unit vector in the direction of $\mathbf{A}$ (i.e. the vector $\hat{\mathbf{A}}$ such that $\mathbf{A} = A\hat{\mathbf{A}}$ with $\hat{\mathbf{A}} \cdot \hat{\mathbf{A}} = 1$)

$$\hat{\mathbf{A}} = \frac{\mathbf{A}}{\sqrt{\mathbf{A} \cdot \mathbf{A}}}$$

$$A = \sqrt{\mathbf{A} \cdot \mathbf{A}}$$

Note here that due to the definition of the dot product the magnitude A is not necessarily a real number.

The cross product is defined in the usual way

$$\mathbf{A}\times\mathbf{B}=\begin{vmatrix}\hat{\mathbf{x}} & \hat{\mathbf{y}} & \hat{\mathbf{z}}\\ a_x & a_y & a_z\\ b_x & b_y & b_z\end{vmatrix}=\hat{\mathbf{x}}\left(a_yb_z-a_zb_y\right)-\hat{\mathbf{y}}\left(a_xb_z-a_zb_x\right)+\hat{\mathbf{z}}\left(a_xb_y-a_yb_x\right)$$

These definitions allow us to use the standard vector identities

$$\mathbf{A}\cdot(\mathbf{B}\times\mathbf{C})=\mathbf{B}\cdot(\mathbf{C}\times\mathbf{A})=\mathbf{C}\cdot(\mathbf{A}\times\mathbf{B}) \tag{B.1}$$

$$\mathbf{A}\times(\mathbf{B}\times\mathbf{C})=(\mathbf{A}\cdot\mathbf{C})\,\mathbf{B}-(\mathbf{A}\cdot\mathbf{B})\,\mathbf{C} \tag{B.2}$$

$$(\mathbf{A}\times\mathbf{B})\cdot(\mathbf{C}\times\mathbf{D})=(\mathbf{A}\cdot\mathbf{C})\,(\mathbf{B}\cdot\mathbf{D})-(\mathbf{B}\cdot\mathbf{C})\,(\mathbf{A}\cdot\mathbf{D}) \tag{B.3}$$

$$(\mathbf{A}\times\mathbf{B})\times(\mathbf{C}\times\mathbf{D})=(\mathbf{A}\cdot\mathbf{B}\times\mathbf{D})\,\mathbf{C}-(\mathbf{A}\cdot\mathbf{B}\times\mathbf{C})\,\mathbf{D} \tag{B.4}$$

where $\mathbf{A}$, $\mathbf{B}$, $\mathbf{C}$, and $\mathbf{D}$ are arbitrary (real or complex) vectors.

B.2 Phase Matching Condition

One boundary condition is the continuity of the tangential electric field across any boundary. This can be written as

$$(\mathbf{E}_i+\mathbf{E}_r-\mathbf{E}_t)\cdot\mathbf{n}_\perp=0 \tag{B.5a}$$

$$\left(\mathbf{E}_i^0e^{i(\mathbf{k}_i\cdot\mathbf{n}_\perp-\omega t)}+\mathbf{E}_r^0e^{i(\mathbf{k}_r\cdot\mathbf{n}_\perp-\omega t)}-\mathbf{E}_t^0e^{i(\mathbf{k}_t\cdot\mathbf{n}_\perp-\omega t)}\right)\cdot\mathbf{n}_\perp=0 \tag{B.5b}$$

where $\mathbf{n}_\perp$ is any vector such that $\mathbf{n}_\perp\cdot\hat{\mathbf{n}}=0$ (i.e. it is on the interface). Every term varies with a $e^{i\mathbf{k}\cdot\mathbf{n}_\perp}$ dependence; because the boundary condition must be satisfied over the entire interface, we require that

$$\mathbf{k}_i\cdot\mathbf{n}_\perp=\mathbf{k}_r\cdot\mathbf{n}_\perp=\mathbf{k}_t\cdot\mathbf{n}_\perp \tag{B.6}$$

Because $\hat{\mathbf{n}}\cdot\hat{\mathbf{n}}=1$ and $\hat{\mathbf{n}}\cdot\mathbf{n}_\perp=0$ we can write

$$\mathbf{k}\cdot\mathbf{n}_\perp=(\mathbf{k}\cdot\mathbf{n}_\perp)\,(\hat{\mathbf{n}}\cdot\hat{\mathbf{n}})-(\hat{\mathbf{n}}\cdot\mathbf{n}_\perp)\,(\mathbf{k}\cdot\hat{\mathbf{n}})$$

This has the form of Equation B.3. Thus,

$$(\mathbf{k}_i \times \hat{\mathbf{n}}) \cdot (\mathbf{n}_\perp \times \hat{\mathbf{n}}) = (\mathbf{k}_r \times \hat{\mathbf{n}}) \cdot (\mathbf{n}_\perp \times \hat{\mathbf{n}}) = (\mathbf{k}_t \times \hat{\mathbf{n}}) \cdot (\mathbf{n}_\perp \times \hat{\mathbf{n}})$$

Because $\mathbf{n}_\perp$ is arbitrary, $\mathbf{n}_\perp \times \hat{\mathbf{n}}$ can be any vector on the interface. Therefore

$$\mathbf{k}_i \times \hat{\mathbf{n}} = \mathbf{k}_r \times \hat{\mathbf{n}} = \mathbf{k}_t \times \hat{\mathbf{n}}$$

B.3 Amplitude Reflection and Transmission Coefficients

We consider the geometry defined in Section 2.2.1. We have defined the fields in terms of the local coordinates $\hat{\mathbf{s}}$ and $\hat{\mathbf{p}}$ (Equation 2.23) as

$$\mathbf{E} = E_s\hat{\mathbf{s}} + E_p\hat{\mathbf{p}} \tag{B.7a}$$

$$\mathbf{H} = H_s\hat{\mathbf{p}} + H_p\hat{\mathbf{s}} \tag{B.7b}$$

We now seek a relationship between E_s, H_s, E_p, and H_p. Applying Equations 2.4c, 2.23, and B.2

$$H_s\hat{\mathbf{p}} + H_p\hat{\mathbf{s}} = \frac{k}{\omega\mu}\hat{\mathbf{k}} \times (E_s\hat{\mathbf{s}} + E_p\hat{\mathbf{p}}) = \frac{k}{\omega\mu}(E_s\hat{\mathbf{p}} - E_p\hat{\mathbf{s}})$$

$$H_s = \frac{k}{\omega\mu}E_s \tag{B.8a}$$

$$H_p = -\frac{k}{\omega\mu}E_p \tag{B.8b}$$

Beginning with Equations 2.22a and 2.22b, we use Equations B.7a and B.7b for the incident, reflected, and transmitted fields

$$\hat{\mathbf{n}} \times (E_{s,i}\hat{\mathbf{s}} + E_{p,i}\hat{\mathbf{p}}_i) + \hat{\mathbf{n}} \times (E_{s,r}\hat{\mathbf{s}} + E_{p,r}\hat{\mathbf{p}}_r) - \hat{\mathbf{n}} \times (E_{s,t}\hat{\mathbf{s}} + E_{p,t}\hat{\mathbf{p}}_t) = 0$$

$$\hat{\mathbf{n}} \times (H_{s,i}\hat{\mathbf{p}}_i + H_{p,i}\hat{\mathbf{s}}) + \hat{\mathbf{n}} \times (H_{s,r}\hat{\mathbf{p}}_r + H_{p,r}\hat{\mathbf{s}}) - \hat{\mathbf{n}} \times (H_{s,t}\hat{\mathbf{p}}_t + H_{p,t}\hat{\mathbf{s}}) = 0$$

We know from applying Equation B.2 to Equation 2.23 that

$$\begin{aligned}\hat{\mathbf{n}} \times \hat{\mathbf{p}} &= \hat{\mathbf{n}} \times \left(\hat{\mathbf{k}} \times \hat{\mathbf{s}}\right) = \hat{\mathbf{n}} \times \left(\frac{\hat{\mathbf{k}} \times \left(\hat{\mathbf{n}} \times \hat{\mathbf{k}}\right)}{\sqrt{(\hat{\mathbf{n}} \times \hat{\mathbf{k}}) \cdot (\hat{\mathbf{n}} \times \hat{\mathbf{k}})}}\right) \\ &= \hat{\mathbf{n}} \times \left(\frac{\hat{\mathbf{n}} - \left(\hat{\mathbf{k}} \cdot \hat{\mathbf{n}}\right)\hat{\mathbf{k}}}{\sqrt{(\hat{\mathbf{n}} \times \hat{\mathbf{k}}) \cdot (\hat{\mathbf{n}} \times \hat{\mathbf{k}})}}\right) = -\left(\hat{\mathbf{k}} \cdot \hat{\mathbf{n}}\right)\hat{\mathbf{s}}\end{aligned} \tag{B.9}$$

This allows us to group terms that are perpendicular and parallel to $\hat{\mathbf{s}}$

$$\left(E_{s,i} + E_{s,r} - E_{s,t}\right) \hat{\mathbf{n}} \times \hat{\mathbf{s}} = 0 \tag{B.10a}$$

$$\left(H_{p,i} + H_{p,r} - H_{p,t}\right) \hat{\mathbf{n}} \times \hat{\mathbf{s}} = 0 \tag{B.10b}$$

$$\left(E_{p,i}\hat{\mathbf{k}}_i \cdot \hat{\mathbf{n}} + E_{p,r}\hat{\mathbf{k}}_r \cdot \hat{\mathbf{n}} - E_{p,t}\hat{\mathbf{k}}_t \cdot \hat{\mathbf{n}}\right) \hat{\mathbf{s}} = 0 \tag{B.10c}$$

$$\left(H_{s,i}\hat{\mathbf{k}}_i \cdot \hat{\mathbf{n}} + H_{s,r}\hat{\mathbf{k}}_r \cdot \hat{\mathbf{n}} - H_{s,t}\hat{\mathbf{k}}_t \cdot \hat{\mathbf{n}}\right) \hat{\mathbf{s}} = 0 \tag{B.10d}$$

Dividing Equations B.10a and B.10b by $E_{s,i}$ and $H_{p,i}$, respectively, and using the definition of r_s, r_p, t_s, and t_p from Equations 2.24 and 2.25, we obtain

$$1 + r_s - t_s = 0$$

$$1 + r_p - t_p = 0$$

Substituting for E_p and H_s in Equations B.10c and B.10d from Equations B.8a and B.8b

$$\begin{aligned} -\frac{\omega\mu}{k_i} H_{p,i}\hat{\mathbf{k}}_i \cdot \hat{\mathbf{n}} - \frac{\omega\mu}{k_r} H_{p,r}\hat{\mathbf{k}}_r \cdot \hat{\mathbf{n}} + \frac{\omega\mu}{k_t} H_{p,t}\hat{\mathbf{k}}_t \cdot \hat{\mathbf{n}} = 0 \\ \frac{k_i}{\omega\mu} E_{s,i}\hat{\mathbf{k}}_i \cdot \hat{\mathbf{n}} + \frac{k_r}{\omega\mu} E_{s,r}\hat{\mathbf{k}}_r \cdot \hat{\mathbf{n}} - \frac{k_t}{\omega\mu} E_{s,t}\hat{\mathbf{k}}_t \cdot \hat{\mathbf{n}} = 0 \end{aligned}$$

Using the dispersion relation $k^2 = \omega^2\mu\varepsilon$ we know that $\omega\mu/k = k/\omega\varepsilon$. We have also defined $\mathbf{k} = k\hat{\mathbf{k}}$; additionally, both ω and μ are constants, so we cancel them. This gives

$$\begin{aligned} -\frac{1}{\varepsilon_1} H_{p,i}\mathbf{k}_i \cdot \hat{\mathbf{n}} - \frac{1}{\varepsilon_1} H_{p,r}\mathbf{k}_r \cdot \hat{\mathbf{n}} + \frac{1}{\varepsilon_2} H_{p,t}\mathbf{k}_t \cdot \hat{\mathbf{n}} = 0 \\ E_{s,i}\mathbf{k}_i \cdot \hat{\mathbf{n}} + E_{s,r}\mathbf{k}_r \cdot \hat{\mathbf{n}} - E_{s,t}\mathbf{k}_t \cdot \hat{\mathbf{n}} = 0 \end{aligned}$$

Dividing through by $H_{p,i}$ and $E_{p,i}$, multiplying the first equation by $\varepsilon_1\varepsilon_2$, and grouping terms

$$\begin{aligned} r_p\left(\varepsilon_1\mathbf{k}_t \cdot \hat{\mathbf{n}} - \varepsilon_2\mathbf{k}_r \cdot \hat{\mathbf{n}}\right) - \varepsilon_2\mathbf{k}_i \cdot \hat{\mathbf{n}} + \varepsilon_1\mathbf{k}_t \cdot \hat{\mathbf{n}} = 0 \\ r_s\left(\mathbf{k}_r \cdot \hat{\mathbf{n}} - \mathbf{k}_t \cdot \hat{\mathbf{n}}\right) + \mathbf{k}_i \cdot \hat{\mathbf{n}} - \mathbf{k}_t \cdot \hat{\mathbf{n}} = 0 \end{aligned}$$

$$r_p = \frac{\varepsilon_1 \mathbf{k}_t \cdot \hat{\mathbf{n}} - \varepsilon_2 \mathbf{k}_i \cdot \hat{\mathbf{n}}}{\varepsilon_1 \mathbf{k}_t \cdot \hat{\mathbf{n}} - \varepsilon_2 \mathbf{k}_r \cdot \hat{\mathbf{n}}}$$
$$r_s = -\frac{\mathbf{k}_i \cdot \hat{\mathbf{n}} - \mathbf{k}_t \cdot \hat{\mathbf{n}}}{\mathbf{k}_r \cdot \hat{\mathbf{n}} - \mathbf{k}_t \cdot \hat{\mathbf{n}}}$$

Finally, we note from Equation 2.21 that $\mathbf{k}_r \cdot \hat{\mathbf{n}} = -\mathbf{k}_i \cdot \hat{\mathbf{n}}$; substituting this and canceling negative signs completes the derivation.

B.4 Poynting Vector

We begin with the standard expression for a propagating wave

$$\mathbf{E} = \mathbf{E}_0 e^{i(\mathbf{k}\cdot\mathbf{r}-\omega t)}$$
$$\mathbf{H} = \mathbf{H}_0 e^{i(\mathbf{k}\cdot\mathbf{r}-\omega t)}$$

Then the time-averaged power flow is given by the Poynting vector

$$\mathbf{S} = \frac{1}{2}\mathfrak{Re}\left\{\mathbf{E}\times\mathbf{H}^*\right\} = \frac{1}{2}\mathfrak{Re}\left\{\mathbf{E}_0 e^{i(\mathbf{k}\cdot\mathbf{r}-\omega t)} \times \mathbf{H}_0^* e^{-i(\mathbf{k}^*\cdot\mathbf{r}-\omega t)}\right\} = \frac{1}{2}e^{2\mathfrak{Im}(\mathbf{k})\cdot\mathbf{r}}\mathfrak{Re}\left\{\mathbf{E}_0\times\mathbf{H}_0^*\right\}$$

We know from Maxwell's equations that $\mathbf{H}_0 = \mathbf{k}\times\mathbf{E}_0/\omega\mu_0$. Thus

$$\mathbf{S} = \frac{e^{2\mathfrak{Im}(\mathbf{k})\cdot\mathbf{r}}}{2\omega\mu}\mathfrak{Re}\left\{\mathbf{E}_0\times\left(\mathbf{k}^*\times\mathbf{E}_0^*\right)\right\}$$

Evaluating the quantity $\mathbf{E}_0\times(\mathbf{k}^*\times\mathbf{E}_0^*)$ using Equation B.2

$$\begin{aligned}\mathbf{S} &= \frac{e^{2\mathfrak{Im}(\mathbf{k})\cdot\mathbf{r}}}{2\omega\mu}\mathfrak{Re}\left\{\left(\mathbf{E}_0\cdot\mathbf{E}_0^*\right)\mathbf{k}^* - \left(\mathbf{E}_0\cdot\mathbf{k}^*\right)\mathbf{E}_0^*\right\}\\ &= \frac{e^{2\mathfrak{Im}(\mathbf{k})\cdot\mathbf{r}}}{2\omega\mu}\left[\left(\mathbf{E}_0\cdot\mathbf{E}_0^*\right)\mathfrak{Re}\left\{\mathbf{k}\right\} - \mathfrak{Re}\left\{\left(\mathbf{k}^*\cdot\mathbf{E}_0\right)\mathbf{E}_0^*\right\}\right]\end{aligned}$$

From Maxwell's equations, $\mathbf{E}_0\cdot\mathbf{k} = \mathbf{E}_0^*\cdot\mathbf{k}^* = 0$. Therefore

$$-\left(\mathbf{k}^*\cdot\mathbf{E}_0\right)\mathbf{E}_0^* = \left(\mathbf{k}^*\cdot\mathbf{E}_0^*\right)\mathbf{E}_0 - \left(\mathbf{k}^*\cdot\mathbf{E}_0\right)\mathbf{E}_0^*$$

which has the form of the right side of Equation B.2. Making this substitution

$$\mathbf{S} = \frac{e^{2\mathfrak{Im}(\mathbf{k})\cdot\mathbf{r}}}{2\omega\mu}\left[\left(\mathbf{E}_0\cdot\mathbf{E}_0^*\right)\mathfrak{Re}\left\{\mathbf{k}\right\} + \mathfrak{Re}\left\{\mathbf{k}^*\times\left(\mathbf{E}_0\times\mathbf{E}_0^*\right)\right\}\right]$$

The product $\mathbf{E}_0\times\mathbf{E}_0^*$ is purely imaginary (or zero, if $\mathbf{E}_0$ is real). Therefore, we make the substitution $\mathbf{E}_0\times\mathbf{E}_0^* = i\mathbf{v}$ where $\mathbf{v}$ is real. Then

$$\mathfrak{Re}\left\{\mathbf{k}^*\times\left(\mathbf{E}_0\times\mathbf{E}_0^*\right)\right\} = \mathfrak{Re}\left\{i\mathbf{k}^*\times\mathbf{v}\right\} = -\mathfrak{Im}\left\{\mathbf{k}^*\right\}\times\mathbf{v} = \mathfrak{Im}\left\{\mathbf{k}\right\}\times\mathbf{v}$$

Substituting back $\mathbf{v} = -i\mathbf{E}_0 \times \mathbf{E}_0^*$ gives the Poynting vector

$$\mathbf{S} = \frac{e^{2\mathfrak{Im}(\mathbf{k})\cdot\mathbf{r}}}{2\omega\mu}\left[\left(\mathbf{E}_0 \cdot \mathbf{E}_0^*\right)\mathfrak{Re}\left\{\mathbf{k}\right\} - i\mathfrak{Im}\left\{\mathbf{k}\right\} \times \left(\mathbf{E}_0 \times \mathbf{E}_0^*\right)\right]$$

B.5 Power Reflection and Transmission Coefficients

We consider the geometry defined in Section 2.2.1. We know that at steady-state, in a time-averaged sense we have conservation of energy across an interface. Additionally, at the surface itself we have no dissipation. Then, we can write the conservation of energy across an interface in terms of the Poynting vector in medium 1 and 2, denoted $\mathbf{S}_1$ and $\mathbf{S}_2$ as

$$\mathbf{S}_1 \cdot \hat{\mathbf{n}} = \mathbf{S}_2 \cdot \hat{\mathbf{n}} \tag{B.11}$$

The power flux in medium 2 is due only to the field transmitted from medium 1 to medium 2; we denote this $\mathbf{S}_t$. In medium 1, however, we have power flux $\mathbf{S}_i$ due to the incident field, power flux $\mathbf{S}_r$ due to the reflected field, and an *additional* term $\mathbf{S}_m$ due to the interference of incident and reflected fields. Thus

$$\left(\mathbf{S}_i + \mathbf{S}_r + \mathbf{S}_m\right) \cdot \hat{\mathbf{n}} = \mathbf{S}_t \cdot \hat{\mathbf{n}} \tag{B.12}$$

$$\mathbf{S}_i = \mathfrak{Re}\left\{\mathbf{E}_i \times \mathbf{H}_i^*\right\} \tag{B.13a}$$

$$\mathbf{S}_r = \mathfrak{Re}\left\{\mathbf{E}_r \times \mathbf{H}_r^*\right\} \tag{B.13b}$$

$$\mathbf{S}_m = \mathfrak{Re}\left\{\mathbf{E}_i \times \mathbf{H}_r^* + \mathbf{E}_r \times \mathbf{H}_i^*\right\} \tag{B.13c}$$

$$\mathbf{S}_t = \mathfrak{Re}\left\{\mathbf{E}_t \times \mathbf{H}_t^*\right\} \tag{B.13d}$$

In fact, the statement of energy conservation in Equation B.12 is not the most general condition on energy flux at the boundary as we require only continuity of the real part of $\mathbf{E} \times \mathbf{H}$, i.e. the time-averaged power flux. The imaginary part of $\mathbf{E} \times \mathbf{H}$, however, is related to the average stored energy [53] and this quantity must *also* be continuous across the interface. Therefore, the general energy conservation relation is

$$\left(\mathcal{S}_i + \mathcal{S}_r + \mathcal{S}_m\right) \cdot \hat{\mathbf{n}} = \mathcal{S}_t \cdot \hat{\mathbf{n}} \tag{B.14}$$

$$\mathcal{S}_i = \mathbf{E}_i \times \mathbf{H}_i^* \tag{B.15a}$$

$$\mathcal{S}_r = \mathbf{E}_r \times \mathbf{H}_r^* \tag{B.15b}$$

$$\mathcal{S}_m = \mathbf{E}_i \times \mathbf{H}_r^* + \mathbf{E}_r \times \mathbf{H}_i^* \tag{B.15c}$$

$$\mathcal{S}_t = \mathbf{E}_t \times \mathbf{H}_t^* \tag{B.15d}$$

We now evaluate $\mathcal{S}_i$, $\mathcal{S}_r$, $\mathcal{S}_m$, and $\mathcal{S}_t$. To do this, we decompose $\mathbf{E}$ and $\mathbf{H}$ using Equations B.7 and B.8, and substitute values of r and t defined in Equations 2.24 and 2.25, and use the fact that $\omega\mu/k = k/\omega\varepsilon$. Doing this we obtain

$$\begin{aligned}
\mathcal{S}_i &= \mathbf{E}_i \times \mathbf{H}_i^* = (E_{s,i}\hat{\mathbf{s}}_i + E_{p,i}\hat{\mathbf{p}}_i) \times \left(H_{s,i}^*\hat{\mathbf{p}}_i^* + H_{p,i}^*\hat{\mathbf{s}}_i^*\right) \\
&= E_{s,i}H_{s,i}^*\hat{\mathbf{s}} \times \hat{\mathbf{p}}_i^* + E_{p,i}H_{p,i}^*\hat{\mathbf{p}}_i \times \hat{\mathbf{s}}^* + E_{s,i}H_{p,i}^*\hat{\mathbf{s}} \times \hat{\mathbf{s}}^* + E_{p,i}H_{s,i}^*\hat{\mathbf{p}}_i \times \hat{\mathbf{p}}_i^* \\
&= \frac{k_1^*}{\omega\mu}E_{s,i}E_{s,i}^*\hat{\mathbf{s}} \times \hat{\mathbf{p}}_i^* - \frac{k_1}{\omega\varepsilon_1}H_{p,i}H_{p,i}^*\hat{\mathbf{p}}_i \times \hat{\mathbf{s}}^* + E_{s,i}H_{p,i}^*\hat{\mathbf{s}} \times \hat{\mathbf{s}}^* - \frac{k_1^*}{k_1}H_{p,i}E_{s,i}^*\hat{\mathbf{p}}_i \times \hat{\mathbf{p}}_i^* \\
\mathcal{S}_r &= \mathbf{E}_r \times \mathbf{H}_r^* = (E_{s,r}\hat{\mathbf{s}} + E_{p,r}\hat{\mathbf{p}}_r) \times \left(H_{s,r}^*\hat{\mathbf{p}}_r^* + H_{p,r}^*\hat{\mathbf{s}}^*\right) \\
&= E_{s,r}H_{s,r}^*\hat{\mathbf{s}} \times \hat{\mathbf{p}}_r^* + E_{p,r}H_{p,r}^*\hat{\mathbf{p}}_r \times \hat{\mathbf{s}}^* + E_{s,r}H_{p,r}^*\hat{\mathbf{s}} \times \hat{\mathbf{s}}^* + E_{p,r}H_{s,r}^*\hat{\mathbf{p}}_r \times \hat{\mathbf{p}}_r^* \\
&= \frac{k_1^*}{\omega\mu}r_s r_s^* E_{s,i}E_{s,i}^*\hat{\mathbf{s}} \times \hat{\mathbf{p}}_r^* - \frac{k_1}{\omega\varepsilon_1}r_p r_p^* H_{p,i}H_{p,i}^*\hat{\mathbf{p}}_r \times \hat{\mathbf{s}}^* \\
&+ r_s r_p^* E_{s,i}H_{p,i}^*\hat{\mathbf{s}} \times \hat{\mathbf{s}}^* - \frac{k_1^*}{k_1}r_p r_s^* H_{p,i}E_{s,i}^*\hat{\mathbf{p}}_r \times \hat{\mathbf{p}}_r^* \\
\mathcal{S}_m &= \mathbf{E}_i \times \mathbf{H}_r^* + \mathbf{E}_r \times \mathbf{H}_i^* = \begin{bmatrix} (E_{s,i}\hat{\mathbf{s}} + E_{p,i}\hat{\mathbf{p}}_i) \times \left(H_{s,r}^*\hat{\mathbf{p}}_r^* + H_{p,r}^*\hat{\mathbf{s}}^*\right) \\ + (E_{s,r}\hat{\mathbf{s}} + E_{p,r}\hat{\mathbf{p}}_r) \times \left(H_{s,i}^*\hat{\mathbf{p}}_i^* + H_{p,i}^*\hat{\mathbf{s}}^*\right) \end{bmatrix} \\
&= \begin{bmatrix} E_{s,i}H_{s,r}^*\hat{\mathbf{s}} \times \hat{\mathbf{p}}_r^* + E_{p,i}H_{p,r}^*\hat{\mathbf{p}}_i \times \hat{\mathbf{s}}^* + E_{s,i}H_{p,r}^*\hat{\mathbf{s}} \times \hat{\mathbf{s}}^* + E_{p,i}H_{s,r}^*\hat{\mathbf{p}}_i \times \hat{\mathbf{p}}_r^* \\ + E_{s,r}H_{s,i}^*\hat{\mathbf{s}} \times \hat{\mathbf{p}}_i^* + E_{p,r}H_{p,i}^*\hat{\mathbf{p}}_r \times \hat{\mathbf{s}}^* + E_{s,r}H_{p,i}^*\hat{\mathbf{s}} \times \hat{\mathbf{s}}^* + E_{p,r}H_{s,i}^*\hat{\mathbf{p}}_r \times \hat{\mathbf{p}}_i^* \end{bmatrix} \\
&= \begin{bmatrix} \frac{k_1^*}{\omega\mu}r_s^* E_{s,i}E_{s,i}^*\hat{\mathbf{s}} \times \hat{\mathbf{p}}_r^* - \frac{k_1}{\omega\varepsilon_1}r_p^* H_{p,i}H_{p,i}^*\hat{\mathbf{p}}_i \times \hat{\mathbf{s}}^* + r_p^* E_{s,i}H_{p,i}^*\hat{\mathbf{s}} \times \hat{\mathbf{s}}^* \\ + \frac{k_1^*}{\omega\mu}r_s E_{s,i}E_{s,i}^*\hat{\mathbf{s}} \times \hat{\mathbf{p}}_i^* - \frac{k_1}{\omega\varepsilon_1}r_p H_{p,i}H_{p,i}^*\hat{\mathbf{p}}_r \times \hat{\mathbf{s}}^* + r_s E_{s,i}H_{p,i}^*\hat{\mathbf{s}} \times \hat{\mathbf{s}}^* \\ - \frac{k_1^*}{k_1}r_s^* H_{p,i}E_{s,i}^*\hat{\mathbf{p}}_i \times \hat{\mathbf{p}}_r^* - \frac{k_1^*}{k_1}r_p H_{p,i}E_{s,i}^*\hat{\mathbf{p}}_r \times \hat{\mathbf{p}}_i^* \end{bmatrix}
\end{aligned}$$

$$\begin{aligned}\mathcal{S}_t &= \mathbf{E}_t \times \mathbf{H}_t^* = \left(E_{s,t}\hat{\mathbf{s}} + E_{p,t}\hat{\mathbf{p}}_t\right) \times \left(H_{s,t}^*\hat{\mathbf{p}}_t^* + H_{p,t}^*\hat{\mathbf{s}}^*\right)\\ &= E_{s,t}H_{s,t}^*\hat{\mathbf{s}} \times \hat{\mathbf{p}}_t^* + E_{s,t}H_{p,t}^*\hat{\mathbf{s}} \times \hat{\mathbf{s}}^* + E_{p,t}H_{s,t}^*\hat{\mathbf{p}}_t \times \hat{\mathbf{p}}_t^* + E_{p,t}H_{p,t}^*\hat{\mathbf{p}}_t \times \hat{\mathbf{s}}^*\\ &= \frac{k_2^*}{\omega\mu}t_s t_s^* E_{s,i}E_{s,i}^*\hat{\mathbf{s}} \times \hat{\mathbf{p}}_t^* - \frac{k_2}{\omega\varepsilon_2}t_p t_p^* H_{p,i}H_{p,i}^*\hat{\mathbf{p}}_t \times \hat{\mathbf{s}}^*\\ &+ t_s t_p^* E_{s,i}H_{p,i}^*\hat{\mathbf{s}} \times \hat{\mathbf{s}}^* - \frac{k_2^*}{k_2}t_p t_s^* H_{p,i}E_{s,i}^*\hat{\mathbf{p}}_t \times \hat{\mathbf{p}}_t^*\end{aligned}$$

Substituting the expanded quantities into Equation B.12 gives a natural grouping into independent equations for s, p, and cross-polarized states

$$0 = \frac{E_{s,i}E_{s,i}^*}{\omega\mu}\left(k_1^*\hat{\mathbf{s}} \times \hat{\mathbf{p}}_i^* + k_1^* r_s r_s^*\hat{\mathbf{s}} \times \hat{\mathbf{p}}_r^* + k_1^* r_s^*\hat{\mathbf{s}} \times \hat{\mathbf{p}}_r^* + k_1^* r_s\hat{\mathbf{s}} \times \hat{\mathbf{p}}_i^* - k_2^* t_s t_s^*\hat{\mathbf{s}} \times \hat{\mathbf{p}}_t^*\right) \cdot \hat{\mathbf{n}}$$

$$0 = \frac{H_{p,i}H_{p,i}^*}{\omega}\begin{pmatrix} -\frac{k_1}{\varepsilon_1}\hat{\mathbf{p}}_i \times \hat{\mathbf{s}}^* - \frac{k_1}{\varepsilon_1}r_p r_p^*\hat{\mathbf{p}}_r \times \hat{\mathbf{s}}^* - \frac{k_1}{\varepsilon_1}r_p^*\hat{\mathbf{p}}_i \times \hat{\mathbf{s}}^*\\ -\frac{k_1}{\varepsilon_1}r_p\hat{\mathbf{p}}_r \times \hat{\mathbf{s}}^* + \frac{k_2}{\varepsilon_2}t_p t_p^*\hat{\mathbf{p}}_t \times \hat{\mathbf{s}}^*\end{pmatrix} \cdot \hat{\mathbf{n}}$$

$$\begin{aligned}0 &= E_{s,i}H_{p,i}^*\left(\hat{\mathbf{s}} \times \hat{\mathbf{s}}^* + r_s r_p^*\hat{\mathbf{s}} \times \hat{\mathbf{s}}^* + r_p^*\hat{\mathbf{s}} \times \hat{\mathbf{s}}^* + r_s\hat{\mathbf{s}} \times \hat{\mathbf{s}}^* - t_s t_p^*\hat{\mathbf{s}} \times \hat{\mathbf{s}}^*\right) \cdot \hat{\mathbf{n}}\\ &+ H_{p,i}E_{s,i}^*\begin{pmatrix} -\frac{k_1^*}{k_1}\hat{\mathbf{p}}_i \times \hat{\mathbf{p}}_i^* - \frac{k_1^*}{k_1}r_p r_s^*\hat{\mathbf{p}}_r \times \hat{\mathbf{p}}_r^* - \frac{k_1^*}{k_1}r_s^*\hat{\mathbf{p}}_i \times \hat{\mathbf{p}}_r^*\\ -\frac{k_1^*}{k_1}r_p\hat{\mathbf{p}}_r \times \hat{\mathbf{p}}_i^* + \frac{k_2^*}{k_2}t_p t_s^*\hat{\mathbf{p}}_t \times \hat{\mathbf{p}}_t^*\end{pmatrix} \cdot \hat{\mathbf{n}}\end{aligned}$$

If the incident wave is homogeneous, then $\hat{\mathbf{s}}$, $\hat{\mathbf{p}}_i$, and $\hat{\mathbf{p}}_r$ are real; thus, $\hat{\mathbf{s}} \times \hat{\mathbf{s}}^* = \hat{\mathbf{p}}_i \times \hat{\mathbf{p}}_i^* = \hat{\mathbf{p}}_r \times \hat{\mathbf{p}}_r^* = 0$. Additionally, the vectors $\mathbf{k}_i$, $\mathfrak{Re}\left\{\mathbf{k}_t\right\}$, $\mathfrak{Im}\left\{\mathbf{k}_t\right\}$ and $\hat{\mathbf{n}}$ are all in the same plane, and thus so are $\hat{\mathbf{p}}_i$, $\hat{\mathbf{p}}_r$, and $\hat{\mathbf{p}}_t$; therefore, $\hat{\mathbf{p}}_i \times \hat{\mathbf{p}}_r^* \cdot \hat{\mathbf{n}} = \hat{\mathbf{p}}_r \times \hat{\mathbf{p}}_i^* \cdot \hat{\mathbf{n}} = \hat{\mathbf{p}}_t \times \hat{\mathbf{p}}_t^* \cdot \hat{\mathbf{n}} = 0$, and the mixed and cross-polarization terms vanish. We now evaluate the remaining vector quantities

$$\begin{aligned}\left(\hat{\mathbf{s}} \times \hat{\mathbf{p}}^*\right) \cdot \hat{\mathbf{n}} &= \left(\hat{\mathbf{s}} \times \left(\hat{\mathbf{k}}^* \times \hat{\mathbf{s}}^*\right)\right) \cdot \hat{\mathbf{n}} = \left(\left(\hat{\mathbf{s}} \cdot \hat{\mathbf{s}}^*\right)\hat{\mathbf{k}}^* - \left(\hat{\mathbf{s}} \cdot \hat{\mathbf{k}}^*\right)\hat{\mathbf{s}}^*\right) \cdot \hat{\mathbf{n}}\\ &= \hat{\mathbf{k}}^* \cdot \hat{\mathbf{n}} = \frac{\mathbf{k}^* \cdot \hat{\mathbf{n}}}{k^*}\\ \left(\hat{\mathbf{p}} \times \hat{\mathbf{s}}^*\right) \cdot \hat{\mathbf{n}} &= \left(\left(\hat{\mathbf{k}} \times \hat{\mathbf{s}}\right) \times \hat{\mathbf{s}}^*\right) \cdot \hat{\mathbf{n}} = -\left(\hat{\mathbf{s}}^* \times \left(\hat{\mathbf{k}} \times \hat{\mathbf{s}}\right)\right) \cdot \hat{\mathbf{n}}\\ &= -\left(\left(\hat{\mathbf{s}}^* \cdot \hat{\mathbf{s}}\right)\hat{\mathbf{k}} + \left(\hat{\mathbf{s}}^* \cdot \hat{\mathbf{k}}\right)\hat{\mathbf{s}}\right) \cdot \hat{\mathbf{n}} = -\hat{\mathbf{k}} \cdot \hat{\mathbf{n}} = -\frac{\mathbf{k} \cdot \hat{\mathbf{n}}}{k}\end{aligned}$$

Making these substitutions and factoring out constants,

$$\begin{aligned}0 &= \mathbf{k}_i^* \cdot \hat{\mathbf{n}} + r_s r_s^*\mathbf{k}_r^* \cdot \hat{\mathbf{n}} + r_s^*\mathbf{k}_r^* \cdot \hat{\mathbf{n}} + r_s\mathbf{k}_i^* \cdot \hat{\mathbf{n}} - t_s t_s^*\mathbf{k}_t^* \cdot \hat{\mathbf{n}}\\ 0 &= \frac{\mathbf{k}_i \cdot \hat{\mathbf{n}}}{\varepsilon_1} + r_p r_p^*\frac{\mathbf{k}_r \cdot \hat{\mathbf{n}}}{\varepsilon_1} + r_p^*\frac{\mathbf{k}_i \cdot \hat{\mathbf{n}}}{\varepsilon_1} + r_p\frac{\mathbf{k}_r \cdot \hat{\mathbf{n}}}{\varepsilon_1} - t_p t_p^*\frac{\mathbf{k}_t \cdot \hat{\mathbf{n}}}{\varepsilon_2}\end{aligned}$$

Then, recalling that $\mathbf{k}_r \cdot \hat{\mathbf{n}} = -\mathbf{k}_i \cdot \hat{\mathbf{n}}$ we can write

$$
\begin{aligned}
0 &= 1 - \mathcal{R}_s - \mathcal{T}_s \\
0 &= 1 - \mathcal{R}_p - \mathcal{T}_p
\end{aligned}
$$

$$
\begin{aligned}
\mathcal{R}_s &= r_s r_s^* \\
\mathcal{T}_s &= t_s t_s^* \frac{\mathbf{k}_t^* \cdot \hat{\mathbf{n}}}{\mathbf{k}_i^* \cdot \hat{\mathbf{n}}} \\
\mathcal{R}_p &= r_p r_p^* \\
\mathcal{T}_p &= t_p t_p^* \frac{\varepsilon_1 \mathbf{k}_t \cdot \hat{\mathbf{n}}}{\varepsilon_2 \mathbf{k}_i \cdot \hat{\mathbf{n}}}
\end{aligned}
$$

$$
\begin{aligned}
\mathcal{S}_r \cdot \hat{\mathbf{n}} &= \mathcal{R} \mathcal{S}_i \cdot \hat{\mathbf{n}} \\
\mathcal{S}_t \cdot \hat{\mathbf{n}} &= \mathcal{T} \mathcal{S}_i \cdot \hat{\mathbf{n}}
\end{aligned}
$$

If the incident wave is homogeneous, $\mathcal{S}_i$ is real, therefore $\mathbf{S}_i = \mathcal{S}_i$ and $\mathbf{S}_r \cdot \hat{\mathbf{n}} = \mathcal{R}\mathbf{S}_i \cdot \hat{\mathbf{n}}$. If we take the transmitted wave as also being homogeneous (it will in general not be) then, similarly, $\mathbf{S}_t \cdot \hat{\mathbf{n}} = \mathfrak{Re}\left\{\mathcal{T}\right\} \mathbf{S}_i \cdot \hat{\mathbf{n}}$